NASA CONTRACTOR REPORT 177424

Application of a Low Order Panel Method to Complex Three-Dimensional Internal Flow Problems

D. L. Ashby
D. R. Sandlin
California Polytechnic State University
Aeronautical Engineering Department
San Luis Obispo, California

Prepared for
Ames Research Center
under Contract NCC2-226
September 1986

National Aeronautics and
Space Administration

Ames Research Center
Moffett Field, California 94035

ABSTRACT

APPLICATION OF A LOW ORDER PANEL METHOD TO COMPLEX THREE-DIMENSIONAL INTERNAL FLOW PROBLEMS

An evaluation of the ability of a low order panel method to predict complex three-dimensional internal flow fields has been made. The computer code VSAERO was used as a basis for the evaluation. Guidelines for modeling internal flow geometries were determined and the effects of varying the boundary conditions and the use of numerical approximations on the solution accuracy were studied. Several test cases were run and the results were compared with theoretical or experimental results.

Modeling an internal flow geometry as a closed box with normal velocities specified on an inlet and exit face provided accurate results and gave the user control over the boundary conditions. The values of the boundary conditions greatly influenced the amount of leakage an internal flow geometry suffered and could be adjusted to eliminate leakage. The use of the far-field approximation to reduce computation time influenced the accuracy of a solution and was coupled with the values of the boundary conditions needed to eliminate leakage. The error induced in the influence coefficients by using the far-field approximation was found to be dependent on the type of influence coefficient, the far-field radius, and the aspect ratio of the panels. In all three test cases run, the VSAERO results agreed very well with experimental or theoretical results, provided the boundary conditions and far-field radius were set according to the guidelines developed in this paper.

TABLE OF CONTENTS

NOMENCLATURE

AR	Aspect Ratio
AREA	Area of a panel
B_{JK}	Velocity potential influence coefficient due to a uniform distribution of unit source on panel K
C_{JK}	Velocity potential influence coefficient due to a uniform distribution of unit doublet on panel K
C_P	Pressure coefficient
dS	Differential surface element on configuration
$\hat{l}, \hat{m}, \hat{n}$	Unit vectors in panel coordinate system
l,m,n	Panel coordinate axes
N_S	Total number of surface panels
P	An arbitrary point in space
$\bar{r}$	Vector between an arbitrary point P and a surface element dS
S	Surface of the configuration
S_∞	Imaginary surface at infinity
$\bar{V}$	Velocity vector
V	Magnitude of velocity vector
$\bar{V}_{\mu_{TK}}$	Velocity influence coefficient due to a uniform distribution of unit doublet on panel K
$\bar{V}_{\sigma_{TK}}$	Velocity influence coefficient due to a uniform distribution of unit source on panel K
W	Wake surface
x	Coordinate in free-stream flow direction
y	Coordinate perpendicular to plane of symmetry
z	Coordinate perpendicular to flow direction and parallel to the $y = 0$ plane of symmetry
Φ	Total velocity potential

φ	Perturbation velocity potential
φ_∞	Free-stream velocity potential
μ	Doublet singularity strength per unit area
σ	Source singularity strength per unit area

subscripts:

i	Interior region
J	Refers to panel J or its control point
K	Refers to panel K or its control point
L	Lower surface of panel
P	Refers to velocity scan point P
U	Upper surface of panel
∞	Free-stream conditions

LIST OF FIGURES

CHAPTER 1
INTRODUCTION

Panel methods have been used for years to numerically predict flow fields around arbitrary three-dimensional bodies. In a panel method, the geometry of a three-dimensional body is represented with a set of panels. Singularities are distributed over the panels to create the flow field around the body. The singularities may be sources, doublets, vortices, or some combination of these. If vortices or doublets are used, the body can support lift provided it has a wake. If the singularities are distributed with constant strength over each panel, a low order panel method results. If the singularities are distributed with a linearly or quadratically varying strength over each panel, a high order panel method results. High order panel methods tend to be more accurate than low order panel methods because they better model a continuous singularity strength distribution over the body; however, high order panel methods require significantly longer computation times and care must be taken to ensure that all the panels representing the body match up exactly due to the requirement that the singularity strength be continuous across panels. The long computation times required for the high order panel methods can be a limiting factor for complicated geometries with high panel densities; hence, there is considerable interest in improving the accuracy of low order panel methods without sacrificing their shorter computation times.

Typically, panel methods are used to model three-dimensional bodies such as an aircraft in an external uniform onset flow. Panel methods have been used as a design tool to evaluate things like the effect of canard and tail placement on an aircraft's aerodynamics. Recently, there has been considerable interest in using panel methods for predicting internal flow fields. Engineers at NASA Ames Research Center are currently using panel methods to aid in the redesign of the National Full-Scale Aerodynamics Complex (NFAC) shown in Figure 1 (7 and 8). One set of turning

vanes, vane set 5, has been extensively redesigned following a catastrophic structural failure in December of 1980. Because of the extremely complicated geometries involved in modeling turning vanes in a wind tunnel, as many as 3000 panels or more are required to model the geometry. For problems of this size high order panel methods become prohibitively expensive. A low order panel method is a much preferred alternative provided sufficient accuracy can be obtained. Panel methods offer the advantage of being able to run design iterations to optimize a design before testing it in the field. This greatly reduces expensive testing time by eliminating the need to test each design iteration. Panel methods also provide the capability of testing full scale items which would be difficult, if not impossible, to test in the field, thus eliminating the need for scaling corrections. Models mounted in the wind tunnel could also be modeled using panel methods. The effect of vortex-induced loads on turning vanes downstream of high lift configuration models could be evaluated prior to running the models in the wind tunnel. The engineer could test a variety of configurations with a panel method and determine which ones he wants to test in the tunnel. Expensive wind tunnel time can be reduced by eliminating configurations that will not work. Panel methods could also provide a source of confirmation for wind tunnel data, thus reducing the chance of bad data slipping by unnoticed.

To date, application of panel methods to internal flow problems has been limited mainly to higher order panel methods. This is because most low order panel methods suffer severely from leakage when applied to internal flows. Leakage manifests itself as a nonconstant mass flux down the length of the tunnel. Leakage occurs because the boundary conditions are applied only at the control point of each panel and the flow is free to leak everywhere else. The simplest internal flow problem is the case of a duct with straight parallel walls. This case was examined by D.R. Holt and B. Hunt (3). They modeled such a duct as a long open tube set in a uniform external flow field as shown in Figure 2. Hunt and Holt were examining the use of a panel method to predict wall interference corrections for a wing in a tunnel. Their tunnel was modeled with a piecewise constant source distribution on

the wall panels. Even for this very simple case Hunt and Holt observed low levels of leakage through the tunnel walls, leading to an apparently varying mass flux down the tunnel. The leakage problem becomes more pronounced when a wind tunnel with a full three-dimensional contraction, test section, and diffuser is modeled. This problem is much more difficult to solve using panel methods, because the tunnel walls typically have to turn the flow a great deal and the contraction and diffuser impart large changes in velocity down the length of the wind tunnel.

Recent improvements in the mathematical basis for low order panel methods seem to have made them more suitable for application to internal flow problems. The low order panel method VSAERO (1 and 2) is a program which has given good results in preliminary application to internal flow problems. VSAERO employs piecewise constant source and doublet distributions over each panel. The body must be modeled as a closed surface which divides all space into two regions: an inner and an outer region. The external region contains the flow field of interest while the inner region contains a fictitious flow. The boundary conditions used by VSAERO are an external Neumann boundary condition which implies a known normal velocity at the control point of each panel and an internal Dirichlet boundary condition of zero perturbation potential inside the surface. The second boundary condition implies that the fictitious potential internal to the closed surface of the body is set equal to the known free-stream potential. This reduces the jump in potential across the surface from the inner to the outer flow, thereby reducing the strength of the singularities needed on the surface. The boundary conditions used in VSAERO enable it to accurately handle complicated geometries which were previously handled only by high order panel methods.

The present study will assess the applicability of a low order panel method to internal flow problems. The computer code VSAERO will be used as a basis for the present study; however, it should be noted that the material presented in this report applies to low order panel methods in general . This report will outline the theoretical basis for VSAERO, give guidelines for modeling the geometry, and present a study of the effects of the boundary conditions and numerical approximations on

the accuracy of the method. In addition a variety of test cases will be run and the results compared with theoretical and experimental data.

CHAPTER 2
THEORY

VSAERO is a low order panel method based on potential flow theory. The flow problem is solved by assuming that the body is at rest in a moving flow field. The body is modeled as a closed surface which divides space into two regions as shown in Figure 3. One region contains the flow field of interest and the other contains a fictitious flow. Figure 3 shows the external region as the flow field of interest and the internal flow as the fictitious flow. This is the typical arrangement for external flow problems such as a wing in a uniform stream. This arrangement is reversed for internal flow problems. The internal region contains the flow field of interest and the external flow field is fictitious. In either case it is assumed that the velocity potentials in both regions satisfy Laplace's equation:

$$\nabla^2\Phi = 0$$
$$\nabla^2\Phi_i = 0 \tag{1}$$

The potential at any point P in either region may be evaluated by applying Green's Theorem to both regions. This results in the following integral equation:

$$\Phi_P = \frac{1}{4\pi}\int\limits_{S+W+S\infty}\int (\Phi - \Phi_i)\hat{n}\cdot\nabla(\frac{1}{\bar{r}})dS$$
$$-\frac{1}{4\pi}\int\limits_{S+W+S\infty}\int \frac{1}{\bar{r}}\hat{n}\cdot(\nabla\Phi - \nabla\Phi_i)dS \tag{2}$$

where $\bar{r}$ is the distance from the point P to the element dS on the surface and $\hat{n}$ is the unit normal vector to the surface pointing into the flow field of interest. In this equation the first integral represents the disturbance potential from a surface distribution of doublets with strength $(\Phi - \Phi_i)$ per unit area and the second integral

represents the contribution from a surface distribution of sources with strength $-\hat{n} \cdot (\nabla\Phi - \nabla\Phi_i)$ per unit area. This equation may be simplified by noting that at the surface at infinity, the perturbation potential due to the configuration is essentially zero, leaving only the potential due to the uniform onset flow. It is assumed that the wake is thin and there is no entrainment so the source term for the wake disappears and the jump in normal velocity across the wake is zero. Hence the simplified equation becomes:

$$\begin{aligned}\Phi_P = &\frac{1}{4\pi}\int_S\int(\Phi-\Phi_i)\hat{n}\cdot\nabla(\frac{1}{\bar{r}})dS \\ &-\frac{1}{4\pi}\int_S\int\frac{1}{\bar{r}}\hat{n}\cdot(\nabla\Phi-\nabla\Phi_i)dS \\ &+\frac{1}{4\pi}\int_W\int(\Phi_U-\Phi_L)\hat{n}\cdot\nabla(\frac{1}{\bar{r}})dS+\phi_{\infty_r}\end{aligned} \tag{3}$$

The point P must be excluded from the integration if it lies on the surface, since the integrals become singular in that case at point P. This is done by assuming a hemispherical deformation of the surface centered at P. If the integral is evaluated for this hemispherical deformation as its radius is allowed to go to zero, the contribution at point P is $1/2(\Phi - \Phi_i)_P$. Hence Equation 3 becomes:

$$\begin{aligned}\Phi_P = &\frac{1}{4\pi}\int_{S-P}\int(\Phi-\Phi_i)\hat{n}\cdot\nabla(\frac{1}{\bar{r}})dS-1/2(\Phi-\Phi_i)_P \\ &-\frac{1}{4\pi}\int_S\int\frac{1}{\bar{r}}\hat{n}\cdot(\nabla\Phi-\nabla\Phi_i)dS \\ &+\frac{1}{4\pi}\int_W\int(\Phi_U-\Phi_L)\hat{n}\cdot\nabla(\frac{1}{\bar{r}})dS+\phi_{\infty_r}\end{aligned} \tag{4}$$

The boundary condition used to solve Equation 4 is an internal Dirichlet boundary condition. The total potential Φ can be viewed as being made up of an onset potential ϕ_∞ and a perturbation potential $\phi = \Phi - \phi_\infty$. The potential of the fictitious flow is set equal to the onset potential, ϕ_∞. With this boundary condition, the

singularities on the surface tend to be smaller than if the potential of the fictitious flow is set to zero because the singularities only have to provide the perturbation potential instead of the total potential. Using this boundary condition and looking at points P inside the surface, Equation 4 can be rewritten as:

$$\begin{aligned} 0 = & \frac{1}{4\pi} \int_{S-P} \int \phi \hat{n} \cdot \nabla(\frac{1}{\bar{r}}) dS - 1/2\phi_P \\ & - \frac{1}{4\pi} \int_{S} \int \frac{1}{\bar{r}} \hat{n} \cdot (\nabla\Phi - \nabla\phi_\infty) dS \\ & + \frac{1}{4\pi} \int_{W} \int (\Phi_U - \Phi_L) \hat{n} \cdot \nabla(\frac{1}{\bar{r}}) dS \end{aligned} \tag{5}$$

where the doublet strength is defined as

$$4\pi\mu = \phi = \Phi - \phi_\infty \tag{6}$$

and the source strength is defined as

$$4\pi\sigma = -\hat{n} \cdot (\nabla\Phi - \nabla\phi_\infty) \tag{7}$$

Looking at equation 7, if it is assumed that the normal velocity at the surface is either zero or some known value, then the source strengths can be solved for immediately. Substituting equation 6 into equation 5 leaves one integral equation with the unknown doublet strength over the surface to solve for. Once the doublet and source strengths are known, the general equation for the potential at any point P can be written as:

$$\begin{aligned} \Phi_P = & \int_{S} \int \mu \hat{n} \cdot \nabla(\frac{1}{\bar{r}}) dS + K\mu_P \\ & + \int_{S} \int \frac{\sigma}{\bar{r}} dS \\ & + \int_{W} \int \mu_W \hat{n} \cdot \nabla(\frac{1}{\bar{r}}) dS + \phi_{\infty P} \end{aligned} \tag{8}$$

where $K = 0$ if P is not on the surface, $K = 2\pi$ if P is on a smooth part of the outer surface, $K = -2\pi$ if P is on a smooth part of the inner surface and $K =$ the solid angle contained at the crease if P lies at a crease in the surface (2).

If the surface is broken up into panels, Equation 5 can be written in discretized form, breaking the integrals up into surface integrals over each panel. VSAERO assumes constant strength source and doublet distributions over each panel (thus making it a low order panel method); therefore, the doublet and source strengths can be factored out of the integrals. The surface integrals over each panel are summed for all panels to give a set of simultaneous equations to be solved for the unknown doublet strength on each panel. The surface integrals represent the velocity potential influence coefficients per unit singularity strength for panel K acting on the control point of panel J. Hence Equation 5 becomes:

$$\sum_{K=1}^{N_s} (\mu_K C_{JK}) + \sum_{L=1}^{N_w} (\mu_{wL} C_{JL}) + \sum_{K=1}^{N_s} (\sigma_K B_{JK}) = 0; J = 1, N_s \tag{9}$$

where

$$B_{JK} = \int\int_K \frac{1}{\bar{r}} dS \tag{10}$$

and

$$C_{JK} = \int\int_K \hat{n} \cdot \nabla(\frac{1}{\bar{r}}) dS \tag{11}$$

Since the source values are known, they may be transferred to the right hand side of the matrix equation.

The first step in the solution of this matrix equation is the determination of the velocity potential influence coefficient matrix elements C_{JK} for the unknown doublet strengths and B_{JK} for the known source strengths. The actual solution for the velocity potential influence coefficients C_{JK} and B_{JK} is given in Appendix A. VSAERO makes use of an approximation commonly employed in panel methods. For panels that are nearby, the influence coefficients are calculated exactly by

treating the singularities as being distributed over the panel and integrating over the panel surface; however, for panels that are far away, the influence coefficients are calculated by treating the panel as though it were a point source or point doublet. The distance at which this approximation starts being used is determined by the far-field radius. This distance is nondimensionalized by a characteristic panel size to give a far-field factor. The characteristic panel size is the sum of the distance from the midpoint of one side to the centroid of the panel and the distance from the midpoint of an adjacent side to the midpoint. The far-field factor is then defined as the far-field radius divided by the characteristic panel size. In VSAERO a default value of 5.0 for the far-field factor was found to produce sufficiently accurate results. This default value was determined from initial test cases using a wing and a wing-body configuration (2). The default value for far-field factor can be changed by the user if so desired. The main purpose in using this approximation is that it provides a considerable savings in time with little loss in accuracy for most configurations.

Once the influence coefficients have been evaluated, the unknown doublets can be solved for. The matrix equation is solved directly using Purcell's vector method for influence coefficient matrices which are 600×600 or smaller. For larger matrices, a blocked controlled Gauss-Seidel iterative technique is used (10). The convergence criteria for the doublet solution requires that the solution residuals be less than the default value of 0.2 percent of the maximum doublet size in the solution. This value may be changed by the user if desired. For internal flow problems it has been found that a value of 0.01 percent of the maximum doublet size for the converged solution residual works pretty well. This convergence criteria generally results in 50 to 100 iterations to determine a converged solution for internal flow problems.

With the unknown doublets solved for, the singularities on all the panels are known; thus, the velocities at the control points of the panels can be evaluated. The velocities normal to the panels are either zero or the value specified by the user. The tangential velocities on the surface are evaluated in the panel coordinate system by differentiating the doublet strengths in the appropriate direction for each

tangential component of velocity. With the three components of velocity calculated in the panel coordinate system, the velocities can be transformed into the x, y, z coordinate system of the entire configuration and a resultant velocity can be calculated. Using the resultant velocity at each panel control point, the pressure coefficient at each panel control point can be calculated using the following equation:

$$C_{P_K} = 1 - V_K^2/V_\infty^2 \tag{12}$$

With the pressure distribution over the body determined, the resultant forces in the lift and drag directions can be evaluated as well as the moments about a user defined reference point.

The velocities at scan points off the body are evaluated by taking the gradient of equation 8 with respect to the coordinates of point P. Thus equation 8 becomes:

$$\begin{aligned} \vec{V}_P = &- \int_S \int \mu \nabla(\hat{n} \cdot \nabla(\frac{1}{\vec{r}}))dS \\ &- \int_S \int \sigma \nabla(\frac{1}{\vec{r}})dS \\ &- \int_W \int \mu_W \nabla(\hat{n} \cdot \nabla(\frac{1}{\vec{r}}))dS + \vec{V}_\infty \end{aligned} \tag{13}$$

Equation 13 can also be written in discretized form similar to the equation for the potential at point P. The resulting discretized equation is:

$$\vec{V}_P = \vec{V}_\infty - \sum_{K=1}^{N_s} (\mu_K \vec{V}_{\mu_{rK}}) - \sum_{L=1}^{N_w} (\mu_{w_L} \vec{V}_{\mu_{rL}}) - \sum_{K=1}^{N_s} (\sigma_K \vec{V}_{\sigma_{rK}}) \tag{14}$$

where

$$\vec{V}_{\sigma_{rK}} = \int_K \int \nabla(\frac{1}{\vec{r}})dS \tag{15}$$

and

$$\vec{V}_{\mu_{rK}} = \int_K \int \nabla(\hat{n} \cdot \nabla(\frac{1}{\vec{r}}))dS \tag{16}$$

The velocity influence coefficients $\bar{V}_{\sigma_{PK}}$ and $\bar{V}_{\mu_{PK}}$ must be calculated for all scan points P. The actual solution for the velocity influence coefficients $\bar{V}_{\sigma_{PK}}$ and $\bar{V}_{\mu_{PK}}$ is given in Appendix A.

VSAERO also provides the capability to calculate wake relaxations, on-body and off-body streamlines, and boundary layer properties along surface streamlines. Wake relaxations are performed by aligning the streamwise edges of the wake panels with the local velocity at each panel edge. A new set of influence coefficients must be calculated after each wake relaxation and the singularities on all the panels must be solved for again. The on-body and off-body streamline calculations are based on velocities calculated using the velocity influence coefficients. Details of the streamline calculation can be found in Reference 3. Boundary layer properties are calculated using an integral boundary layer technique along surface streamlines.

When VSAERO or any other panel method based on Green's Theorem is applied to internal flow problems, the influence coefficient matrix becomes singular and the doublet solution is only unique to within an arbitrary constant as discussed in reference 5. VSAERO circumvents this nonuniqueness problem by specifying the doublet value on one panel, thus removing one unknown. In VSAERO the doublet value on one panel on either the inlet face or the fan face is set equal to zero. Another unknown and equation are added to the matrix equation by introducing a correction velocity to satisfy continuity in the tunnel. This correction velocity is a small increment that is added uniformly to all the panels on either the inlet or exit patch. This procedure allows VSAERO to find the solution to a problem which would otherwise be indeterminate. This procedure in VSAERO is still under development.

CHAPTER 3
RESULTS AND DISCUSSION

Geometry Modeling

The geometry initially selected to evaluate a low order panel method's ability to solve internal flow problems was a portion of the 40 × 80 circuit of the NFAC at NASA Ames Research Center. A plan view of the 40 × 80 circuit is shown in Figure 1. The portion of the 40 × 80 modeled in this study consisted of the contraction, the test section, and the diffuser. None of the corners or turning vanes were included in the model. The 40 × 80 geometry was selected because it provides a complex three-dimensional internal flow. Once it was shown that a low order panel method could successfully predict the flow field in an empty tunnel, several test cases of tunnels with bodies in them were run.

The 40 × 80 has a 7.9:1 contraction with the shape of a cubic curve. The corners of the contraction are quarter circles with a radius of 20 feet at the beginning of the contraction. The test section has dimensions of 40 feet high by 80 feet wide. The test section is composed of a 40 foot square center with two semicircular sections, one on either side, of 20 foot radius. The diffuser has a diffusion ratio of 2.6:1 and a diffusion half angle of approximately 2.75 degrees. The corners of the diffuser are circular at the test section end and are filleted to sharp corners at the end of the diffuser. The lengths of the contraction, test section, and diffuser are 145.0 feet, 85.01 feet, and 297.88 feet respectively. A view of the 40 × 80 contraction, test section, and diffuser is shown in Figure 5.

Wind tunnels and ducts can be modeled in several ways. One way to model a tunnel is to panel an inside surface (the actual inner walls of the tunnel) with the normals pointing into the internal flow region, and an outside surface with the normals pointing into the external flow. One end of the tunnel is open to the external flow region and the other end is closed off and a normal velocity is

specified on it. Such a model is shown in Figure 4. This is a very inefficient method of modeling a tunnel for a number of reasons. First, the number of panels required to model the geometry is greatly increased (for creating the outer surface) and hence the complexity of the problem and the computation time go up. Another problem is that with this model the onset flow cannot be set independently of the flow through the tunnel. In order to provide the desired velocity distribution in the tunnel, the onset flow is generally set to zero and the velocity distribution in the tunnel is provided by the normal velocity specified on the fan face. With the onset flow turned off, the benefit of the zero internal perturbation potential is lost. A large jump in potential usually exists across the surface causing the singularities on the panels to be large. When the singularities on the surface are large, the solution does not seem to be as well behaved or as accurate. In some instances however, it is necessary to model a tunnel in this fashion. Such is the case when a tunnel inlet is being modeled as shown in Figure 4.

A much more efficient method of modeling a tunnel is to make the tunnel a closed box with all the panel normals pointing into the box. This type of model is illustrated in Figure 5. The 40×80 wind tunnel was modeled this way in this study. A normal velocity was specified on both the inlet face and the fan face. These normal velocities satisfied continuity based on the areas of the inlet face and the exit face. This type of modeling makes the most efficient use of panels (i.e. there is no waste of panels in modeling external surfaces). This type of modeling also allows the setting of the onset flow independently of what the velocity in the tunnel is, thus giving the user some control over the boundary conditions. The singularities in this case tend to be smaller because they only have to provide the perturbation potential instead of the total potential. The setting of the onset flow for internal flow problems will be discussed in greater detail later in this paper.

There are several guidelines that should be followed when paneling up a tunnel geometry. While these guidelines may not apply in every case, in general they will help eliminate erroneous results caused by poor geometry modeling. The first guideline is to keep the paneling as continuous as possible and avoid gaps and

overlaps in the paneling. One of the reported advantages of low order panel methods is that the panels can be mismatched and still give reasonable answers, since the singularities on the panels are piecewise constant and do not have to match singularity strengths across panel junctions. In internal flow problems, however, the singularities are affecting flow in a constrained region instead of an infinite region. Because of this, internal flows seem to be more sensitive to small errors in the singularity strengths. Avoiding gaps or overlaps is especially important when paneling a wing or a turning vane attached to the tunnel wall. Gaps or overlaps at the wing/wall junction can cause erroneous spanwise flows on the wing.

Sharp corners or discontinuities in the slope of the surface paneling can also cause problems. In a potential flow, a sharp corner or discontinuity will cause large local spikes in the pressure distribution. This results from the flow trying to turn a corner of zero radius. The pressure spikes are confined locally to the area of the discontinuity on the surface. Figures 6 and 7 illustrate the effect of a surface discontinuity on surface pressure coefficients. In these two cases the onset flow is set equal to 1.0 and the far-field factor is set to the default value of 5.0. The effect of these two parameter settings will be discussed later in this paper. Figure 6 shows wall pressure coefficients for a horizontal cut at $z = 0$ for a tunnel where there are no discontinuities in the test section surface paneling except at the entrance and exit of the test section. There are small pressure spikes at the entrance and exit of the test section. Figure 7 shows the wall pressure coefficients at a horizontal cut of $z = 0$ for the same tunnel with a six inch liner added to the test section. At the beginning of the liner is a 45 degree ramp with sharp corners at the top and bottom of the ramp. At the end of the liner is another ramp which is not quite as steep. As can be seen from Figure 7, there is an extremely large pressure spike at both the beginning and the end of the liner.

Another important factor is the order in which the panels that make up the geometry are input, especially for internal flows. VSAERO solves the matrix equation for singularity strength by means of the controlled blocked Gauss-Seidel iterative method (10). Internal flow problems tend to have many large elements in the

influence coefficient matrix. The geometry should be input starting from either the fan face or the inlet face and working to the other end, inputting the panels in a circumferential manner. If this pattern is not followed, some of the large elements could appear far off the diagonal in the influence coefficient matrix which could make it ill-conditioned or even indeterminate.

The panel density is also important in modeling internal flow problems. The panel density should be high in contraction and diffusion regions to prevent leakage problems. In straight sections of the tunnel, the panel density does not need to be as high because the walls are parallel to the flow and do not have to turn the flow. Transition from regions of high panel density to low panel density should be made smoothly. Placing very large panels next to very small panels can yield poor results.This is because low order panel methods use a piecewise constant distribution of singularity strengths, and large gradients in singularity strength, which are common in internal flows, are not modeled well if a very large panel is next to a very small panel.

The paneling for the 40 × 80 geometry, shown in Figure 5, illustrates a typical paneling arrangement for an internal flow problem. Only half the 40 × 80 tunnel was modeled due to symmetry about the $y = 0$ plane . The tunnel was paneled with 22 divisions circumferentially. A section of tunnel upstream of the beginning of the contraction was included in the modeling to provide a smooth transition into the contraction instead of placing the inlet face right at the entrance to the contraction. The spacing in the upstream duct was half cosine with the larger panels at the inlet end. The panel density did not have to be high here because this part of the tunnel was straight and the velocity in this portion of the tunnel was very low. The panel density was greatly increased in the contraction region of the tunnel because the contraction was quite large and rather sudden. The panel spacing in the test section was kept constant because it was a straight section of duct. Because the velocity in the test section was higher than on the upstream duct and because the test section was the main region of interest, a high panel density was used there. In the diffuser, the paneling did not have to be as dense as in the contraction because the diffusion

was very gradual. The inlet face and the fan face were paneled so that they match up with the panels on the tunnel. A total of 2450 panels were used to model the 40×80.

Boundary Conditions

As discussed in the theory section of this report, the boundary conditions used in VSAERO are an external Neumann boundary condition at the control point of each panel and an internal Dirichlet boundary condition. The external Neumann boundary condition specifies the normal velocity at the control point of each panel. From this boundary condition all the source strengths can be determined. The internal Dirichlet boundary condition is set by making the fictitious potential inside the body equal to the onset potential, making the potential jump across the surface small for most geometries, thus reducing the strengths of the singularities. This makes the solution better behaved than it is if the fictitious potential were set to zero.

For internal flow problems that are modeled as a closed box, the flow field of interest is inside the box and the fictitious flow field is external to the box. Flow through the tunnel is set by means of the normal velocities specified on the inlet and fan faces of the tunnel. By modeling the tunnel as a closed box, the onset flow can be set independently of the flow through the tunnel. This gives the user control over the onset flow and thus over the internal Dirichlet boundary condition. The onset flow can be varied to give the best solution inside the tunnel. This is not true if the tunnel is modeled with an inner and outer body and one face open to the external flow. In this case the onset flow cannot be set independently of the flow through the tunnel. Generally the onset flow is turned off and the proper flow through the tunnel is achieved by specifying a normal velocity on the fan face.

The purpose of setting the fictitious flow potential equal to the onset flow potential is to minimize the potential jump across the surface thus reducing the strength of the singularities needed on the surface. Problems arise, however, when a tunnel with a large contraction and/or diffusion ratio is modeled. In this case

the velocity inside the tunnel can vary greatly and the potential due to the velocity in the tunnel can be significantly different from the potential due to the uniform onset flow. The question then becomes what value should the onset flow be set to in order to achieve the best solution in the tunnel when it is modeled as a closed box.

Figures 6, 8, and 9 show the effect of varying the onset flow on the solution in the tunnel, assuming all other variables are held constant. The normal velocities at the inlet face and fan face of the 40×80 were specified so as to yield a velocity of 1.0 in the test section. The far-field factor was left at the default value of 5.0. Leakage in the tunnel was determined by integrating the velocity distribution across the inlet face, the exit face, and a scan plane in the center of the test section. In addition, another indication of leakage was determined from the pressure distribution on the walls of the tunnel. The pressure coefficients are nondimensionalized with a reference velocity of 1.0, so if the velocity in the test section is 1.0 (and the tunnel is conserving mass) then the pressure coefficients on the test section walls will be 0.0. As mentioned in the theory section of this report, VSAERO calculates an incremental correction velocity which is uniformly distributed over the inlet face or the exit face in order to attempt to satisfy continuity in the tunnel. If the tunnel leaks, the correction velocity will be added to or subtracted from one end of the tunnel or the other to compensate for the leakage. During the course of the present study, it was found that if the tunnel conserved mass, the incremental correction velocity was zero, but if the tunnel leaked, the incremental correction velocity was not able to entirely compensate for the leakage.

Figure 6 shows the wall pressure coefficients for the onset flow set equal to 1.0. The tunnel leaks considerably in this case. There was a 9.72 percent increase in mass flux between the inlet and the test section and a 1.21 percent decrease in mass flux between the test section and the diffuser. The net mass flux change between the inlet and the fan face was 8.39 percent. The doublet strengths in this case were quite high, being in the range from 0.0 to -313.0 ft^2/sec per unit area. Figure 8 shows the wall pressure coefficients when the onset flow was set equal to 0.0. In

this case the direction of the leakage was reversed from the previous case. There was a 6.57 percent decrease in mass flux from the inlet face to the test section and a 0.78 percent increase in mass flux from the test section to the diffuser. The net decrease in mass flux was 5.84 percent. Again the doublet strengths were quite large, being on the order of 0.0 to 354.0 ft^2/sec per unit area. In this case it is also important to note that the pressure distribution was not very smooth. This is probably due to the fact that with the onset flow turned off, the source strengths on the surface are zero except where nonzero normal velocities are specified. The source distribution on the surface apparently helps smooth out the solution on the surface. Figure 9 shows the wall pressure coefficients when the onset flow was set equal to 0.35. In this case, the leakage was almost completely eliminated. There was a 0.57 percent decrease in mass flux between the inlet face and the test section and a 0.32 percent decrease in mass flux between the test section and the fan face. There was a 0.89 percent net mass flux decrease between the inlet face and the fan face. The singularity strengths also appeared to be at a minimum when compared to the previous two cases. The doublet strengths ranged from 0.0 to 169.0 ft^2/sec per unit area.

From the above results, it appears that there is a value of the onset flow which eliminates leakage in the tunnel. This value of onset flow also minimizes the singularity strengths. The value of the onset flow that eliminates leakage is somewhat less than the average value of the velocity through the tunnel in this case. Because the leakage depends on the specific geometry of the tunnel, it is difficult to derive a rule for setting the onset flow that applies to all tunnel geometries. The best that can be done at this point is to start with the onset flow set to about the average velocity in the tunnel and then vary the onset flow until the tunnel conserves mass. One way to improve upon this is to allow for a variable onset flow for internal flow problems. If the onset flow could be set as a function of x, y, and z so that it more closely matched the anticipated velocities in the tunnel, better results could be obtained without the inefficient iteration process.

Far-Field Approximation

VSAERO makes use of a far-field approximation in calculating the influence coefficients used in solving for the singularity strengths and velocities. The value of the far-field factor seems to be tied in with the value of the onset flow and conservation of mass. If the onset flow is held constant and the far-field factor is varied, the leakage in the tunnel varies. Referring to Figure 9, when the onset flow was set equal to 0.35 and the far-field factor was set equal to 5.0, the tunnel was conserving mass. In Figure 10 the far-field factor was increased to 10.0 without changing the onset flow. In this case the tunnel no longer conserved mass. There was a 1.72 percent increase in mass flux between the inlet face and the test section and a 0.71 percent decrease in mass flux between the test section and the fan face. This gave a net mass flux increase of 1 percent between the inlet face and the fan face. In Figure 11, the onset flow was reduced to 0.1 and the tunnel again conserved mass. Figure 12 shows a plot of onset flow versus far-field factor. As can be seen in this figure, as the far-field factor is increased, the onset flow needed to conserve mass in the tunnel decreases. In the limit where the far-field factor is set high enough to include the entire geometry, the value of the onset flow at which the tunnel conserves mass is 0.0. Apparently the far-field approximation causes leakage in the tunnel and this leakage can be alleviated by turning on the onset flow. The coupling of the far-field approximation and the Dirichlet boundary condition is useful for reducing the computation time while still maintaining accuracy in the solution. Computation time increases substantially as the far-field factor is increased as shown in Figure 13; therefore, the far-field factor should only be increased enough to give the desired accuracy in the solution and the onset flow should be set to balance mass flow.

The default value of 5.0 for the far-field factor does not appear to be large enough for internal flow problems. This is illustrated in Figures 14 and 15, which show angularity contours on a scan plane in the center of the test section. In Figures 14a and 14b, the far-field factor was set to the default value of 5.0 and the onset flow was set so that the tunnel was conserving mass. In this case, there was a large amount of angularity in the flow. The alpha angle varied from -0.5 to 0.5 degrees

with the largest angularity being near the centerline of the tunnel. The beta angle varied between -0.292 and 0.363 degrees with some of the larger values in the center portion of the test section. In Figures 15a and 15b, the far-field factor was increased to 10.0, and the onset flow was readjusted so that the tunnel was conserving mass. In this case the angularity in the test section disappeared almost entirely. The alpha angle varied between -0.0176 and 0.0176 degrees and the beta angle varied between -0.0784 and 0.0 degrees. Apparently internal flows are more sensitive to the far-field approximation than external flows, probably because in internal flows the singularities are acting on a confined region of fluid instead of an infinite region of fluid. It should be noted that at a far-field factor of 5.0, the solution on the surface was reasonable, but the solution on the velocity scan planes was not. Since the velocities on the scan plane are calculated using velocity influence coefficients instead of velocity potential influence coefficients as on the surface, it appears that the far-field approximation affects the two types of influence coefficients differently.

The error caused by using the far-field approximation for the velocity influence coefficients and the velocity potential influence coefficients was mapped out for the influence of a panel on another panel, and the influence of a panel on a scan point. The difference between the exact solution for the influence coefficients and the far-field approximation is that in the exact solution, the integration is carried out over the panel surface as detailed in Appendix A, while in the far-field approximation, the singularities are treated as point singularities at the centroid of the panel. A computer code (contained in Appendix A) was written to evaluate both the velocity influence coefficients and the velocity potential influence coefficients due to sources and doublets. The code calculated the influence coefficients both exactly and using the far-field approximation for the influence of one panel on another. A variety of panel arrangements, sizes, and separation distances were studied in order to put together a complete picture. The results from the computer code were plotted with a contour plotter using Akima's method with a tension value of 0.4.

Figures 17 through 21 show the results of the far-field approximation error analysis for the velocity potential influence coefficients. The panels used in this

analysis were rectangular, but the results can be extended to irregularly shaped panels. The panel with the singularity distribution on it was panel K and the panel being influenced was panel J. The coordinate system for the two panels is shown in Figure 16. Plane 1 contains the L and N axes of panel K, plane 2 contains the M and N axes of panel K, and plane 3 contains the L and M axes of panel K. Since the problem is symmetric about all three axes, only results for one quadrant are presented. Panel J was rotated through 90 degrees at varying radii in the three different planes. Panel J was oriented in three different ways in planes 1 and 2. In Case 1, the normal to panel J was held parallel to the line between the control points of the two panels and pointing toward panel K. In Case 2, the normal to panel J was held perpendicular to the line between the control points of the two panels and pointing in the $+N$ direction when $\theta = 0$ degrees. In Case 3, the normal to panel J was held parallel to plane 3 and pointing in the $-L$ or the $-M$ direction depending on which plane panel J was in. When panel J was in plane 3, the only case that was run was Case 4 where the normal to panel J was parallel to the N axis and pointing in the $+N$ direction. The radius from panel K to panel J was nondimensionalized by the characteristic panel size of panel K so that the distance between panels was expressed in terms of the nondimensional far-field factor. The far-field factor was varied from 2.0 to 10.0 by increments of 2.0. Panel J was rotated through 90 degrees in increments of 15 degrees. All cases were run for panel K aspect ratios of 1.0 and 4.0. The panel orientations for all cases run are illustrated in Figure 16.

Figures 17a, 17b, and 17c show the error in B_{JK} caused by using the far-field approximation for Case 1. Figure 17a shows the error when panel K had an aspect ratio of 1 and panel J was in plane 1. The error incurred by using the far-field approximation was quite small. The error was 0.2 percent at a far-field factor of 6 and increased in an exponential manner to 1.4 percent at a far-field factor of 3. The error started off positive at $\theta = 0$ degrees and went through a zero point at $\theta = 38$ degrees. Above $\theta = 38$ degrees, the error was negative. Figure 17b shows the error when the aspect ratio of panel K was increased to 4 and panel J was in plane 1. In this case the error increased somewhat, but was still relatively small.

The error was 0.25 percent at a far-field factor of 9 and increased to 1.75 percent at a far-field factor of 3.75. The node of zero error occurred at $\theta = 50$ degrees in this case. Figure 17c shows the error when the aspect ratio of panel K was 4 and panel J was in plane 2. In this case there was no node of zero error and the error was negative for all values of θ. The error was 0.25 percent at a far-field factor of 6.5 and increased to 1.75 percent at a far-field factor of 3.

Figures 18, 19, and 20 show the error in B_{JK} caused by using the far-field approximation for Cases 2, 3, and 4. The results from these cases were similar to the results described above for Figure 17. Similar patterns occurred in each case. The relative magnitude of the error varied slightly from case to case, but in general the error was on the order of 1 percent or less for far-field factors of 4 or greater. The node of zero error occurred at different values of θ depending on which case was being studied, but it usually occurred at θ values between 30 and 60 degrees. The only time there was no node of zero error was when panel J was in plane 2 and the aspect ratio of panel K was greater than 1 or when panel J was in plane 3 and the aspect ratio of panel K was equal to 1.

Figures 21a, 21b, and 21c show the error in C_{JK} caused by using the far-field approximation for Case 1. It was found that the results for Cases 2 and 3 were identical to those for Case 1 so only the results for Case 1 are shown. Figure 21a shows the error when panel K had an aspect ratio of 1 and panel J was in plane 1. The error was about twice as large as it was for B_{JK}. The error ranged between 0.5 percent at a far-field factor of 8 to 3.5 percent at a far-field factor of 3.5. The node of zero error in this case occurred at $\theta = 45$ degrees. The error was positive below 45 degrees and negative above 45 degrees. Figure 21b shows the error when the aspect ratio of panel K was increased to 4 and panel J was in plane 1. The error increased significantly. The error was 1 percent at a far-field factor of 10 and increased to 7 percent at a far-field factor of 4. The node of zero error occurred at $\theta = 60$ degrees. The largest errors occurred at angles below 60 degrees. Figure 21c shows the error when panel K had an aspect ratio of 4 and panel J was in plane 2. Here the error was of the same magnitude as when panel K had an aspect ratio

of 1 and panel J was in plane 1. The error ranged from 0.5 percent at a far-field factor of 8 to 3.5 percent at a far-field factor of 3.5. The error was always negative in this case. When panel J was in plane 3 (i.e. Case 4), it was found that the error was always zero. Both the exact solution and the far-field approximation predicted a value of zero for C_{JK} when panel J was in plane 3.

The results of the far-field approximation error analysis for the velocity influence coefficients are shown in Figures 22 through 27. The scan point P was moved through all the same positions in planes 1 and 2 that panel J was. The scan point P was not run in plane 3 because for internal flow problems velocity scan points usually do not lie in the same plane as any of the panels. Since there is no orientation on a point as there is on a panel, only one case needed to be run for the scan point P. Since the velocity influence coefficient is a vector quantity, its three components in the coordinate system of panel K were examined in each plane. Again aspect ratios of 1 and 4 for panel K were run.

Figures 22a and 22b show respectively the error in the L and N components of $\bar{V}_{\sigma_{PK}}$ caused by using the far-field approximation when the scan point P was in plane 1 and panel K had an aspect ratio of 1. When the scan point P was in plane 1, the M component of $\bar{V}_{\sigma_{PK}}$ was zero and there was no error. The error in both nonzero components of $\bar{V}_{\sigma_{PK}}$ was of the same magnitude as the error in C_{JK}. For the L component, shown in Figure 22a, the error ranged between 0.5 percent at a far-field factor of 9.75 to 3.5 percent at a far-field factor of 4. The node of zero error occurred at $\theta = 30$ degrees and the largest errors were at angles above 30 degrees. For the N component, shown in Figure 22b, the error ranged from 0.5 percent at a far-field factor of 8 to 3.5 percent at a far-field factor of 3.5. The node of zero error occurred at $\theta = 45$ degrees.

Figures 23 and 24 show the error contours for the nonzero components of $\bar{V}_{\sigma_{PK}}$ when the aspect ratio of panel K was increased to 4. Figure 23a shows the error in the L component of $\bar{V}_{\sigma_{PK}}$ when the scan point P was in plane 1. The error ranged from 1 percent at a far-field factor of 9.75 to 7 percent at a far-field factor of 3.8. The node of zero error was at $\theta = 40$ degrees with the larger errors occurring at

angles above 40 degrees. Figure 23b shows the error in the N component of $\bar{V}_{\sigma_{PK}}$ when the scan point P was in plane 1. The results were very similar to those for the L component except that the zero error node occurred at $\theta = 60$ degrees and the largest errors occurred at angles below 60 degrees. Figures 24a and 24b show the errors in the M and N components of $\bar{V}_{\sigma_{PK}}$ when the scan point P was in plane 2. In these cases the error was always negative and ranged from 0.5 percent at a far-field factor of 8 to 3.5 percent at a far-field factor of 3.5.

Figures 25a and 25b show the error respectively in the L and N components of $\bar{V}_{\mu_{PK}}$ when panel K had an aspect ratio of 1 and the scan point P was in plane 1. The error in this case was quite large. The error in the L component, shown in Figure 25a, ranged from 1 percent at a far-field factor of 9 to 7 percent at a far-field factor of 3.75. The node of zero error was at $\theta = 45$ degrees. The error in the N component, shown in Figure 25b, ranged from 1 percent at a far-field factor of 10 to 7 percent at a far-field factor of 4. There were two nodes of zero error in this case. The largest errors occurred at angles between 15 and 60 degrees.

When the aspect ratio of panel K was increased to 4, and the scan point P was in plane 1, the error in the components of $\bar{V}_{\mu_{PK}}$ increased greatly . This is shown in Figures 26a and 26b. The error in the L component, shown in Figure 26a, ranged from 2 percent at a far-field factor of 9.8 to 7 percent at a far-field factor of 5.5. The node of zero error occurred at $\theta = 45$ degrees. The error in the N component, shown in Figure 26b, increased the most. The error ranged from 4 percent at a far-field factor of 9.25 to as high as 14 percent at a far-field factor of 5.75. In this case the sign of the error seemed to alternate several times. The largest errors occurred at angles between 15 and 60 degrees.

When the scan point P was moved to plane 2, the errors were not quite as large, but they were still larger than the errors for the other influence coefficients in the same case. Figure 27a shows the error in the M component. The error ranged from 0.5 percent at a far-field factor of 10 to 3.5 percent at a far-field factor of 4. The error in this case was always negative. Figure 27b shows the error in the N component. The error in this case was in the same range as that for the M

component. There was a node of zero error in this case, though, and it occurred at $\theta = 30$ degrees. The larger errors occurred at angles above 30 degrees.

Two important conclusions can be drawn from the results discussed above. The first conclusion is that the amount of error due to using the far-field approximation varies for the different influence coefficients. The influence coefficient least sensitive to the far-field approximation is B_{JK}. The errors induced in C_{JK} and $\bar{V}_{\sigma_{TK}}$ due to the use of the far-field approximation are about the same and are roughly twice the error induced in B_{JK}. The error induced in $\bar{V}_{\mu_{TK}}$ due to the far-field approximation is the greatest and is roughly 4 to 10 times the error induced in B_{JK}. This suggests that computation time could be saved while still obtaining the accuracy desired by using different values of the far-field factor for the various influence coefficients instead of using the same value for all of them as is currently the case in VSAERO. The user could define the far-field factor for B_{JK} and then it could be multiplied by some factor greater than one for the the other influence coefficients. Based on the results of the present study, suggested multiplication factors would be 1.5 for C_{JK} and $\bar{V}_{\sigma_{TK}}$ and 2.0 for $\bar{V}_{\mu_{TK}}$. This scheme should yield close to the same accuracy as doubling the far-field factor for all the influence coefficients, but with less computation time.

The second conclusion that can be drawn from the results above is that the aspect ratio of the panels greatly influences the amount of error induced in the influence coefficients by using the far-field approximation. If the aspect ratio of the panels is increased, the error in the influence coefficients due to the far-field approximation is also increased. If the aspect ratio of a panel is increased by a factor of four, the error increases by roughly a factor of two for any given far-field factor. Thus the final solution will be more accurate if the aspect ratio of the panels is kept as close to 1 as possible. In some cases it is difficult to model a geometry without using higher aspect ratio panels. In this case it would be beneficial to include an option in the program whereby the user could specify selected groups of panels which have high aspect ratios. The far-field factor could then be increased by some factor for these groups of panels rather than increasing the far-field factor for

all the panels. This would also increase accuracy with less increase in computation time than if the far-field factor was increased for all panels.

CHAPTER 4
TEST CASES

Cylinder in a Rectangular Duct

Once the most efficient manner of modeling internal flows for VSAERO was determined, several test cases of increasing complexity were run to validate the ability of VSAERO to handle complex internal flow problems. The first test case was a cylinder in a straight rectangular duct. The cylinder was extended wall-to-wall and both the nonlifting and the lifting cases were considered. A straight rectangular duct was chosen because it was one of the simplest internal flows to model. The cylinder was chosen because analytic solutions exist for pressure distribution over a two-dimensional cylinder for both the nonlifting and the lifting case (5).

The case of a cylinder outside the tunnel was run as a check case. The cylinder was given an aspect ratio of over 300 so that it approximated a two-dimensional cylinder at the mid-span location. The VSAERO prediction of the pressure distribution over the cylinder out of the tunnel was compared to the analytic solution to make sure that VSAERO predicted the correct solution out of the tunnel. Then the VSAERO solution for the cylinder inside the tunnel was compared to the analytic solution. Any differences between the two were then attributed to wall interference effects. The analytic solution was corrected using a standard solid blockage correction (6), and then compared again with the VSAERO solution. Thus it was possible to compare the wall interference effects predicted by VSAERO with classical wall interference corrections.

The paneled geometry of the cylinder in the tunnel is shown in Figure 28. Because of symmetry about the $y = 0$ plane, only half the tunnel and the cylinder was modeled. The cylinder had a span of 30 feet and a diameter of 1 foot. The cylinder was paneled with 36 divisions evenly spaced circumferentially and 10 divisions evenly spaced spanwise on the semispan. The tunnel had dimensions of 10 feet

high by 30 feet wide by 30 feet long. The cylinder was placed in the center of the tunnel. The tunnel was paneled with 10 equal divisions along the semi-width, 5 equal divisions along the height, and 7 equal divisions along the length of the tunnel starting from either end and stopping at a point 2 feet to either side of the center of the tunnel. The center portion of the tunnel was where the cylinder was joined to the wall of the tunnel, and this section required special care in the paneling. The details of the cylinder/wall juncture paneling can be seen in the inset of Figure 28. The velocities on the inlet face and fan face were specified so as to yield a velocity of 1.0 in the empty duct. The onset flow was set to 1.0 and the far-field factor was set to 10.

Figure 29 shows the paneling for the cylinder out of the tunnel. The paneling was exactly the same as for the cylinder in the tunnel for the inboard 15 feet of the cylinder. An extension to the cylinder was added to increase the aspect ratio of the cylinder to 300 so that the end effects would not influence the pressure distribution at the mid-span location on the cylinder. This way the center portion of the cylinder behaved as a two-dimensional cylinder.

Figures 30 and 31 show the results for the cylinder with no lift out of the tunnel and in the tunnel, respectively. As can be seen from Figure 30, the VSAERO prediction of pressure distribution over the two dimensional cylinder outside the tunnel agreed extremely well with the analytic solution. The two curves lay virtually on top of each other. Figure 31 shows the comparison of the VSAERO pressure distribution to the analytic solution for the cylinder in the tunnel. In this case the pressure coefficients predicted by VSAERO were slightly higher than the analytic solution in the region of peak pressure. A standard solid blockage correction for the cylinder in the tunnel was calculated as described in (6) and applied to the analytic solution. Once the blockage correction was applied to the analytic solution, the VSAERO pressure distribution agreed quite well with the analytic solution as can be seen in Figure 32. Hence, for the case of a nonlifting body in a tunnel, VSAERO accurately predicted wall interference effects.

The VSAERO prediction for pressure distribution over a cylinder carrying lift was also compared to an analytic solution (5). In VSAERO, lift can be induced on a cylinder by displacing the separation point of the wake through a given angle as shown in Figure 29. The analytic solution predicts pressure distribution over the surface of the cylinder as a function of separation angle of the wake. Hence, by displacing the wake to a known separation angle in the VSAERO model, a comparison can be made between the VSAERO pressure distribution and the analytic solution. In the present study, the wake was displaced to a separation angle of 40 degrees. This angle was chosen because it creates a large lift coefficient (about ± 8.0 with the sign depending on which direction the wake is displaced) on the cylinder. Thus the ability of VSAERO to predict internal flow fields which contain a body generating a large amount of lift was tested.

Figure 33 shows the comparison between the VSAERO pressure distribution and the analytic solution for the cylinder, with lift, out of the tunnel. The agreement between the VSAERO results and the analytic solution was excellent. The small differences in the region of peak pressure were due to the influence of the very strong end effects still being felt slightly at the mid-span location on the cylinder. These differences could be eliminated if the cylinder were made even longer. Figure 34 shows the comparison between the VSAERO pressure distribution and the analytic solution for the cylinder carrying lift in the tunnel. The VSAERO prediction of pressure coefficients was slightly high in the peak pressure region due to the influence of the walls of the tunnel. When the theoretical pressure coefficients were corrected to take into account the solid blockage effect, the VSAERO results agreed almost exactly with the theoretical results as shown in Figure 35. Thus it appears that VSAERO can handle internal flow problems involving bodies generating a large amount of lift.

NACA 4412 Wing in 7 × 10 Wind Tunnel

The second test case involved modeling a two dimensional NACA 4412 wing in the Army 7 × 10 foot wind tunnel at NASA Ames Research Center (9). The NACA

4412 wing was being run in the 7 × 10 wind tunnel to test a three-component laser doppler velocimeter. During the test, pressure measurements on the surface of the wing were also taken at various angles-of-attack. VSAERO was used to model the contraction, test section, and diffuser of the 7 × 10 wind tunnel and the NACA 4412 wing installed in the test section. The pressure distribution predicted by VSAERO was compared to the experimental pressure distribution over the wing for angles-of-attack of 0 degrees and 4 degrees. Low angles-of-attack were chosen to minimize any differences between the VSAERO results and the experimental results due to flow separation on the upper surface of the wing.

The 7 × 10 tunnel was paneled with 8 equally spaced divisions circumferentially on the top and bottom walls and 10 equally spaced divisions circumferentially on the side wall. The upstream duct, which is 20 feet long had 7 equally spaced divisions in the axial direction. The contraction, which is 43 feet long, had 5 divisions with full cosine spacing in the axial direction in the first 3 feet of the contraction and then 30 approximately equally spaced divisions in the axial direction over the rest of the contraction. The test section,which is 15 feet long, had 7 equally spaced divisions in the axial direction. The diffuser, which is 96 feet long, had 23 equally spaced divisions in the axial direction. The wing/wall juncture required special paneling. The details of this paneling can be seen in the inset of Figure 36. The NACA 4412 wing was paneled with 5 divisions using half cosine spacing starting at the leading edge in the chordwise direction for the first 10 percent of the chord and 21 divisions equally spaced in the chordwise direction for the last 90 percent of the chord, top and bottom. The wing had 5 divisions equally spaced in the spanwise direction. A total of 2512 panels were used to model the geometry. The paneled geometry is shown in Figure 36. The normal velocities were set on the inlet face and the fan face so that an empty test section velocity of 1.0 resulted. The onset flow was set to .35 and the far-field factor was set to 10.

In order to calculate pressure coefficients, VSAERO uses a reference velocity of 1.0 to nondimensionalize the pressures. The experimental pressure coefficients were nondimensionalized with a velocity obtained from static pressure readings off

the side walls of the tunnel one foot upstream of beginning of the test section. The velocity used to nondimensionalize the experimental results was different than the velocity used to nondimensionalize the VSAERO results. Therefore the experimental results were adjusted so that they were also nondimensionalized by a reference velocity of 1.0.

Figures 37 and 38 show the comparison between the VSAERO pressure distribution and the experimental pressure distribution for angles-of-attack of 0 degrees and 4 degrees respectively. For the case of 0 degrees angle-of-attack, the agreement was excellent between the VSAERO and experimental results. For the case of 4 degrees angle-of-attack, the agreement between the VSAERO and experimental results was also good. The only major difference was that VSAERO tended to overpredict the the peak pressure at the leading edge of the wing. Part of this difference can probably be attributed to boundary layer transition strips placed at the leading edge of the wing on the experimental model. There could be a laminar separation and turbulent reattachment of the boundary layer in this region. The above results indicate that VSAERO can correctly predict the flow field for a nonsymmetric wing in a tunnel consisting of a contraction, test section and diffuser.

One-Tenth Scale Vane Set 5 Model

The most complicated internal flow problem modeled with VSAERO was the one-tenth scale model of vane set 5. Vane set 5 is the set of turning vanes in the NFAC that was redesigned following a catastrophic failure. Part of the redesign process involved testing the new vane design in a wind tunnel. A one-tenth scale model of 8 of the new vanes was tested in a wind tunnel at NASA Ames Research Center (11). During the wind tunnel test, the pressure distribution over selected vanes was measured. In the present study, VSAERO was used to model the wind tunnel test of the one-tenth scale model of vane set 5. The pressure distribution predicted by VSAERO over selected vanes was compared with the experimental results.

The VSAERO model was composed of a tunnel with a 45 degree bend in it and a set of 8 turning vanes in the tunnel attached wall to wall. Only half the tunnel and vanes had to be modeled due to symmetry about the $y = 0$ plane. The vanes were positioned at the 45 degree bend to turn the flow. The vanes were equally spaced and were all at the same angle-of-attack. At the inlet the tunnel was 38.25 feet wide and 36 feet high. At the exit the tunnel was 36.66 feet wide and 36 feet high. The paneled model can be seen in Figure 39. There were three equally spaced divisions circumferentially on the side walls of the tunnel and eight equally spaced divisions circumferentially on the ceiling of the tunnel. The panels on the walls and ceiling of the tunnel had an aspect ratio of approximately one. Special paneling was required in the region where the vanes attach to the tunnel walls. The paneling on the ceiling between vanes matched the chordwise paneling on the vanes so that there were no gaps at the vane/tunnel juncture. The inner and outer corners of the tunnel were immediately adjacent to turning vanes and hence were paneled more densely than the rest of the tunnel. Both corners were paneled with 6 equally spaced circumferential divisions and 6 equally spaced axial divisions. The vanes were paneled with 14 divisions in the chordwise direction using full cosine spacing top and bottom and 4 equally spaced divisions in the spanwise direction. The total number of panels used to model the tunnel and the turning vanes was 1650. The normal velocity on the fan face was set to 1.0 and the normal velocity on the inlet face was set to balance mass flow. The far-field factor was set to 10 and the onset flow was set to 1.0. The entire tunnel geometry was oriented so that the onset velocity was perpendicular to the stagger line of the vanes.

Figures 40 and 41 show the comparison of the VSAERO pressure distribution and the experimental pressure distribution over the surfaces of vanes 6 and 8 respectively. Vane 8 is the vane closest to the lower corner of the 45 degree bend in the tunnel in Figure 39 and vane 6 is two vanes up from vane 8. The solid line represents the VSAERO solution and the dotted line represents experimental results. Agreement was excellent between the VSAERO and experimental results for both vane 6 and vane 8 except near the trailing edge of the vane. This is because there

was separation at the trailing edge of the vanes as can be seen from the experimental results. When comparing the VSAERO and experimental plots of pressure coefficients, it should be remembered that there will be small differences due to viscous effects and turbulence in the tunnel that VSAERO cannot model. Because VSAERO is a potential flow code, the solution will not reflect viscous effects such as separation; however, VSAERO does have an integral boundary layer option along surface streamlines as described in the theory section of this report. If the boundary layer option is exercised, VSAERO can calculate an approximate separation point on the vanes. This option was run and it was found that VSAERO predicted the separation point with surprising accuracy. For vane 6 VSAERO predicted a separation point of $x = 15.32$ which was very close to the experimental separation point of approximately $x = 15.5$ shown in Figure 40. Similarly for vane 8 VSAERO predicted a separation point at $x = 18.89$, which was slightly less than the experimental separation point at approximately $x = 19.0$ shown in Figure 41. From these results it can be concluded that VSAERO can accurately handle complex internal flows as long as they do not involve large viscous effects.

CHAPTER 5
CONCLUSIONS

An evaluation of the ability of a low order panel method to predict internal flow fields has been made. The computer code VSAERO was used as the basis for the evaluation. Guidelines for modeling the geometry were determined and the effects of varying the boundary conditions and using numerical approximations were studied. Several test cases of lifting bodies in tunnels were run and the results compared with theoretical or experimental results in order to validate the ability of the code to predict complex internal flow fields.

The geometry of an internal flow problem should be modeled as a closed box with all the unit normal vectors to the panels pointing into the box. Exceptions to this rule would be modeling tunnel inlets or similar internal flows where it is not possible to model the geometry with a closed box. In this case the geometry should be modeled with an inner and an outer surface and one open end. For the usual case of modeling the geometry as a closed box, the normal velocities should be specified on both an inlet face and an exit face so that continuity is satisfied. Overlaps and gaps in the paneling should be avoided, especially in regions such as a wing/wall juncture. Sharp corners in the surface paneling should also be avoided as these discontinuities cause large local spikes in the pressure distribution on the surface. The geometry should be input starting from one end of the tunnel and working to the other end in a circumferential manner. This helps prevent large elements from appearing far away from the diagonal in the influence coefficient matrix. There should be high panel density in contraction and diffusion regions of a tunnel and the transitions from regions of low panel density to high panel density should be made smoothly.

The internal Dirichlet boundary condition is determined by the setting of the onset flow. For the case of the tunnel modeled as a closed box, the onset flow can be

set independently of the flow in the tunnel. The setting of the onset flow directly affects the amount of leakage from the tunnel. The onset flow should be set so that the tunnel conserves mass. From the results of the present study it appears best to start with the onset flow set approximately equal to the average velocity through the tunnel and iterate from there until the tunnel conserves mass. The tunnel conserves mass when the onset flow comes closest to matching the overall flow in the tunnel. One way that the code VSAERO could be improved would be to allow for a variable onset flow. In this way the onset flow could be set to better match the flow through the tunnel and the code would yield better results without having to iterate.

The value of the far-field factor affects both the value to which the onset flow is set and the accuracy of the solution. The default value of 5 for the far-field factor is not large enough to yield accurate results for some internal flow problems. Increasing the far-field factor yields more accurate results for scan plane velocities, but it also increases computation time. The onset flow must also be readjusted to eliminate leakage when the far-field factor is changed. As the far-field factor is increased, the onset flow needed to eliminate leakage decreases.

The error induced in the influence coefficients by using the far-field approximation was investigated. The error was found to be a function of the type of influence coefficient, the far-field factor, and the aspect ratio of the panel containing the singularities. B_{JK} showed the least sensitivity to the far-field approximation. The error induced in C_{JK} and $\bar{V}_{\sigma_{rK}}$ using the far-field approximation was approximately twice the error in B_{JK} for any given far-field factor. The error was the highest for $\bar{V}_{\mu_{rK}}$, being 4 to 10 times higher than that for the error for B_{JK} at any given far-field factor. At present VSAERO uses the same far-field factor for all four influence coefficients. Because the far field approximation does save considerable computation time, it would be beneficial to set the far-field factor for B_{JK} and multiply that far-field factor by some constant to obtain the far-field factors for the other influence coefficients. The constants suggested by the results of the present study are 1.5 for C_{JK} and $\bar{V}_{\sigma_{rK}}$ and 2.0 for $\bar{V}_{\mu_{rK}}$. Increasing the aspect ratio of the panel

with the distributed singularities also increases the error in the influence coefficients when the far-field approximation is used. When the aspect ratio is increased by a factor of 4, the error increases by about a factor of 2 at any given far-field factor. Thus, high aspect ratio panels should be avoided if possible. If the geometry must contain many high aspect ratio panels, the far-field factor should be increased to assure accurate results. Another method of reducing computation time required for a given degree of accuracy would be to specify an increased far-field factor for only the high aspect ratio panels, rather than for all the panels. The far-field factor could be doubled if the aspect ratio of a given panel is larger than a certain value.

When the above guidelines are followed, VSAERO does an excellent job of predicting complex internal flow fields. Test cases were run of a cylinder in a straight tunnel, both with and without lift on the cylinder, a nonsymmetric wing in a tunnel with a contraction, test section, and diffuser, and a set of turning vanes in a tunnel with a 45 degree bend in it. For the cylinder in the tunnel, VSAERO predicted the correct pressure distribution over the cylinder, both with and without lift. The wall interference effect was also correctly predicted by VSAERO for the cylinder in the straight duct. The test case of the NACA 4412 wing in a tunnel with a contraction, test section, and diffuser showed the ability of VSAERO to predict an internal flow field which has large changes in velocity magnitude in the axial direction. The last test case demonstrated VSAERO's ability to predict internal flow fields for a cascade of airfoils in a tunnel with a 45 degree bend in it. Low order panel methods can serve as a valuable tool for predicting complex three-dimensional internal flow fields provided the geometry is modeled correctly and the correct boundary conditions and approximations are used, as outlined in this report.

REFERENCES

(1) Maskew, B. "Program VSAERO, A Computer Program for Calculating the Non-Linear Characteristics of Arbitrary Configurations, Users Manual," NASA CR 166476, December 1982.

(2) Maskew, B. "Program VSAERO, A Computer Program for Calculating the Non-Linear Characteristics of Arbitrary Configurations, Theory Document," NASA CR to be published.

(3) Hunt, B. and Holt, D.R. "The Use of Panel Methods for the Evaluation of Subsonic Wall Interference," Wall Interference in Wind Tunnels, AGARD Conference Proceedings 335, September 1982.

(4) Hunt, B. "The Panel Method for Subsonic Aerodynamic Flows: A Survey of Mathematical Formulations and Numerical Models and an Outline of the New British Aerospace Scheme," Von Karman Institute for Fluid Dynamics, Lecture Series 1978-4, Vol.I, March 13-17, 1978.

(5) Kuethe, A.M. and Schetzer, J.D. Foundations of Aerodynamics, 2nd ed. New York: John Wiley and Sons Inc., 1959, 66-73.

(6) Rae, W. and Pope, A. Low-Speed Wind Tunnel Testing, 2nd ed. New York: John Wiley and Sons Inc., 1984, 353-361.

(7) Corsiglia, V.R., Olson, L.E., and Falarski, M.D. "Aerodynamic Characteristics of the 40 by 80/80 by 120-Foot Wind Tunnel at NASA Ames Research Center," NASA TM 85946, April 1984.

(8) Ross, J.C. "Prediction of Vortex-Induced Loads on Wind Tunnel Turning Vanes," NASA TM 86678, March 1985.

(9) Wadcock, A. "Three-Component LDA Measurements in the Boundary Layer and Wake of a Stalled Airfoil," NASA CR to be published.

(10) Bratkovich, A. and Marshall, F.J. "Iterative Techniques for the Solution of Large Linear Systems in Computational Aerodynamics," Journal of Aircraft, vol. 12, no. 2, February 1975, 116-118.

(11) Olson, L.E. Private communication, NASA Ames Research Center, 1985.

APPENDIX A
CALCULATION OF INFLUENCE COEFFICIENTS

In the program VSAERO there are two types of influence coefficients: velocity potential influence coefficients and velocity influence coefficients. Both types of influence coefficients are evaluated for the influence due to doublets and the influence due to sources. Thus there are four separate influence coefficient calculations to be made. The influence coefficients can be calculated exactly or using a far-field approximation. In the exact solution, the doublets and sources are treated as being distributed uniformly over the surface of a panel K. The integrals for the influence coefficients are then evaluated over the entire surface of panel K. A detailed description of the method of integration can be found in Reference 3. First, the following definitions are made.

$$RNUM = SM \times PN \times (B \times PA - A \times PB)$$

$$DNOM = PA \times PB + PN^2 \times A \times B \times SM^2$$

$$PA = PN^2 \times SL + A1 \times AM$$

$$PB = PN^2 \times SL + A1 \times BM$$

$$PN = \vec{P}_{JK} \cdot \hat{n}_K$$

$$RJ3 = \frac{1}{s} LOG\left|\frac{A+B+s}{A+B-s}\right|$$

$$SL = \vec{s} \cdot \hat{l}$$

$$SM = \vec{s} \cdot \hat{m}$$

$$AL = \vec{a} \cdot \hat{l}$$

$$AM = \vec{a} \cdot \hat{m}$$

$$BM = \vec{b} \cdot \hat{m}$$

$$A1 = AM \times SL - AL \times SM$$

$\vec{P}_{JK}$ = vector between control point K and control point J or scan point P

$s = |\vec{s}|$

$A = |\vec{a}|$

$B = |\vec{b}|$

$\vec{s}$ = the vector representing a given side of panel K

$\vec{a}$ = the position vector of control point J relative to the start of $\vec{s}$

$\vec{b}$ = the position vector of control point J relative to the end of $\vec{s}$

i = the side number of panel K

$\hat{l}, \hat{m}, \hat{n}$ = the coordinate axes of panel K (see Figure 16)

The resulting equations for the exact influence coefficients can then be expressed as:

$$C_{JK} = \sum_{i=1}^{4} C_{JKi}$$

where

$$C_{JKi} = tan^{-1}(RNUM/DNOM)$$

$$B_{JK} = \sum_{i=1}^{4} B_{JKi}$$

where

$$B_{JKi} = A1 \times RJ3 - PN \times C_{JKi}$$

$$\vec{V}_{\mu_{PK}} = \sum_{i=1}^{4} \vec{V}_{\mu_{PK_i}}$$

where

$$\vec{V}_{\mu_{PK_i}} = \frac{\vec{a} \times \vec{b} \times (A + B)}{A \times B \times (A \times B + \vec{a} \cdot \vec{b})}$$

$$\vec{V}_{\sigma_{PK}} = \sum_{i=1}^{4} \vec{V}_{\sigma_{PK_i}}$$

where

$$\vec{V}_{\sigma_{PK_i}} = RJ3 \times (SM \times \hat{l} - SL \times \hat{m}) + C_{JK_i} \times \hat{n}$$

There is a limiting case for C_{JK} when PN goes to zero:

$\lim_{PN \to 0^+} (C_{JK_i}) = \pm\pi$ if $DNOM < 0$

$\lim_{PN \to 0^+} (C_{JK_i}) = \pm\pi/2$ if DNOM $= 0$

$\lim_{PN \to 0^+} (C_{JK_i}) = 0$ if $DNOM > 0$

The positive sign is used if the point P is to the right of the side as you look in the direction of the side, and the negative sign is used if point P is to the left of the side. If $PN \to 0^-$, all the signs on π are reversed.

When the far-field approximation is used, the singularities are treated as point doublets and point sources. With this approximation, all the integrands in the integrals for the influence coefficients become constants. Thus, using the far-field approximation, the equations for the influence coefficients become:

$$C_{JK} = PN \times AREA_K / {P_{JK}}^3$$

$$B_{JK} = AREA_K / P_{JK}$$

$$\vec{V}_{\mu_{PK}} = AREA_K \times (3 \times PN \times \vec{P}_{JK} - {P_{JK}}^2 \times \hat{n}_K) / {P_{JK}}^5$$

$$\bar{V}_{\sigma_{JK}} = AREA_K \times \bar{P}_{JK}/P_{JK}{}^3$$

A computer program was written to evaluate the percent difference between the exact influence coefficients and the ones calculated using the far-field approximation for different panel orientations and positions. The program is written in Fortran 77. The input for the program consists of the vectors for the sides of panel K, which must be rectangular in this program, the normal vector to panel J, the plane of panel K which is being examined, and the elevation angle of panel J above the plane of panel K. The program evaluates the percent error in the influence coefficients at preset far-field factors of 2, 4, 6, 8, and 10. The output for the program consists of a file containing the input information, the values of the exact and the approximate influence coefficients, and the error between the two. The velocity influence coefficients are broken up into their three components and each component is examined separately. Eight other files, one for each velocity potential influence coefficient and one for each component of the velocity influence coefficients, are also output and they contain only position coordinates and error. These files are set up as input data for a contour plotting routine so that the data may be plotted. The program listing follows.

```
      PROGRAM VELINF
C
C     INITIALIZE ARRAYS AND CHARACTER VARIABLES
C
      CHARACTER*15 FN1,FN2,FN3,FN4,FN5,FN6,FN7,FN8,FN9,FN10
      DIMENSION S(4,3),ACB(3),FFVD(3),RNJ(3),A(3),B(3),P(3),CJK(5)
      DIMENSION BJK(5),VD(5,3),VS(5,3),FFVS(3)
C
C     INPUT DATA FROM DATAFILE INFLUCO.DAT
C
      OPEN(1,FILE='INFLUCO.DAT',TYPE='OLD',READONLY)
      READ(1,*)S(1,1),S(1,2),S(1,3)
      READ(1,*)S(2,1),S(2,2),S(2,3)
      READ(1,*)S(3,1),S(3,2),S(3,3)
      READ(1,*)S(4,1),S(4,2),S(4,3)
      READ(1,*)RNJ
      READ(1,*)THETA1
      READ(1,*)KK
      READ(1,3000)FN1
      READ(1,3000)FN2
      READ(1,3000)FN3
      READ(1,3000)FN4
      READ(1,3000)FN5
      READ(1,3000)FN6
      READ(1,3000)FN7
      READ(1,3000)FN8
      READ(1,3000)FN9
      READ(1,3000)FN10
C
C     INITIALIZE VARIABLES AND BEGIN RADIUS LOOP
C
      KKL=1
      THETA=THETA1*3.141592654/180.
      SMP=S(1,1)/2
      SMQ=S(2,2)/2
      DS=SMP+SMQ
      DO 30 L=2,10,2
      RFF=L
      D=RFF*DS
C
C     BEGIN EXACT CALCULATION OF INFLUENCE COEFFIENTS
C
      IF(KK.EQ.1)THEN
      P(1)=D*COS(THETA)
      P(2)=0.0
      P(3)=D*SIN(THETA)
      ELSEIF(KK.EQ.2)THEN
      P(1)=0.0
      P(2)=D*COS(THETA)
      P(3)=D*SIN(THETA)
      ELSE
      P(1)=D*COS(THETA)
      P(2)=D*SIN(THETA)
      P(3)=0.0
      ENDIF
      A(1)=P(1)+S(1,1)/2
      A(2)=P(2)+S(2,2)/2
      A(3)=P(3)
C
C     LOOP THROUGH THE FOUR SIDES OF PANEL K
C
      DO 10 I=1,4
      B(1)=A(1)-S(I,1)
```

```
      B(2)=A(2)-S(I,2)
      B(3)=A(3)-S(I,3)
      RA=SQRT(A(1)**2+A(2)**2+A(3)**2)
      RB=SQRT(B(1)**2+B(2)**2+B(3)**2)
      RP=SQRT(P(1)**2+P(2)**2+P(3)**2)
      RS=SQRT(S(I,1)**2+S(I,2)**2+S(I,3)**2)
      A1=A(2)*S(I,1)-A(1)*S(I,2)
      PA=P(3)**2*S(I,1)+A1*A(2)
      PB=P(3)**2*S(I,1)+A1*B(2)
      RNUM=S(I,2)*P(3)*(RB*PA-RA*PB)
      DNOM=PA*PB+P(3)**2*RA*RB*S(I,2)**2
C
C     TEST TO DETERMINE IF PN=0 AND WHAT DNOM IS
C
      IF(I.EQ.1.AND.P(3).EQ.0)THEN
          IF(DNOM.LE.0.0)THEN
              IF(P(2).GT.-S(2,2)/2)THEN
              CJK(I)=-3.141593
              IF(DNOM.EQ.0.0)CJK(I)=CJK(I)/2
              ELSE
              CJK(I)=3.141593
              IF(DNOM.EQ.0.0)CJK(I)=CJK(I)/2
              ENDIF
          ELSE
          CJK(I)=0.0
          ENDIF
      ENDIF
      IF(I.EQ.2.AND.P(3).EQ.0)THEN
          IF(DNOM.LE.0.0)THEN
              IF(P(1).LT.S(1,1)/2)THEN
              CJK(I)=-3.141593
              IF(DNOM.EQ.0.0)CJK(I)=CJK(I)/2
              ELSE
              CJK(I)=3.141593
              IF(DNOM.EQ.0.0)CJK(I)=CJK(I)/2
              ENDIF
          ELSE
          CJK(I)=0.0
          ENDIF
      ENDIF
      IF(I.EQ.3.AND.P(3).EQ.0)THEN
          IF(DNOM.LE.0.0)THEN
              IF(P(2).LT.S(2,2)/2)THEN
              CJK(I)=-3.141593
              IF(DNOM.EQ.0.0)CJK(I)=CJK(I)/2
              ELSE
              CJK(I)=3.141593
              IF(DNOM.EQ.0.0)CJK(I)=CJK(I)/2
              ENDIF
          ELSE
          CJK(I)=0.0
          ENDIF
      ENDIF
      IF(I.EQ.4.AND.P(3).EQ.0)THEN
          IF(DNOM.LE.0.0)THEN
              IF(P(1).GT.-S(1,1)/2)THEN
              CJK(I)=-3.141593
              IF(DNOM.EQ.0.0)CJK(I)=CJK(I)/2
              ELSE
              CJK(I)=3.141593
              IF(DNOM.EQ.0.0)CJK(I)=CJK(I)/2
              ENDIF
          ELSE
```

```
            CJK(I)=0.0
            ENDIF
          ENDIF
          IF(P(3).EQ.0.0)GO TO 100
          CJK(I)=ATAN2(RNUM,DNOM)
  100     T=ABS((RA+RB+RS)/(RA+RB-RS))
          RJ3=(1/RS)*ALOG(T)
          BJK(I)=A1*RJ3-P(3)*CJK(I)
          ADB=A(1)*B(1)+A(2)*B(2)+A(3)*B(3)
          ACB(1)=A(2)*B(3)-B(2)*A(3)
          ACB(2)=A(3)*B(1)-B(3)*A(1)
          ACB(3)=A(1)*B(2)-B(1)*A(2)
          T1=(RA*RB+ADB)*RA*RB
          T2=(RA+RB)/T1
          VD(I,1)=ACB(1)*T2
          VD(I,2)=ACB(2)*T2
          VD(I,3)=ACB(3)*T2
          VS(I,1)=RJ3*S(I,2)
          VS(I,2)=-RJ3*S(I,1)
          VS(I,3)=CJK(I)
          A(1)=B(1)
          A(2)=B(2)
          A(3)=B(3)
   10     CONTINUE
C
C         INITIALIZE COUNTERS TO SUM CONTRIBUTIONS FROM EACH SIDE OF PANEL
C
          CJK(5)=0
          BJK(5)=0
          VD(5,1)=0
          VD(5,2)=0
          VD(5,3)=0
          VS(5,1)=0
          VS(5,2)=0
          VS(5,3)=0
          DO 20 I=1,4
          CJK(5)=CJK(5)+CJK(I)
          BJK(5)=BJK(5)+BJK(I)
          VD(5,1)=VD(5,1)+VD(I,1)
          VD(5,2)=VD(5,2)+VD(I,2)
          VD(5,3)=VD(5,3)+VD(I,3)
          VS(5,1)=VS(5,1)+VS(I,1)
          VS(5,2)=VS(5,2)+VS(I,2)
          VS(5,3)=VS(5,3)+VS(I,3)
   20     CONTINUE
          RS3=SQRT(S(3,1)**2+S(3,2)**2+S(3,3)**2)
          AK=RS*RS3
C
C         COMPUTE FAR FIELD INFLUENCE COEFFICIENTS
C
          FFCJK=P(3)*AK/RP**3
          FFBJK=AK/RP
          FFVD(1)=(3*P(3)*P(1)*AK)/RP**5
          FFVD(2)=(3*P(3)*P(2)*AK)/RP**5
          FFVD(3)=(3*P(3)**2-RP**2)*AK/RP**5
          T5=AK/RP**3
          FFVS(1)=P(1)*T5
          FFVS(2)=P(2)*T5
          FFVS(3)=P(3)*T5
C
C         CALCULATE ERRORS
C
          IF(CJK(5).NE.0.0)THEN
```

```
      ERRORC=((CJK(5)-FFCJK)*100/CJK(5))
      ELSE
      ERRORC=0
      ENDIF
      IF(BJK(5).NE.0)THEN
      ERRORB=((BJK(5)-FFBJK)*100/BJK(5))
      ELSE
      ERRORB=0
      ENDIF
      IF(VS(5,1).NE.0.0)THEN
      ERRORVS1=(VS(5,1)-FFVS(1))*100/VS(5,1)
      ELSE
      ERRORVS1=0
      ENDIF
      IF(VS(5,2).NE.0.0)THEN
      ERRORVS2=(VS(5,2)-FFVS(2))*100/VS(5,2)
      ELSE
      ERRORVS2=0
      ENDIF
      IF(VS(5,3).NE.0.0)THEN
      ERRORVS3=(VS(5,3)-FFVS(3))*100/VS(5,3)
      ELSE
      ERRORVS3=0
      ENDIF
      IF(VD(5,1).NE.0.0)THEN
      ERRORVD1=(VD(5,1)-FFVD(1))*100/VD(5,1)
      ELSE
      ERRORVD1=0
      ENDIF
      IF(VD(5,2).NE.0.0)THEN
      ERRORVD2=(VD(5,2)-FFVD(2))*100/VD(5,2)
      ELSE
      ERRORVD2=0
      ENDIF
      IF(VD(5,3).NE.0.0)THEN
      ERRORVD3=(VD(5,3)-FFVD(3))*100/VD(5,3)
      ELSE
      ERRORVD3=0
      ENDIF
C
C     OUTPUT THE RESULTS TO DATAFILES
C
      X=RFF*COS(THETA)
      Y=RFF*SIN(THETA)
      OPEN(2,FILE='INFLUCO.CPR',TYPE='NEW')
      WRITE(2,1000)S(1,1),S(1,2),S(1,3)
      WRITE(2,1001)S(2,1),S(2,2),S(2,3)
      WRITE(2,1002)S(3,1),S(3,2),S(3,3)
      WRITE(2,1003)S(4,1),S(4,2),S(4,3)
      WRITE(2,1004)P(1),P(2),P(3)
      WRITE(2,1005)RNJ(1),RNJ(2),RNJ(3)
      WRITE(2,1006)RFF,THETA1
      WRITE(2,2000)CJK(5),FFCJK,ERRORC
      WRITE(2,2001)BJK(5),FFBJK,ERRORB
      WRITE(2,2004)VS(5,1),FFVS(1),ERRORVS1
      WRITE(2,2005)VS(5,2),FFVS(2),ERRORVS2
      WRITE(2,2006)VS(5,3),FFVS(3),ERRORVS3
      WRITE(2,2007)VD(5,1),FFVS(1),ERRORVD1
      WRITE(2,2008)VD(5,2),FFVD(2),ERRORVD2
      WRITE(2,2009)VD(5,3),FFVD(3),ERRORVD3
      OPEN(21,FILE=FN1,TYPE='NEW')
      WRITE(21,4000)X,Y,ERRORC
      OPEN(22,FILE=FN2,TYPE='NEW')
```

```
      WRITE(22,4000)X,Y,ERRORB
      OPEN(25,FILE=FN5,TYPE='NEW')
      WRITE(25,4000)X,Y,ERRORVS1
      OPEN(26,FILE=FN6,TYPE='NEW')
      WRITE(26,4000)X,Y,ERRORVS2
      OPEN(27,FILE=FN7,TYPE='NEW')
      WRITE(27,4000)X,Y,ERRORVS3
      OPEN(28,FILE=FN8,TYPE='NEW')
      WRITE(28,4000)X,Y,ERRORVD1
      OPEN(29,FILE=FN9,TYPE='NEW')
      WRITE(29,4000)X,Y,ERRORVD2
      OPEN(30,FILE=FN10,TYPE='NEW')
      WRITE(30,4000)X,Y,ERRORVD3
C
C     FORMAT STATEMENTS
C
 1000 FORMAT(1X,'SIDE ONE:',F4.1,'L + ',F4.1,'M + ',F4.1,'N'/)
 1001 FORMAT(1X,'SIDE TWO:',F4.1,'L + ',F4.1,'M + ',F4.1,'N'/)
 1002 FORMAT(1X,'SIDE THREE:',F4.1,'L + ',F4.1,'M + ',F4.1,'N'/)
 1003 FORMAT(1X,'SIDE FOUR:',F4.1,'L + ',F4.1,'M + ',F4.1,'N'/)
 1004 FORMAT(1X,'VECTOR P:',F12.8,'L + ',F12.8,'M + ',F12.8,'N'/)
 1005 FORMAT(1X,'VECTOR RNJ:',F12.8,'L + ',F12.8,'M + ',F12.8,'N'/)
 1006 FORMAT(1X,'RFF= ',F4.1,'     THETA= ',F12.8)
 2000 FORMAT(//1X,'CJK=',F11.8,5X,'FFCJK=',F11.8,5X,'% ERROR=',F8.3/)
 2001 FORMAT(1X,'BJK=',F11.8,5X,'FFBJK=',F11.8,5X,'% ERROR=',F8.3/)
 2004 FORMAT(1X,'VSLPK=',F11.8,5X,'FFVSLPK=',F11.8,5X,'% ERROR=',F8.3/)
 2005 FORMAT(1X,'VSMPK=',F11.8,5X,'FFVSMPK=',F11.8,5X,'% ERROR=',F8.3/)
 2006 FORMAT(1X,'VSNPK=',F11.8,5X,'FFVSNPK=',F11.8,5X,'% ERROR=',F8.3/)
 2007 FORMAT(1X,'VDLPK=',F11.8,5X,'FFVDLPK=',F11.8,5X,'% ERROR=',F8.3/)
 2008 FORMAT(1X,'VDMPK=',F11.8,5X,'FFVDMPK=',F11.8,5X,'% ERROR=',F8.3/)
 2009 FORMAT(1X,'VDNPK=',F11.8,5X,'FFVDNPK=',F11.8,5X,'% ERROR=',F8.3/)
 3000 FORMAT(A)
 4000 FORMAT(1X,F10.1,F10.1,F10.3)
   30 CONTINUE
      STOP
      END
```

APPENDIX B

FIGURES

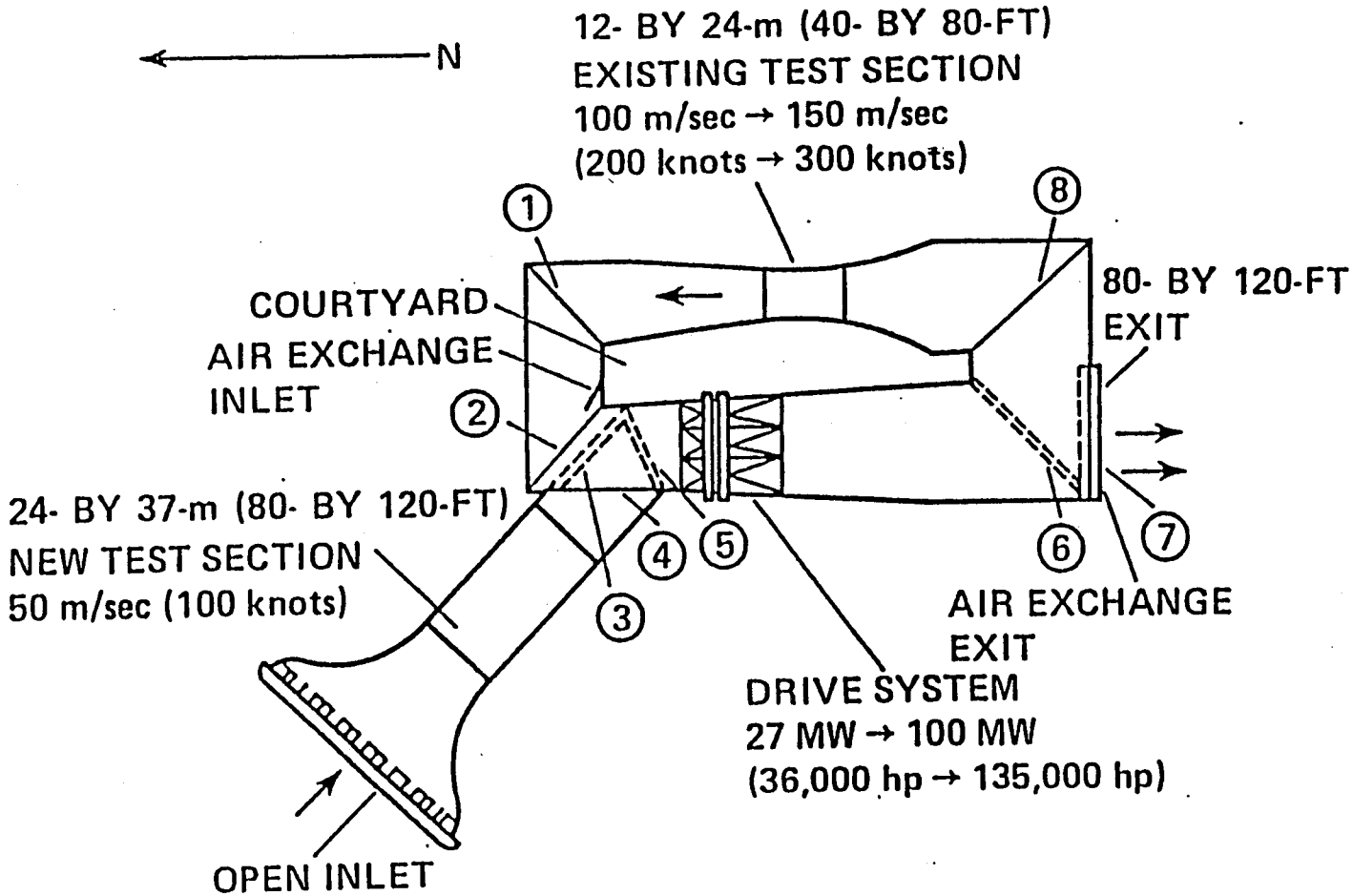

Figure 1 Plan View of the National Full-Scale Aerodynamics Complex (NFAC)

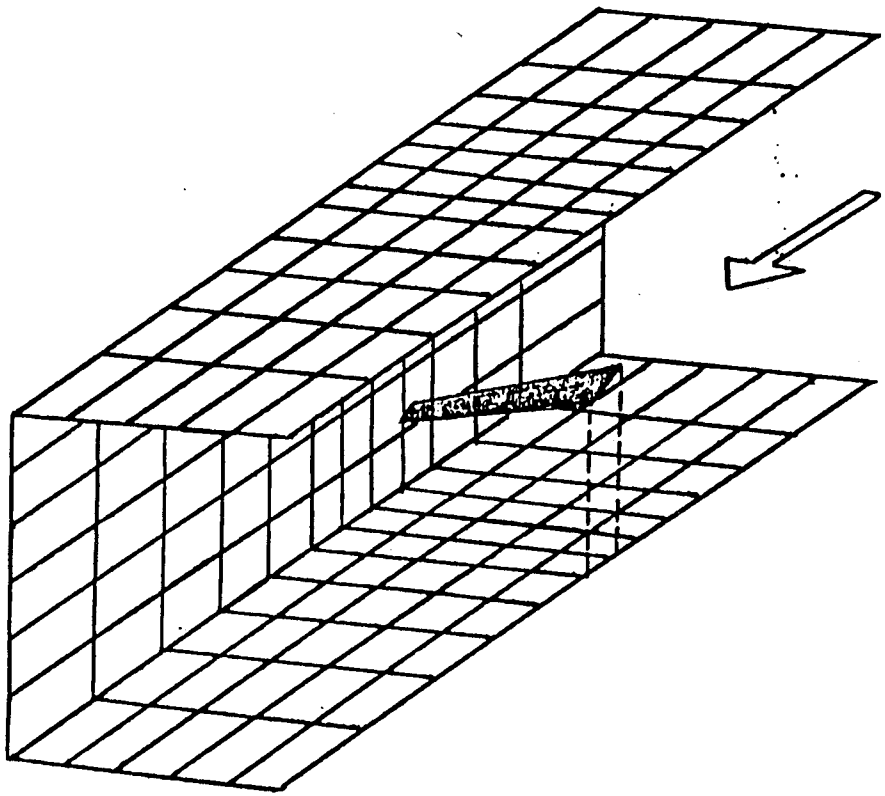

Figure 2 Tunnel Geometry Used by D.R. Holt and B. Hunt (3)

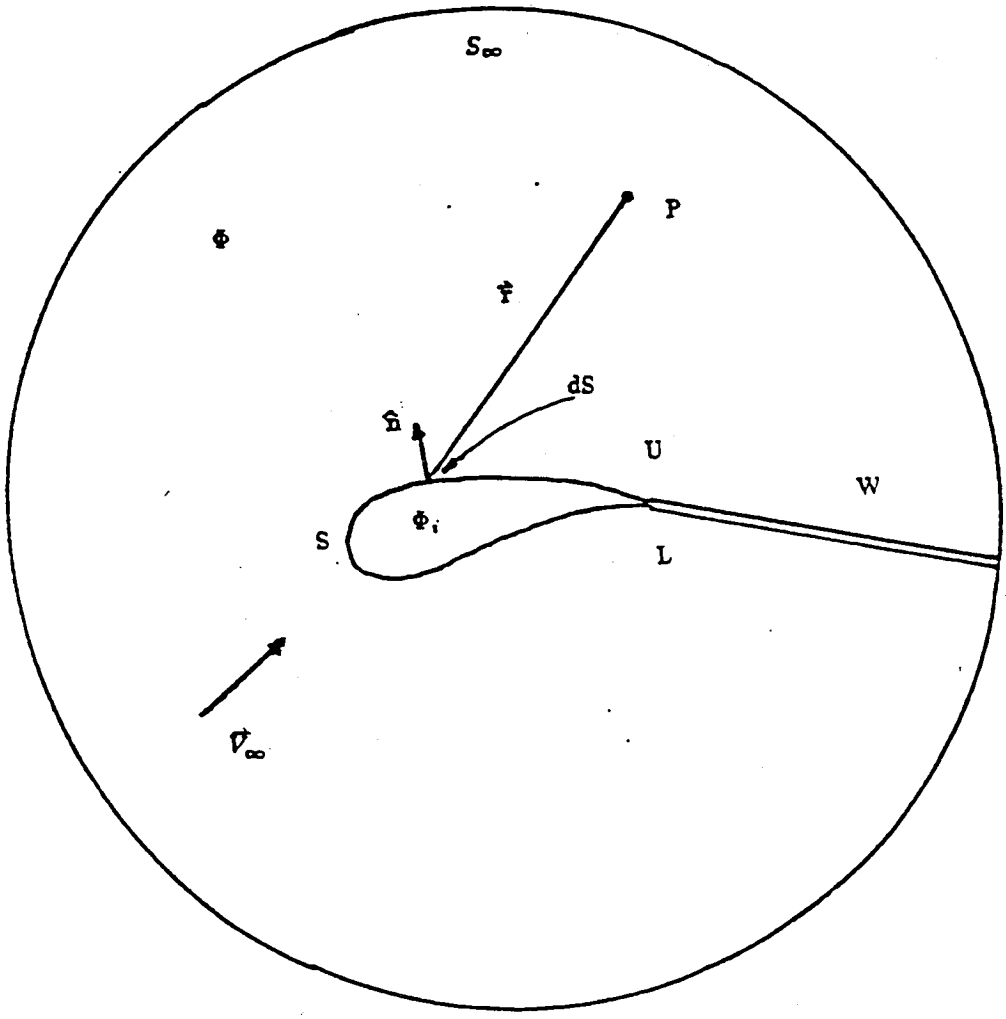

Figure 3 Section Through Idealized Flow Model

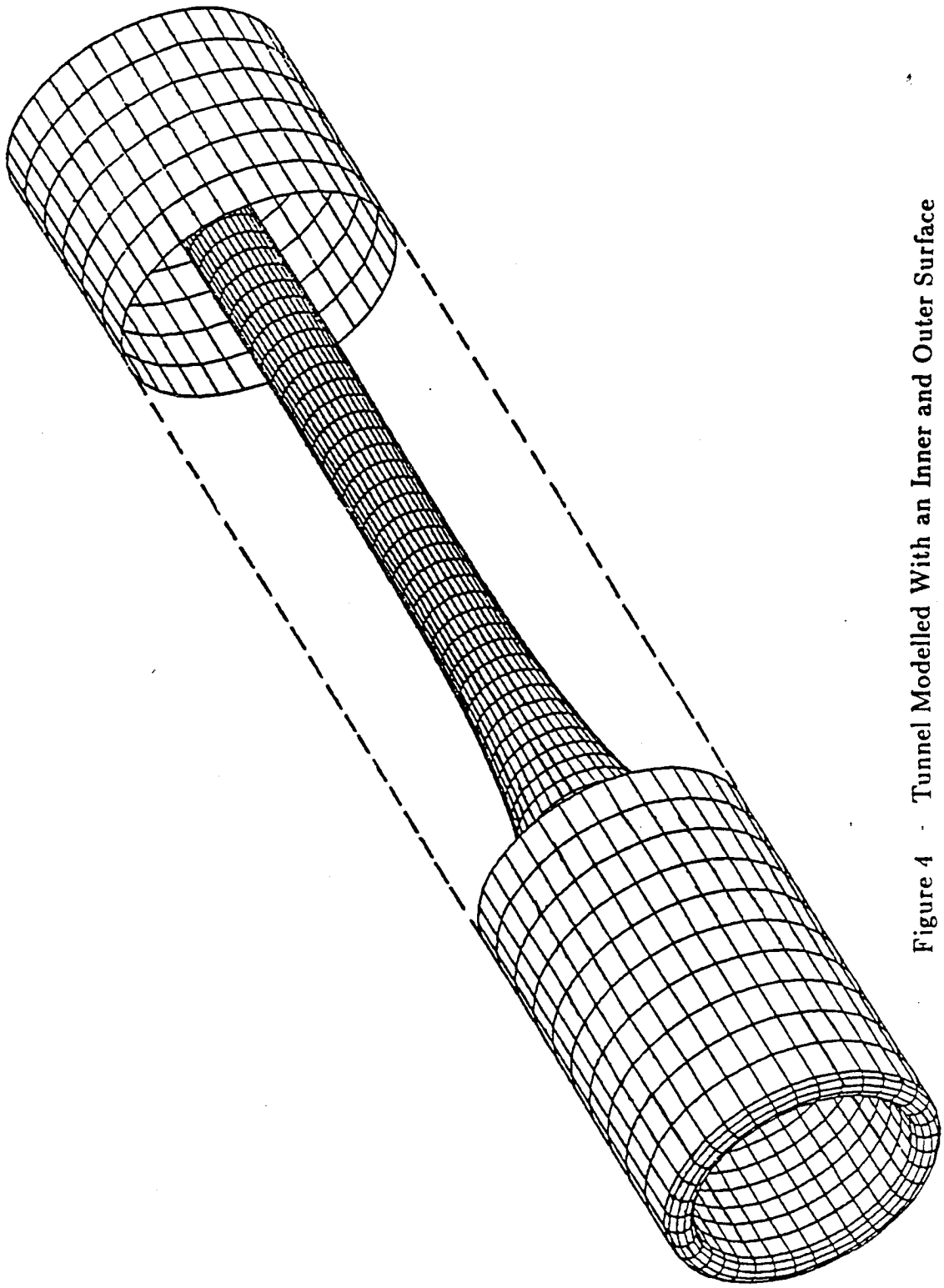

Figure 4 - Tunnel Modelled With an Inner and Outer Surface

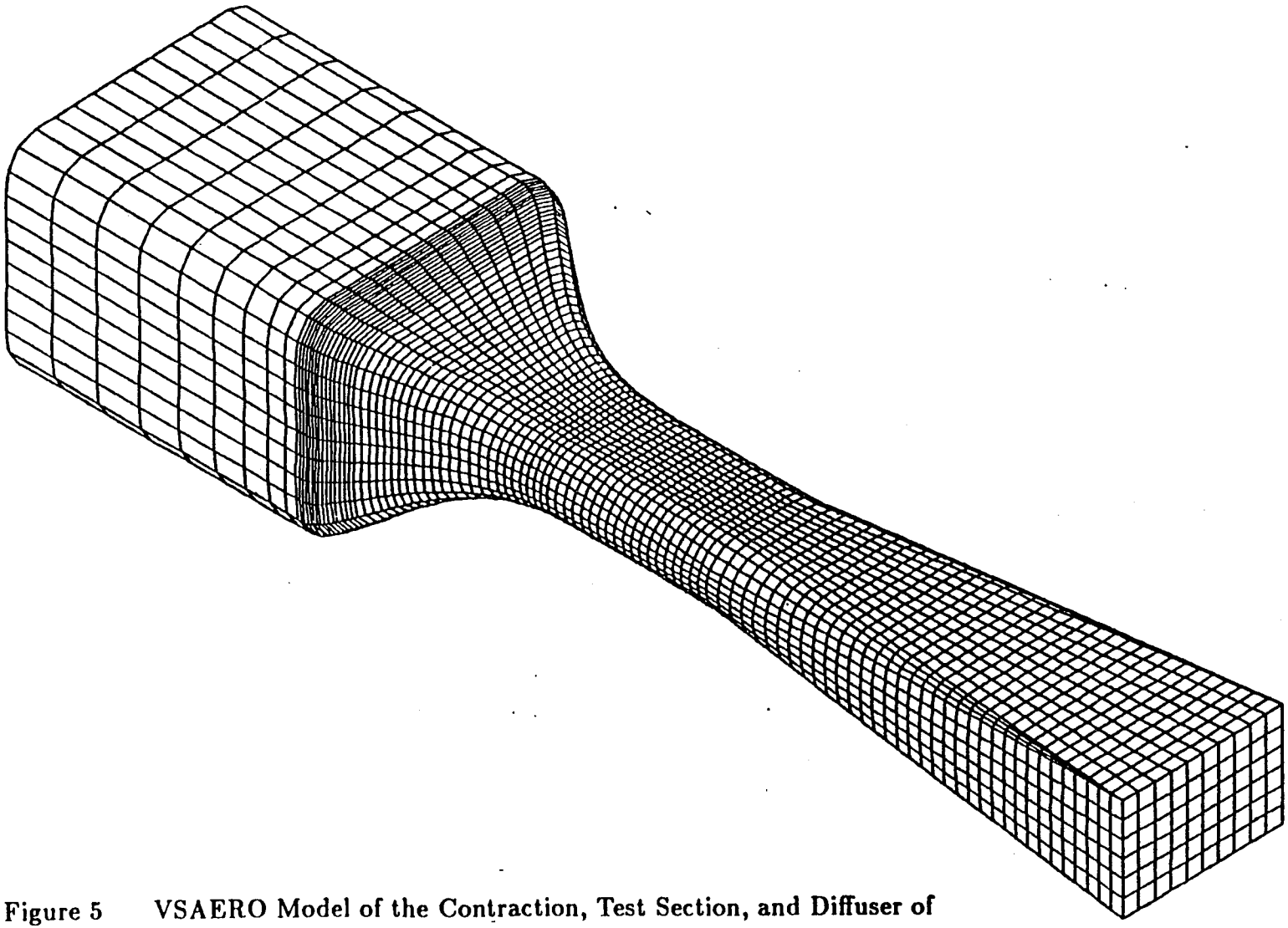

Figure 5 VSAERO Model of the Contraction, Test Section, and Diffuser of the 40 × 80 Circuit of the NFAC

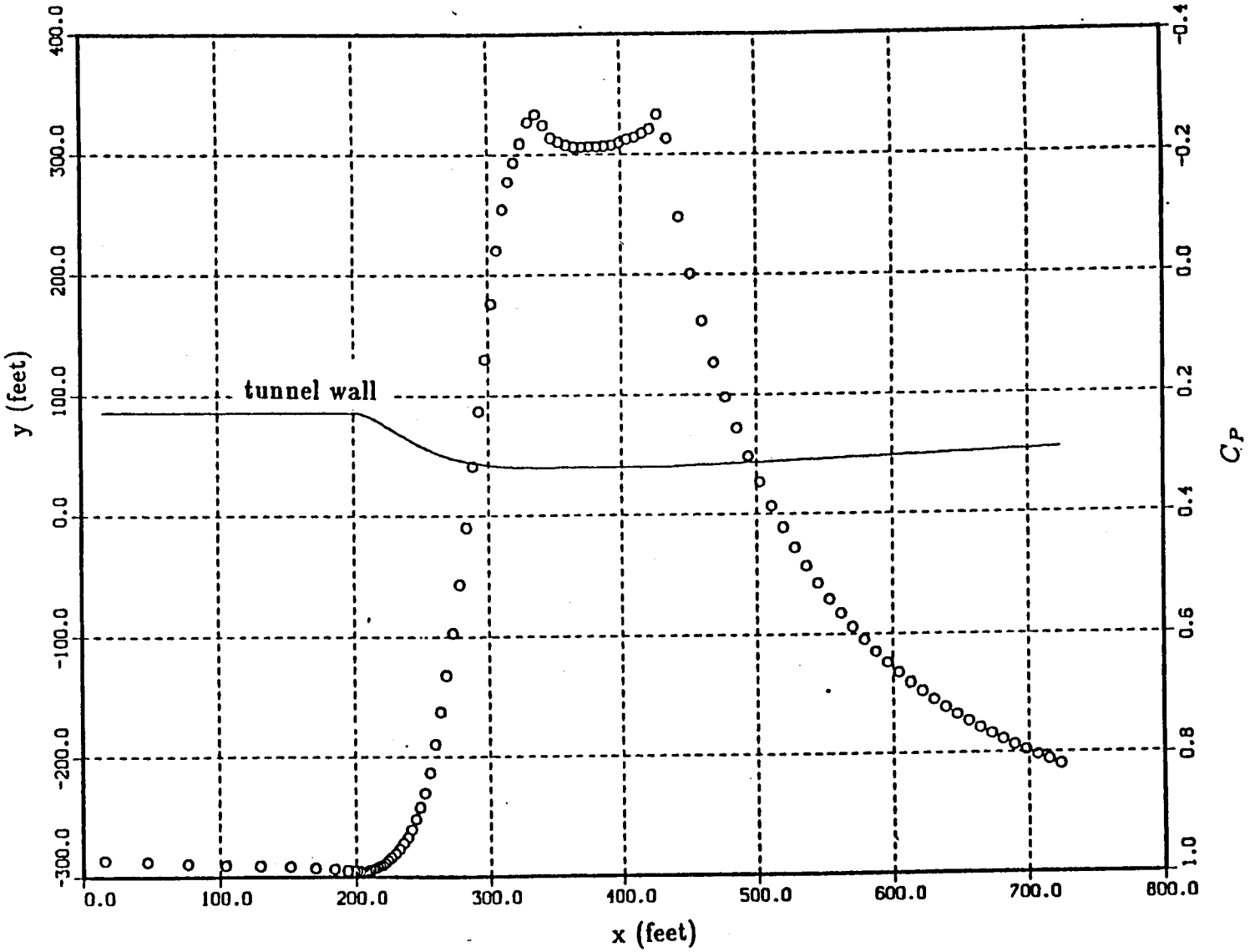

Figure 6 Wall Pressure Distribution in the VSAERO 40 x 80 Model at a $z = 0$ Cut with a Far-Field Factor of 5 and an Onset Velocity of 1.0

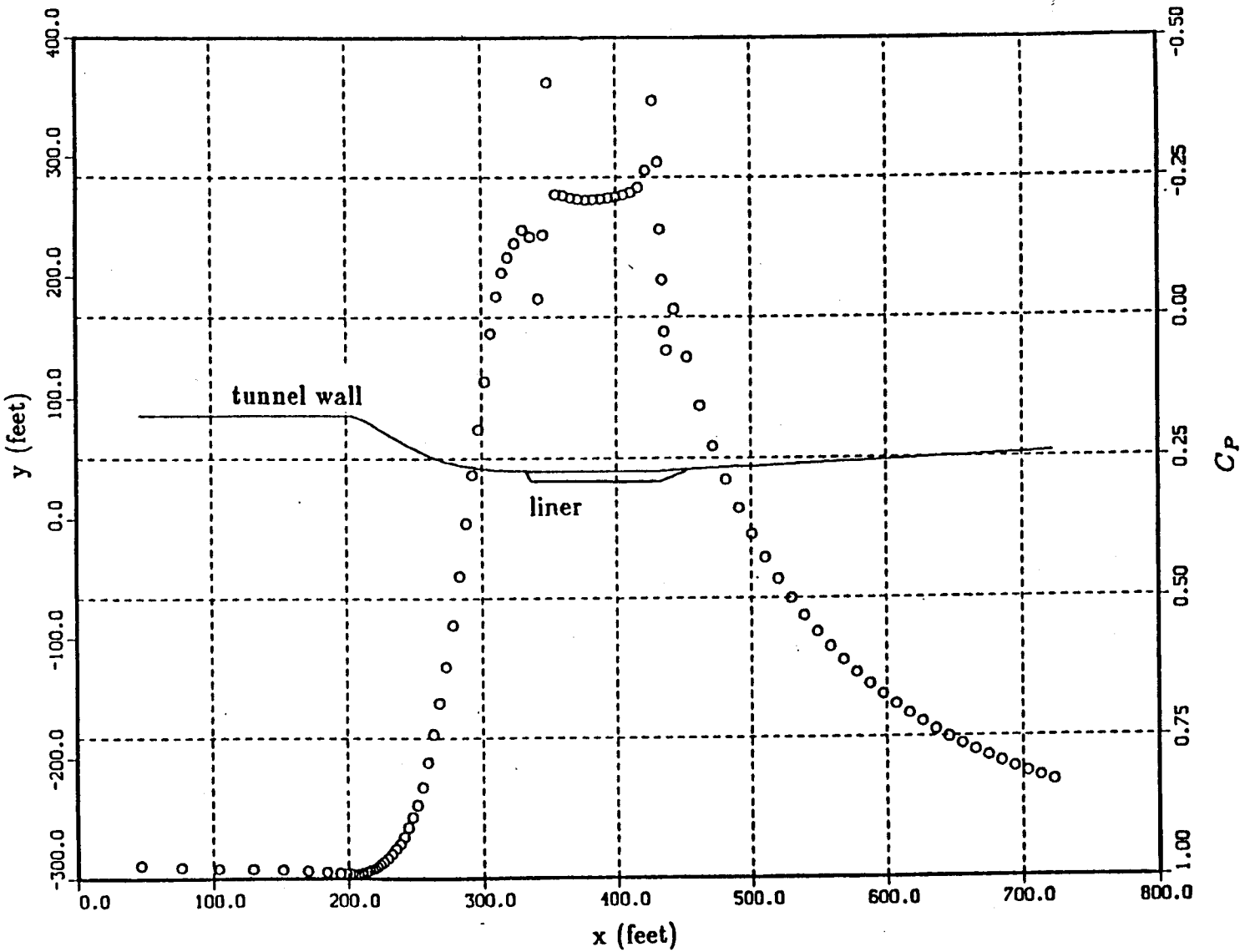

Figure 7 Wall Pressure Distribution in the VSAERO 40 x 80 Model with liner at a $z = 0$ Cut with a Far-Field Factor of 5 and an Onset Velocity of 1.0

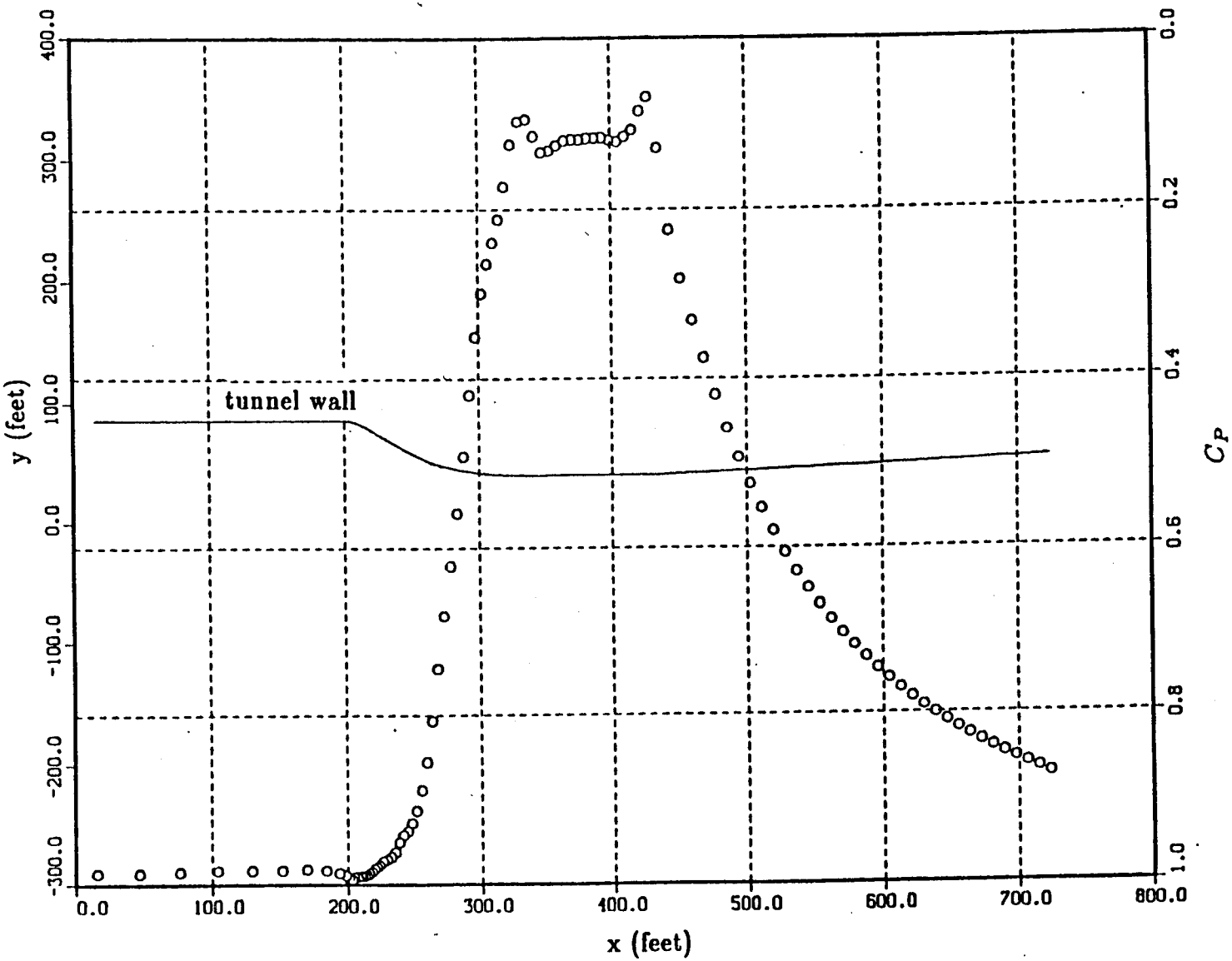

Figure 8 Wall Pressure Distribution in the VSAERO 40 × 80 Model at a $z = 0$ Cut with a Far-Field Factor of 5 and an Onset Velocity of 0.0

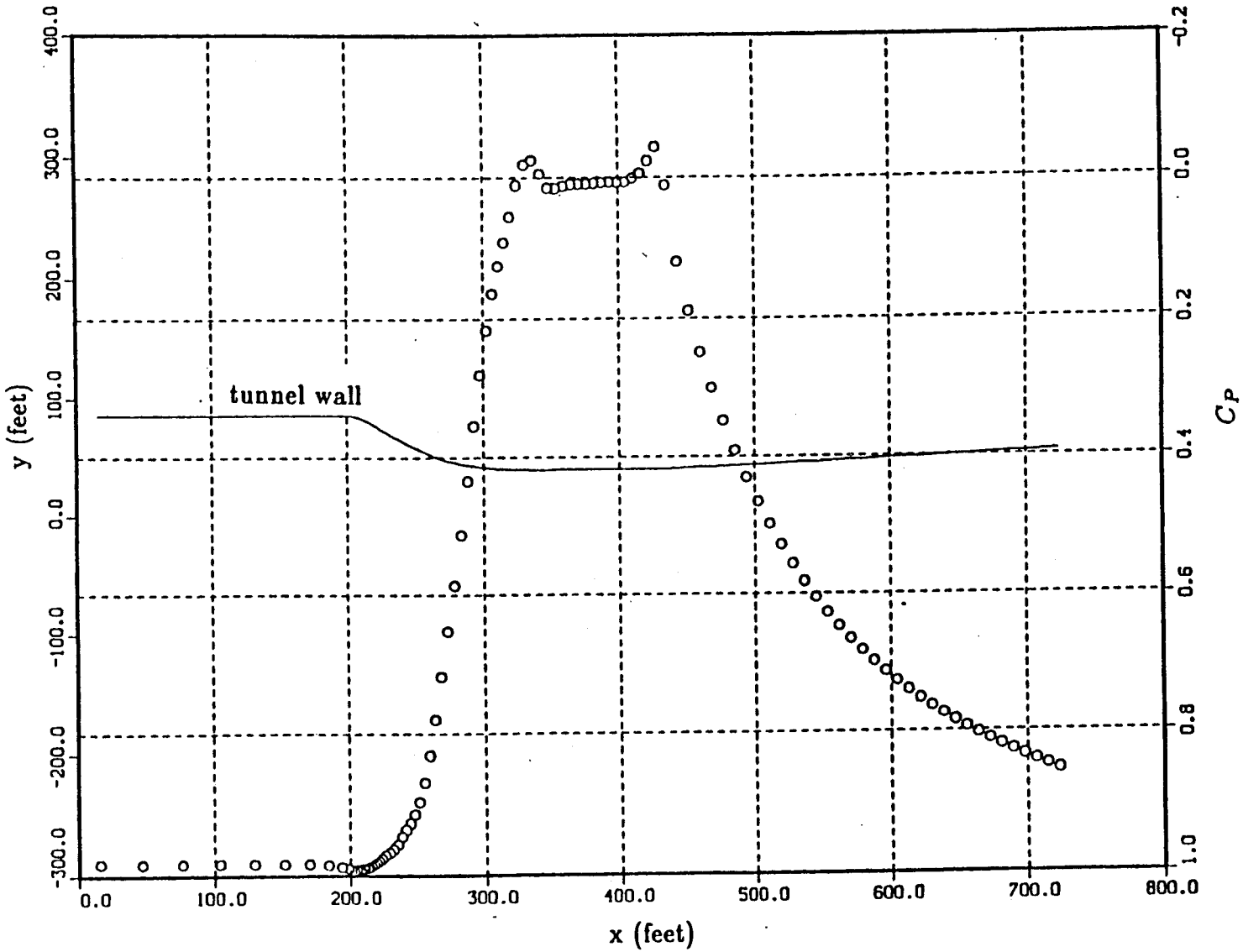

Figure 9 Wall Pressure Distribution in the VSAERO 40 × 80 Model at a $z = 0$ Cut with a Far-Field Factor of 5 and an Onset Velocity of 0.35

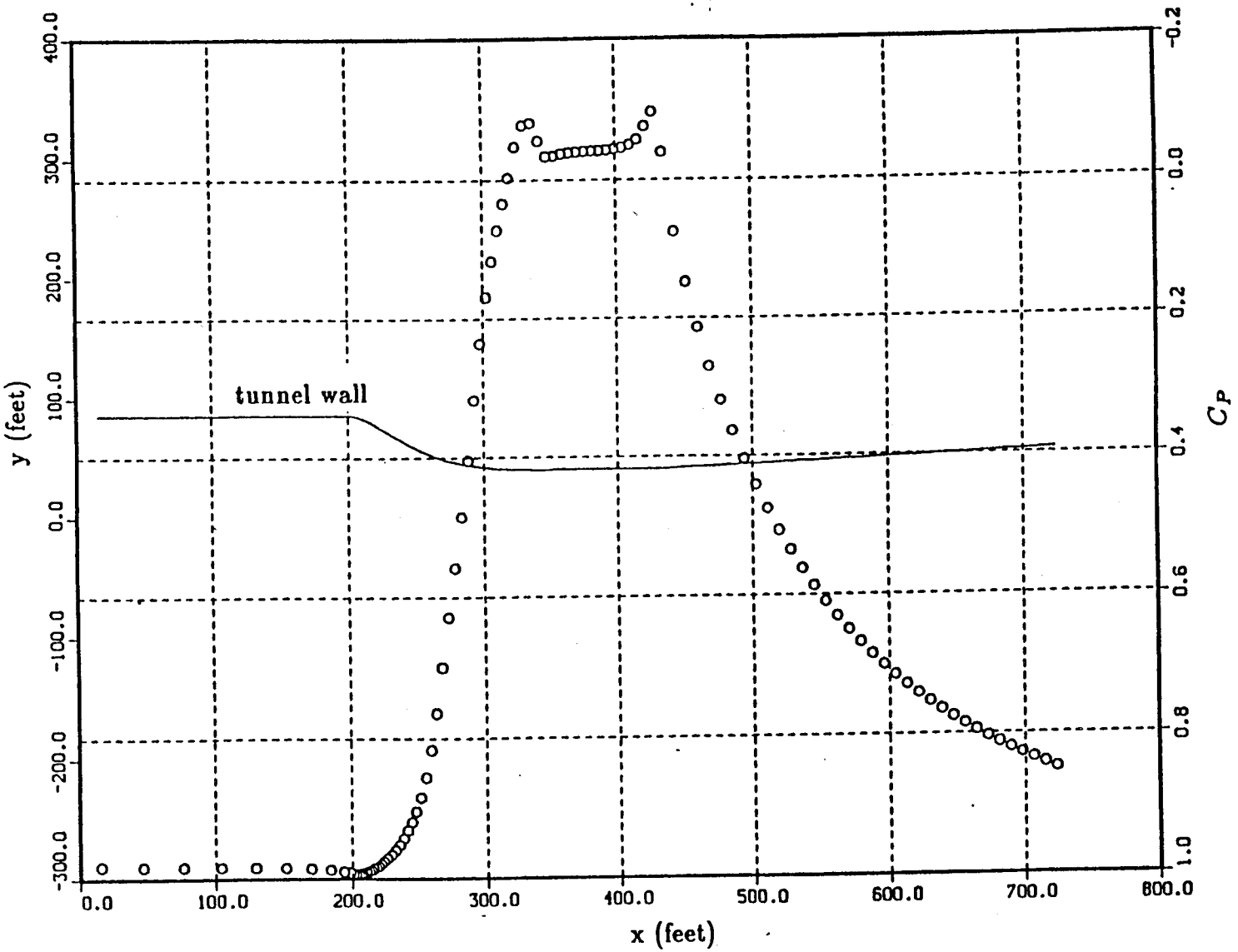

Figure 10 Wall Pressure Distribution in the VSAERO 40 × 80 Model at a $z = 0$ Cut with a Far-Field Factor of 10 and an Onset Velocity of 0.35

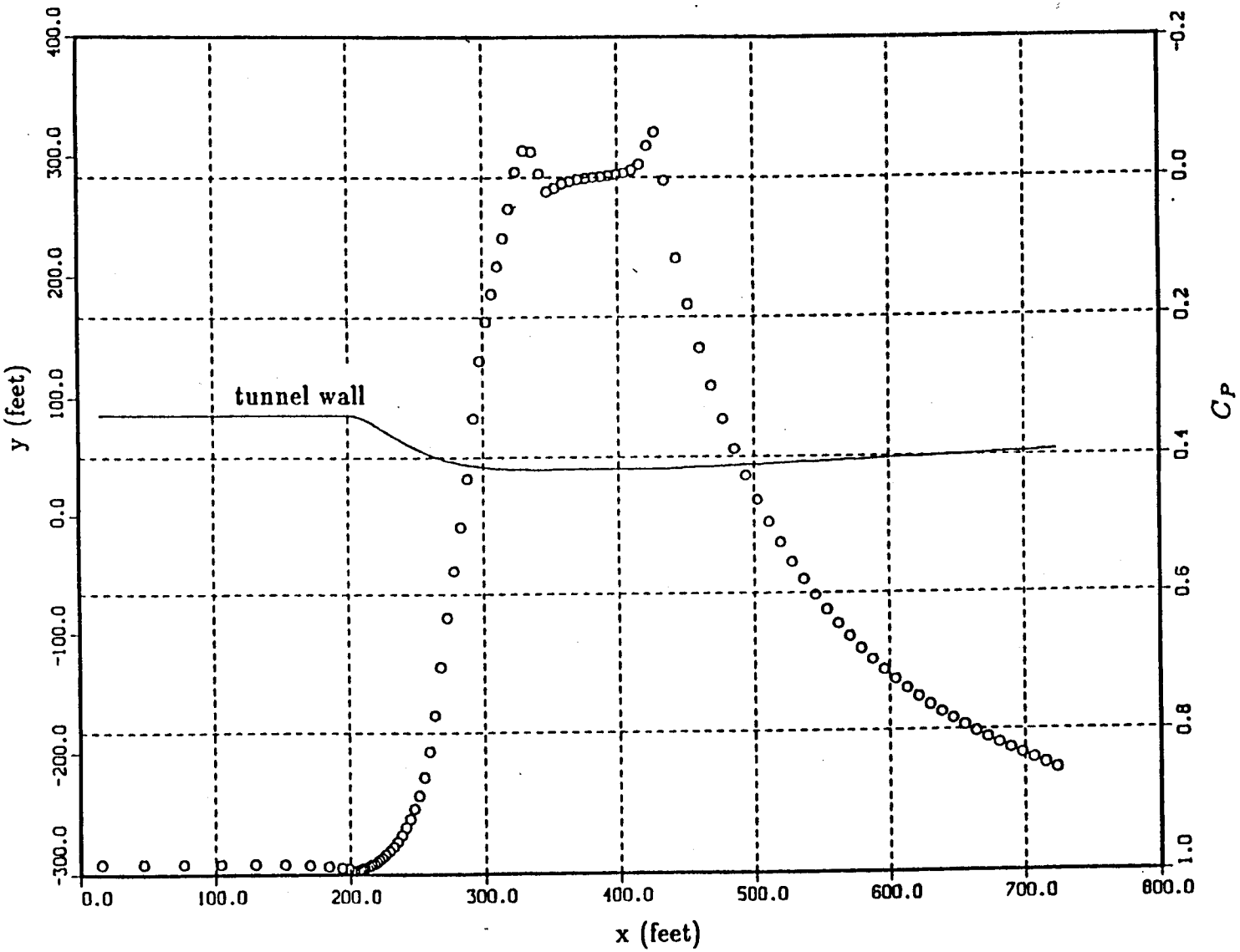

Figure 11 Wall Pressure Distribution in the VSAERO 40 × 80 Model at a $z = 0$ Cut with a Far-Field Factor of 10 and an Onset Velocity of 0.1

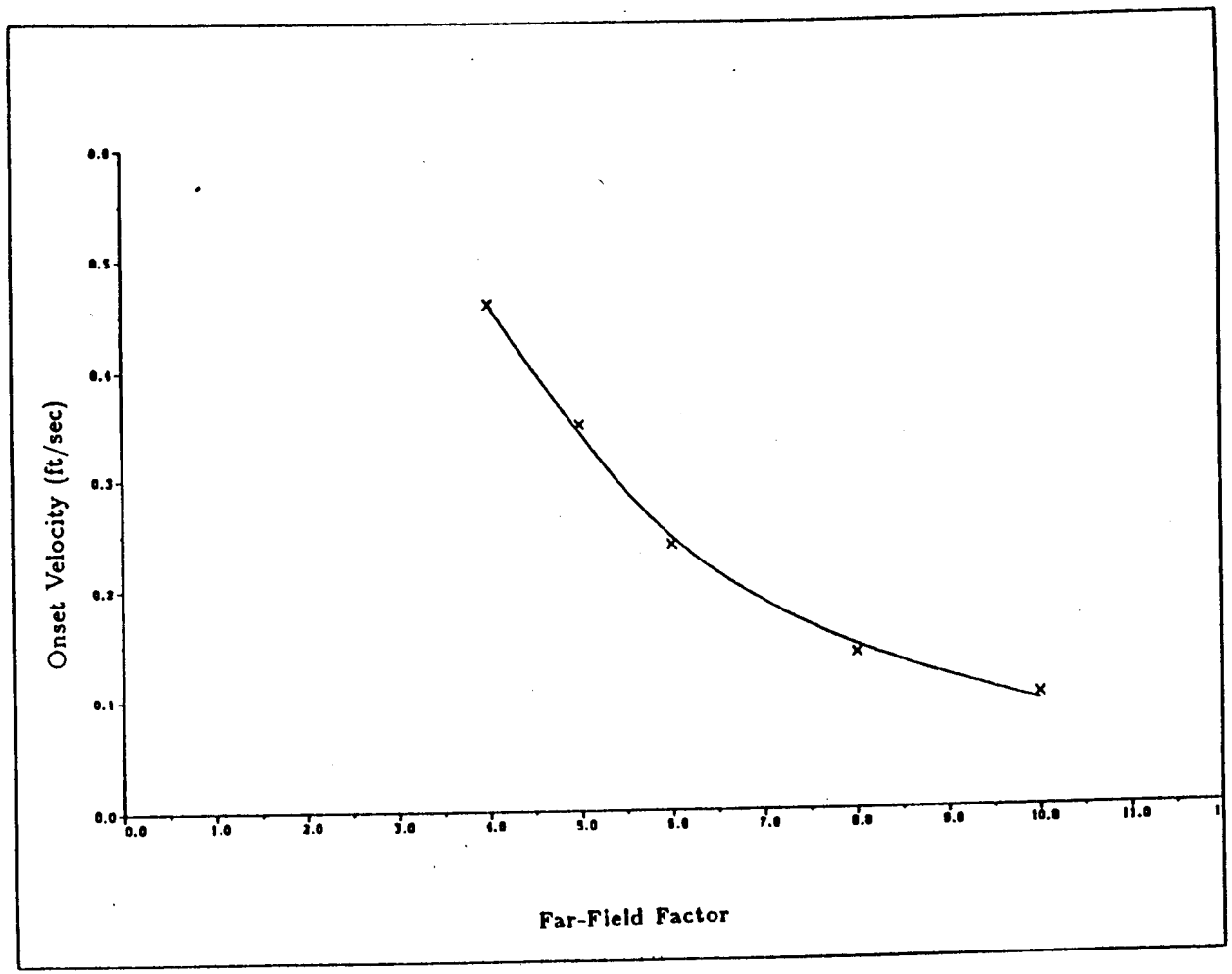

Figure 12 Plot of Onset Velocity Versus Far-Field Factor for Conservation of Mass in the 40 × 80 Model

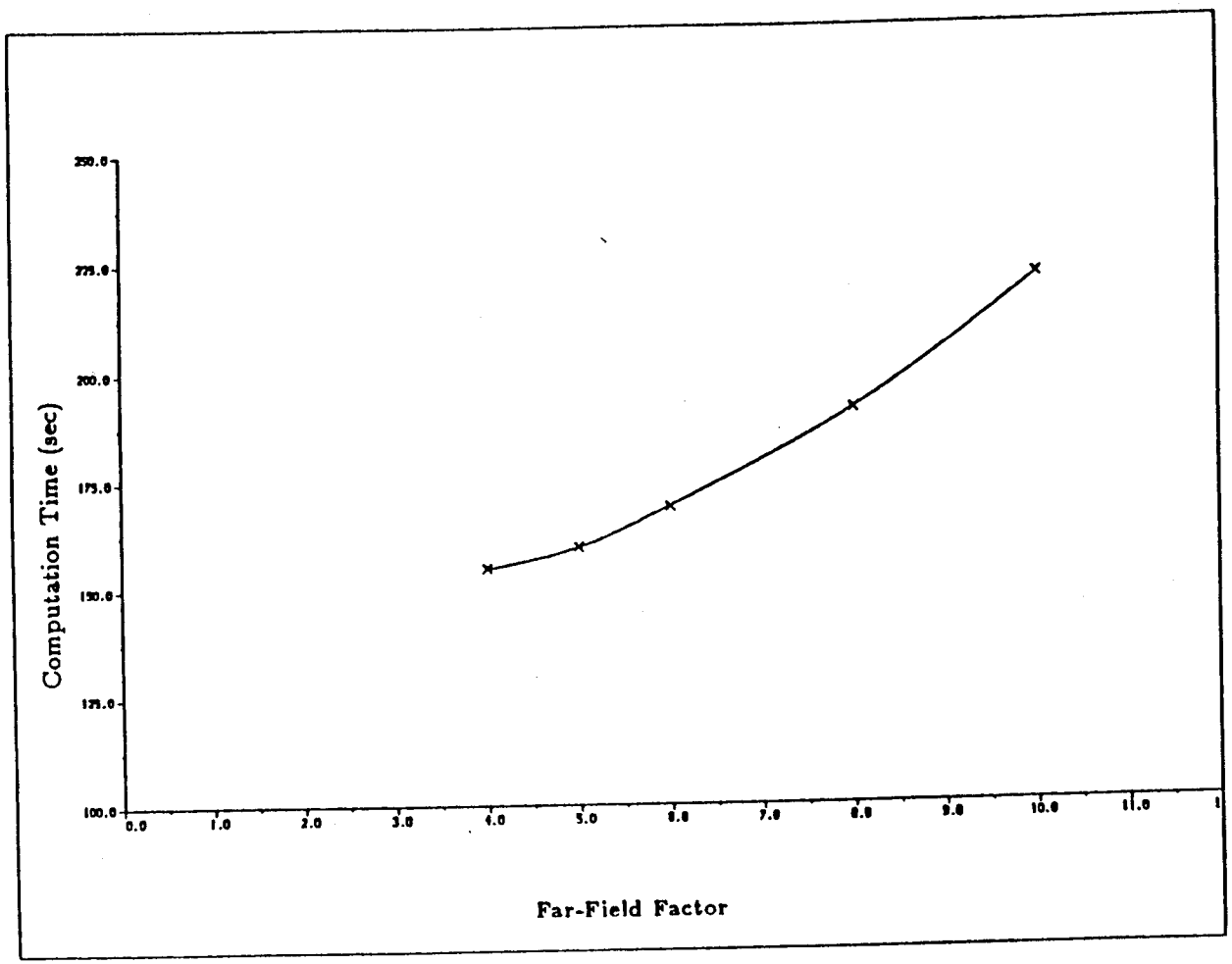

Figure 13 Plot of Computation Time on a Cray X-MP Computer Versus Far-Field Factor for the 40 × 80 Model

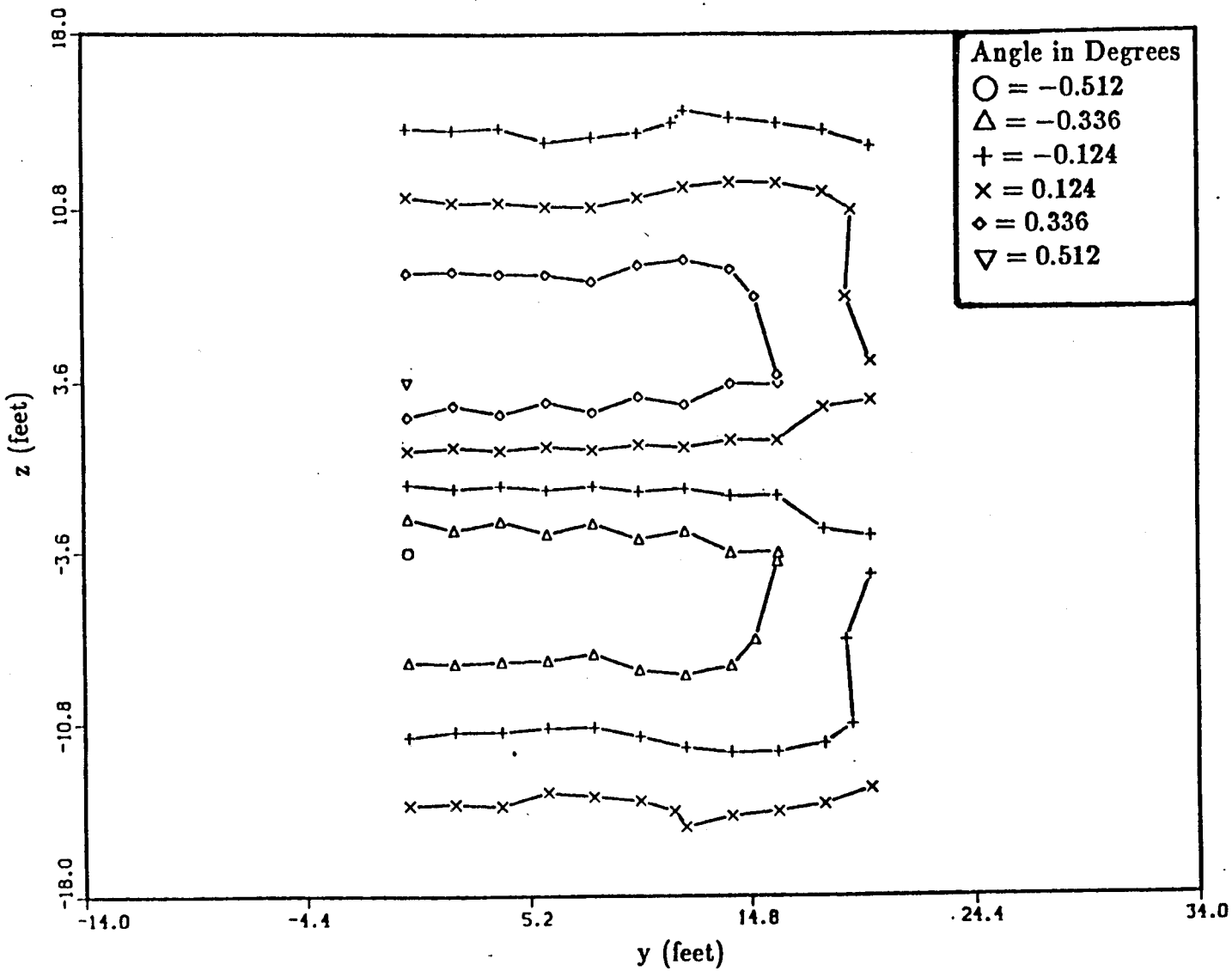

Figure 14 Alpha Contours on a Cross Section Plane Through the Center of the Test Section of the 40 × 80 with a Far-Field Factor of 5 and an Onset Velocity of 0.35

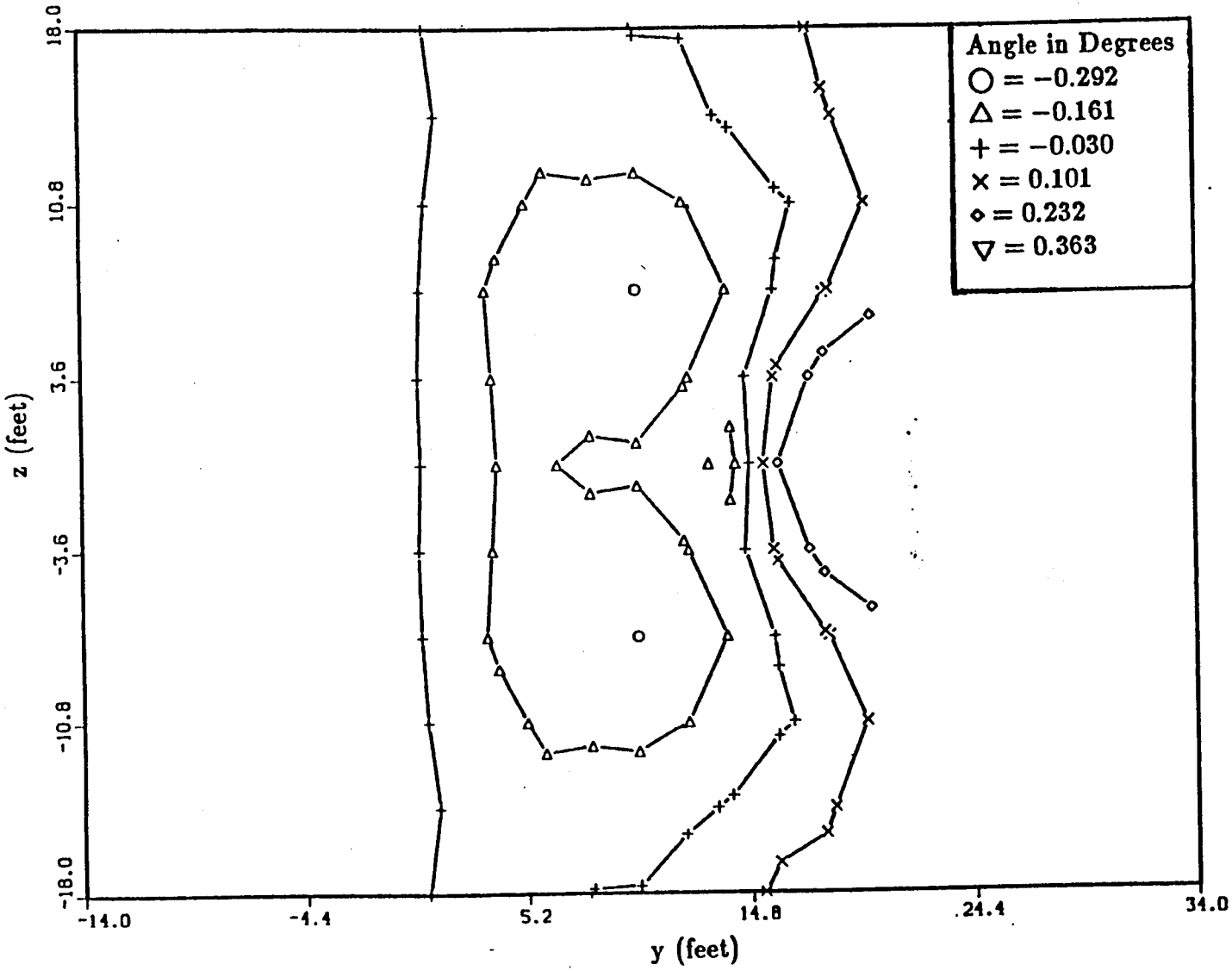

Figure 15 Beta Contours on a Cross Section Plane Through the Center of the Test Section of the 40 × 80 with a Far-Field Factor of 5 and an Onset Velocity of 0.35

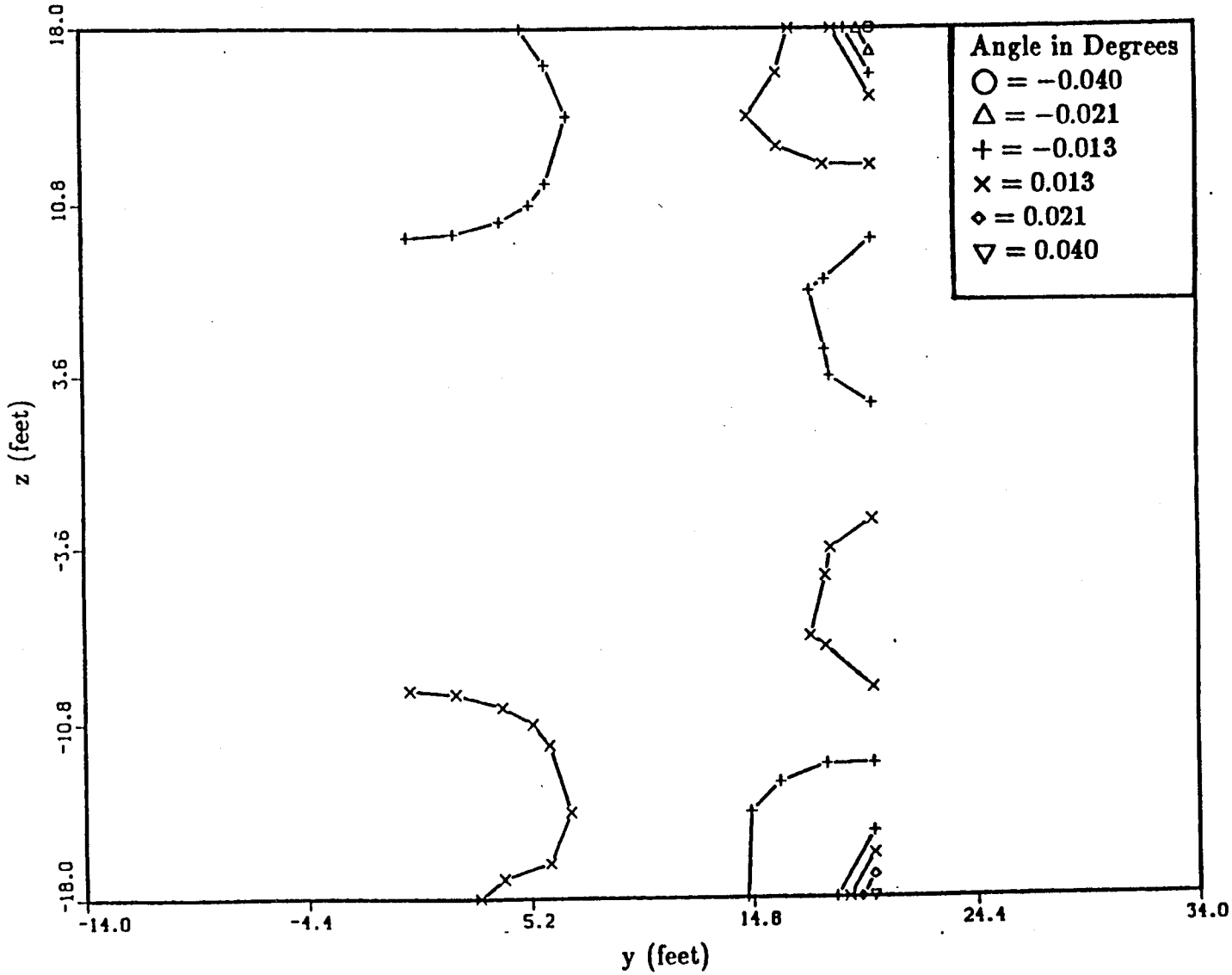

Figure 16 Alpha Contours on a Cross Section Plane Through the Center of the Test Section of the 40 × 80 with a Far-Field Factor of 10 and an Onset Velocity of 0.1

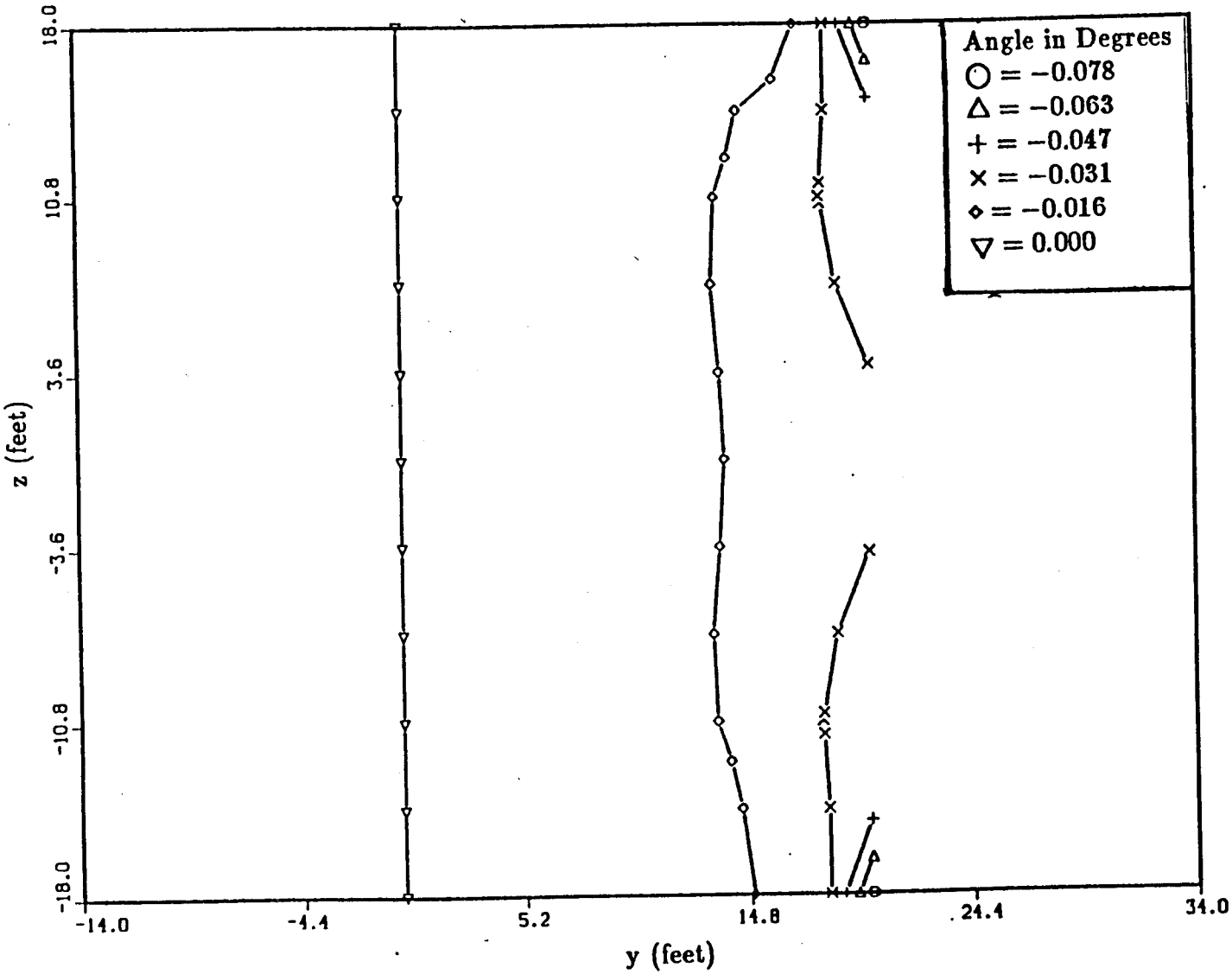

Figure 17 Beta Contours on a Cross Section Plane Through the Center of the Test Section of the 40 × 80 with a Far-Field Factor of 10 and an Onset Velocity of 0.1

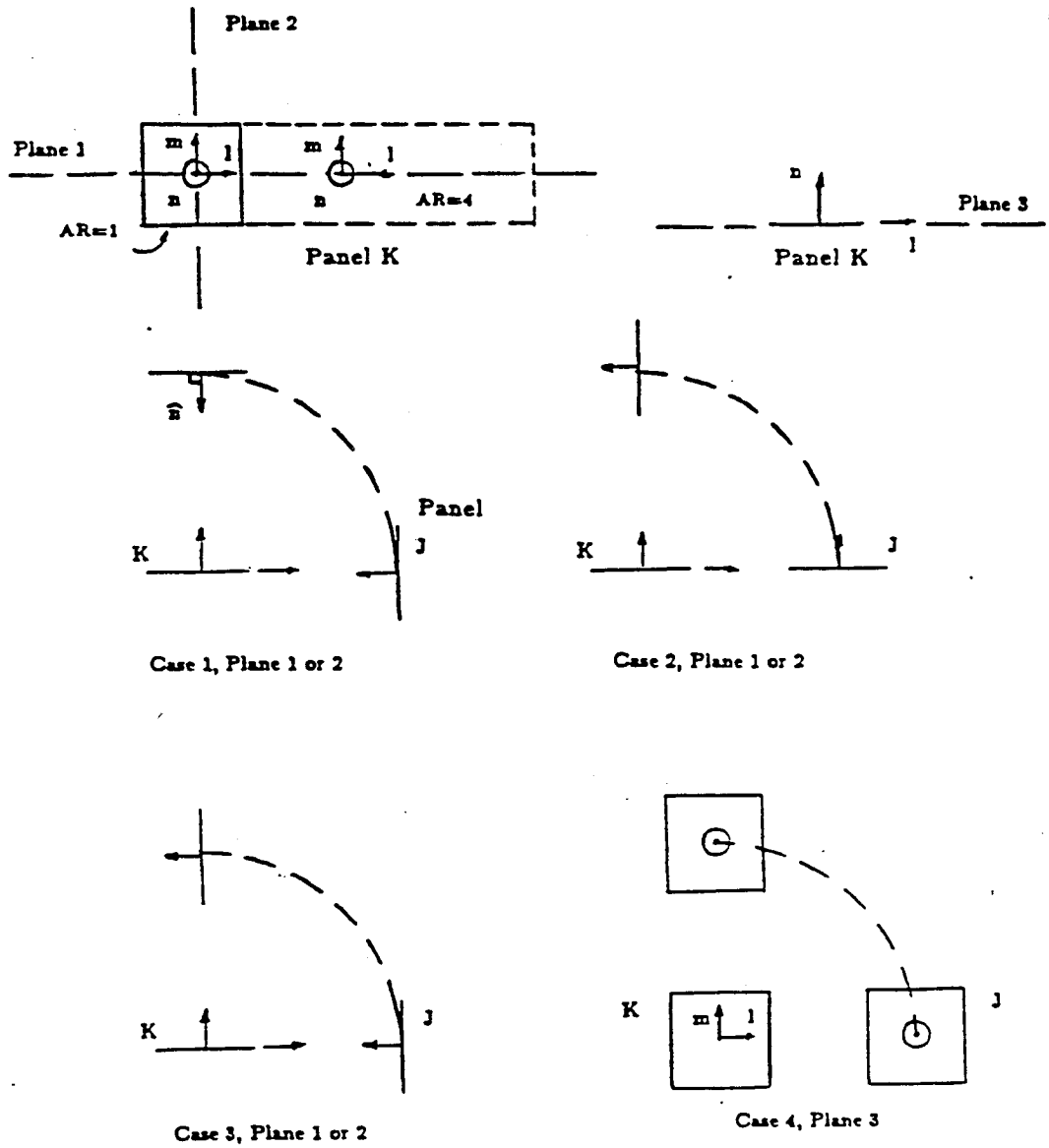

Figure 18 Panel Coordinate System and Panel Orientations for Cases 1-4

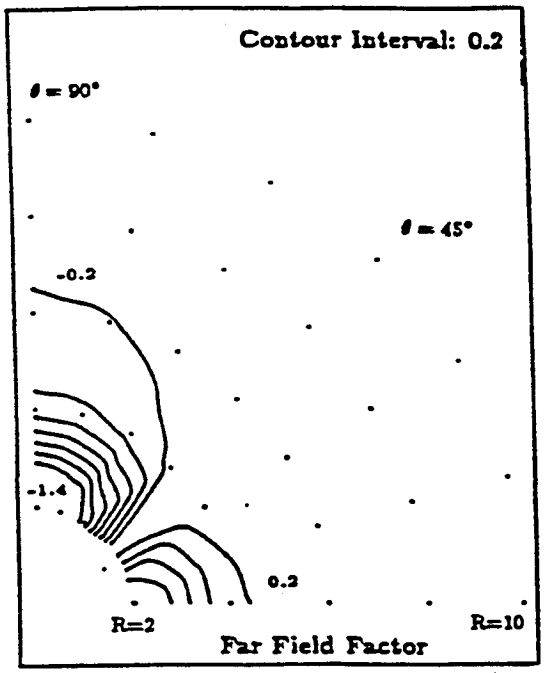

Figure 19a Percent Error in B_{JK}
Case 1, Plane 1, $AR = 1$

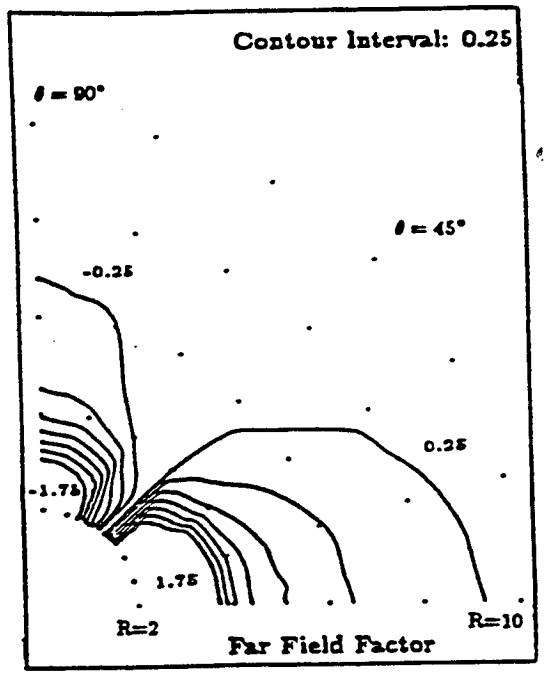

Figure 19b Percent Error in B_{JK}
Case 1, Plane 1, $AR = 4$

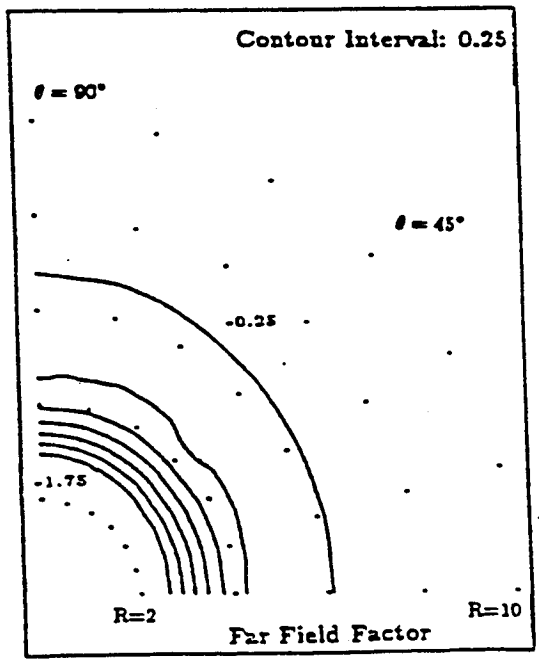

Figure 19c Percent Error in B_{JK}
Case 1, Plane 2, $AR = 4$

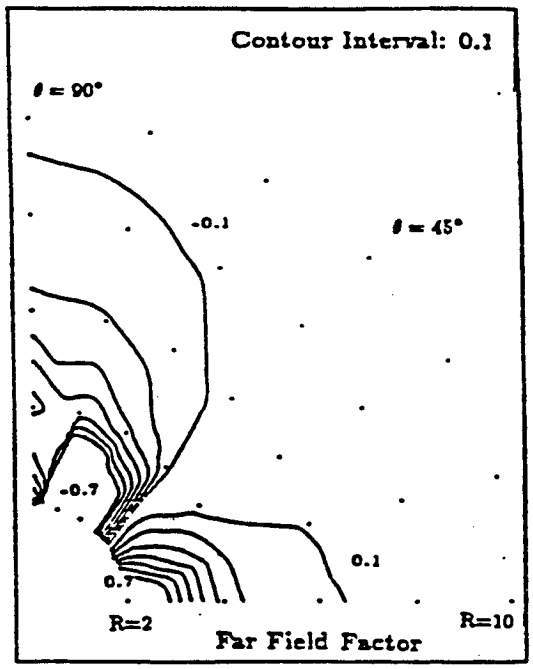

Figure 20a Percent Error in B_{JK}
Case 2, Plane 1, $AR = 1$

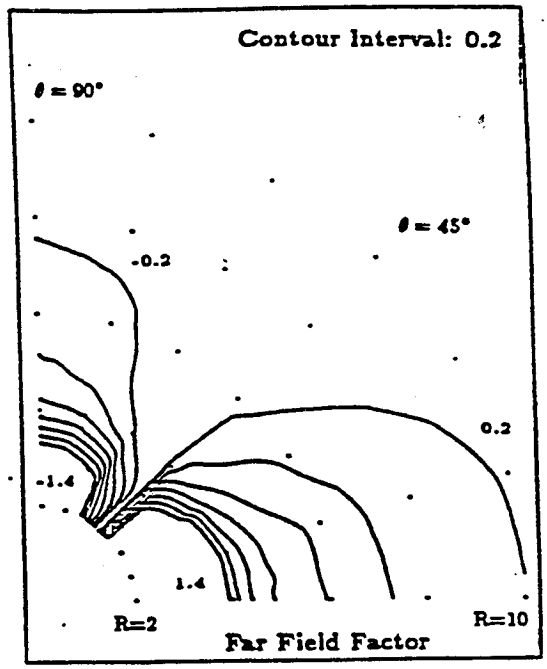

Figure 20b Percent Error in B_{JK}
Case 2, Plane 1, $AR = 4$

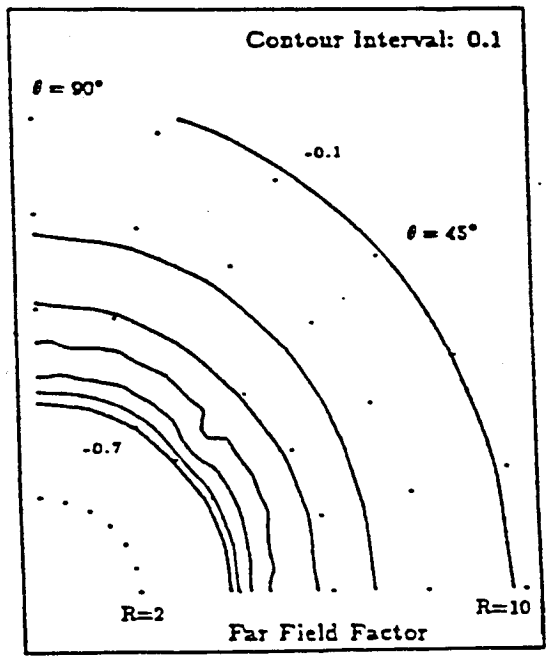

Figure 20c Percent Error in B_{JK}
Case 2, Plane 2, $AR = 4$

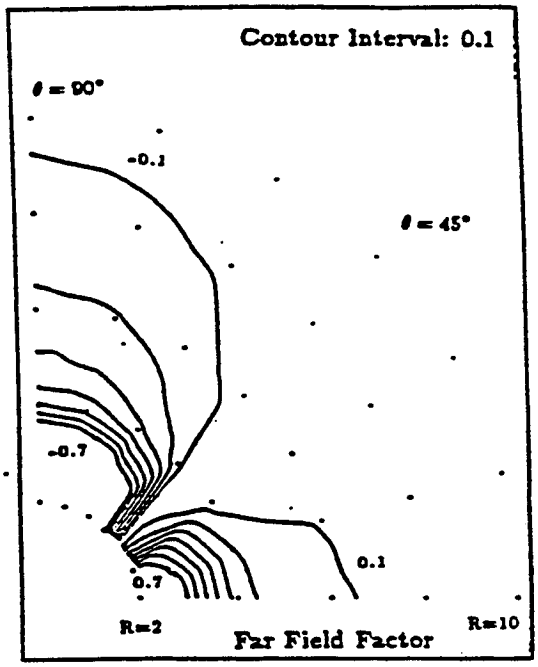

Figure 21a Percent Error in B_{JK}
Case 3, Plane 1, $AR = 1$

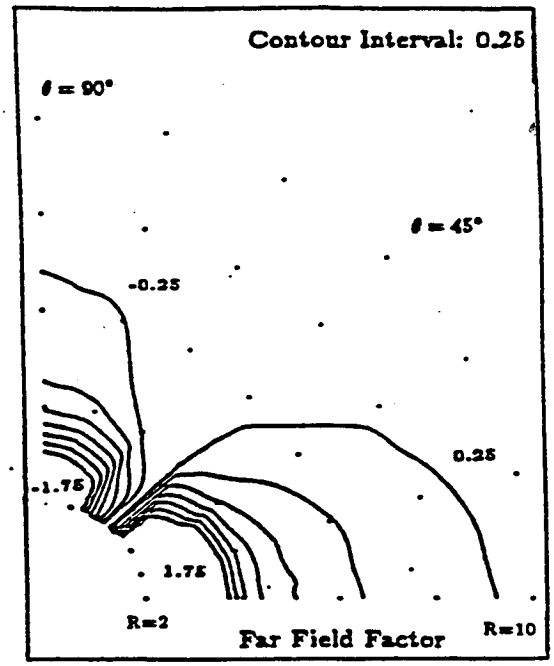

Figure 21b Percent Error in B_{JK}
Case 3, Plane 1, $AR = 4$

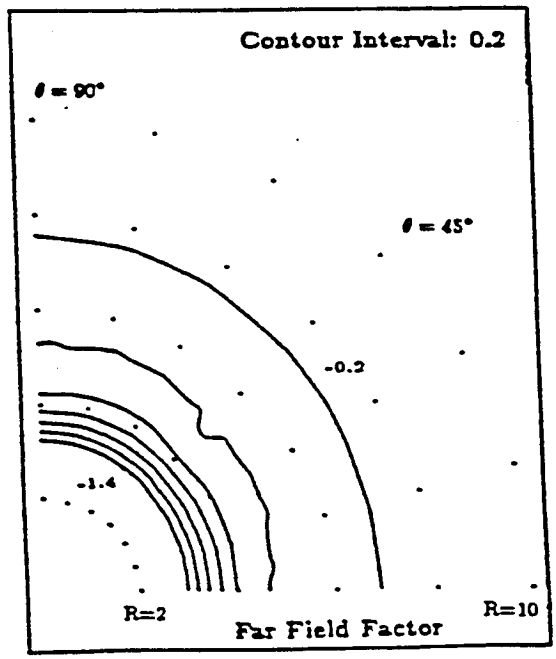

Figure 21c Percent Error in B_{JK}
Case 3, Plane 2, $AR = 4$

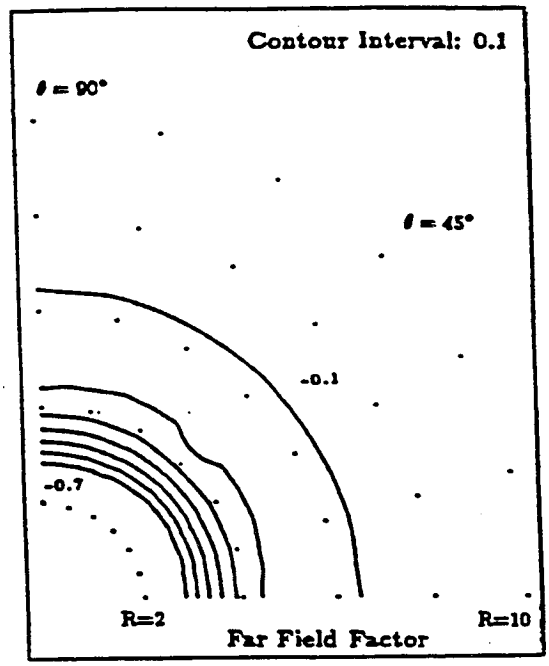

Figure 22a Percent Error in B_{JK}
Case 4, Plane 3, $AR = 1$

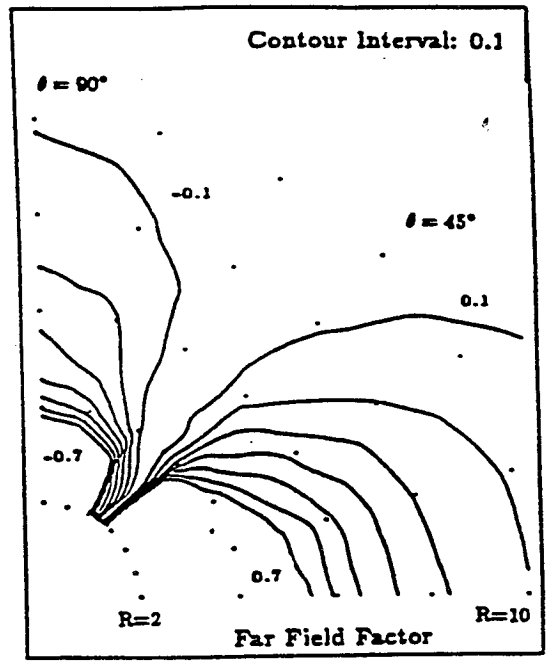

Figure 22b Percent Error in B_{JK}
Case 4, Plane 3, $AR = 4$

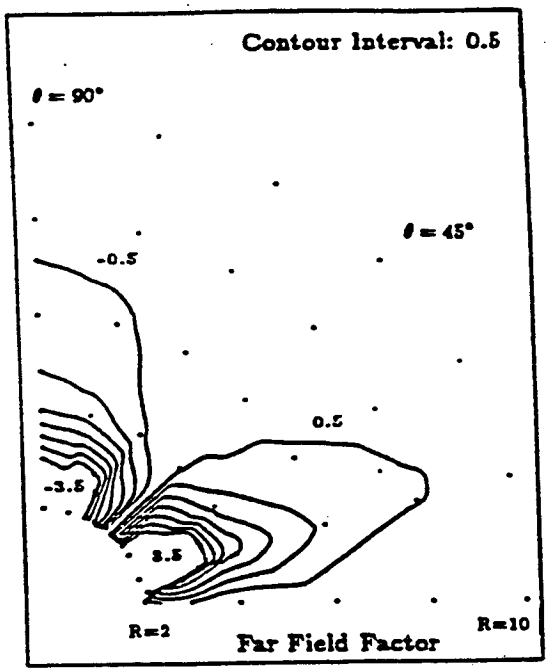

Figure 23a Percent Error in C_{JK}
Case 1, Plane 1, $AR = 1$

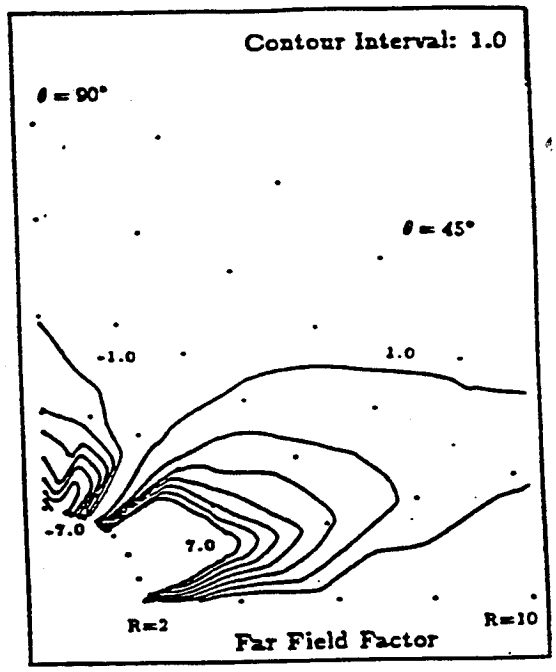

Figure 23b Percent Error in C_{JK}
Case 1, Plane 1, $AR = 4$

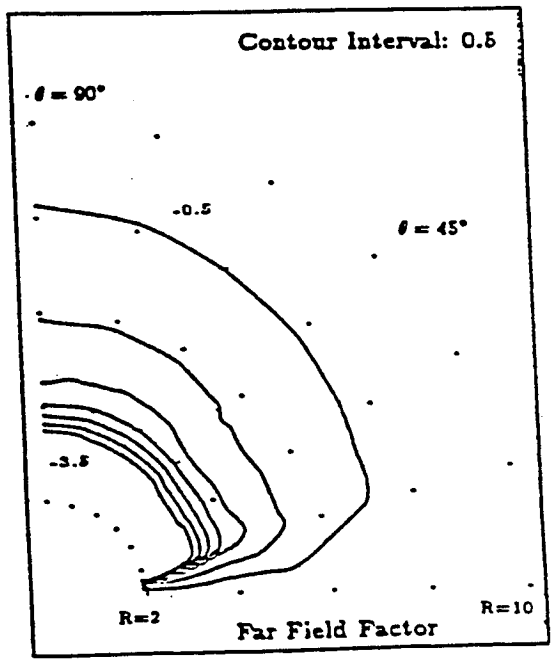

Figure 23c Percent Error in C_{JK}
Case 1, Plane 2, $AR = 4$

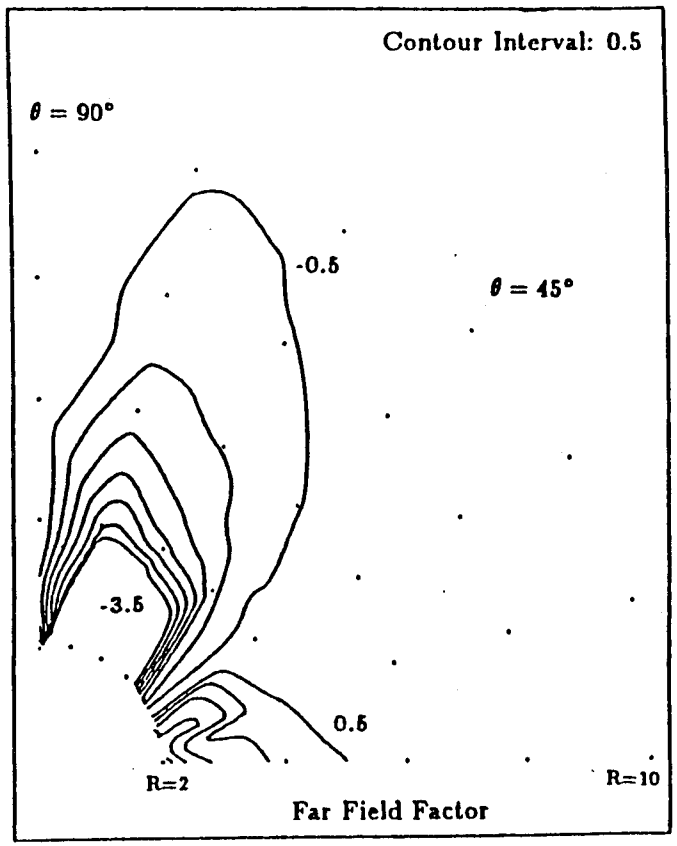

Figure 24a Percent Error in $\vec{V}_{\sigma r K}$
L Component, Plane 1, $AR = 1$

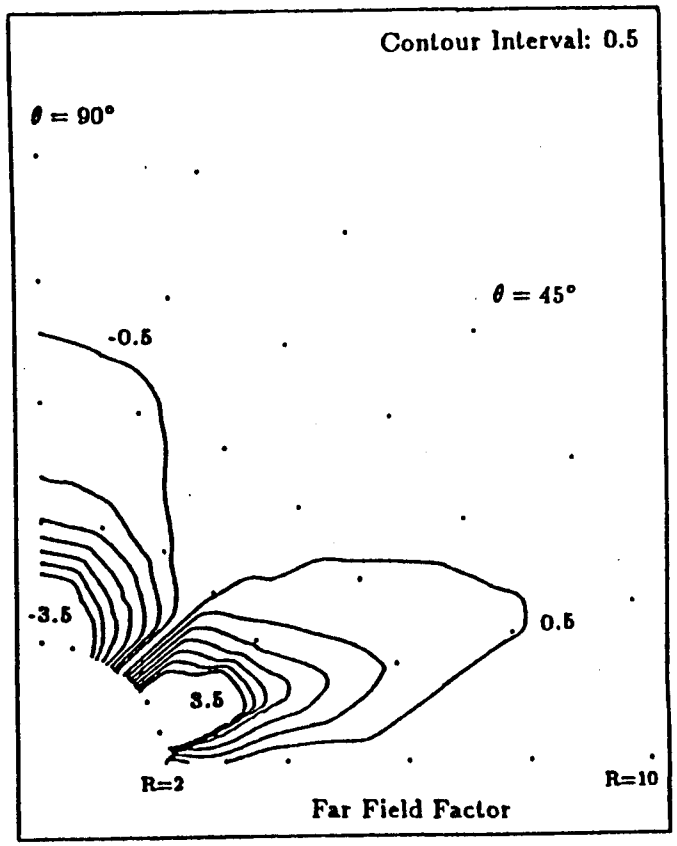

Figure 24b Percent Error in $\vec{V}_{\sigma r K}$
N Component, Plane 1, $AR = 1$

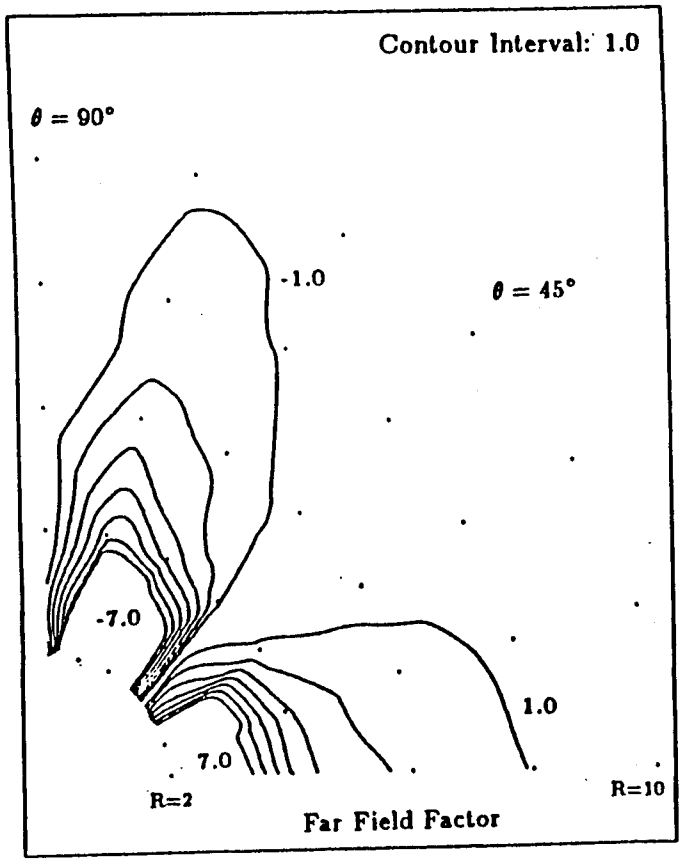

Figure 25a Percent Error in $\vec{V}_{\sigma rK}$
L Component, Plane 1, $AR = 4$

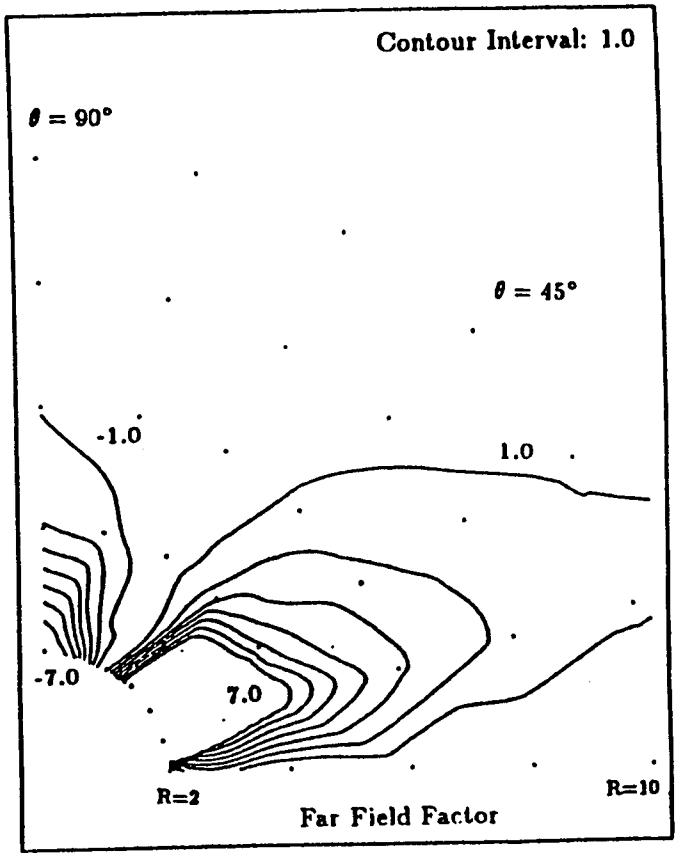

Figure 25b Percent Error in $\vec{V}_{\sigma rK}$
N Component, Plane 1, $AR = 4$

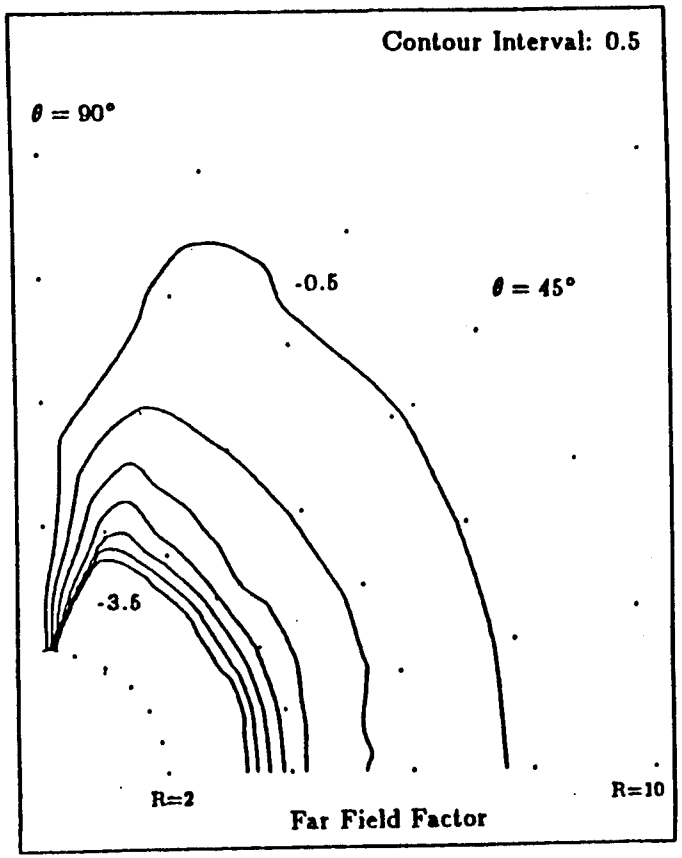

Figure 26a Percent Error in $\vec{V}_{\sigma PK}$
M Component, Plane 2, $AR = 4$

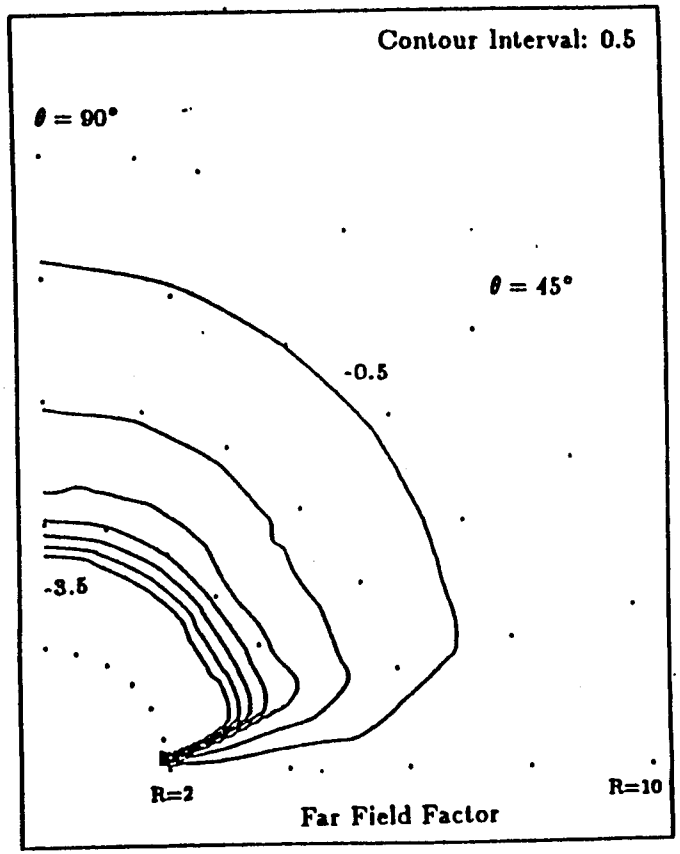

Figure 26b Percent Error in $\vec{V}_{\sigma PK}$
N Component, Plane 2, $AR = 4$

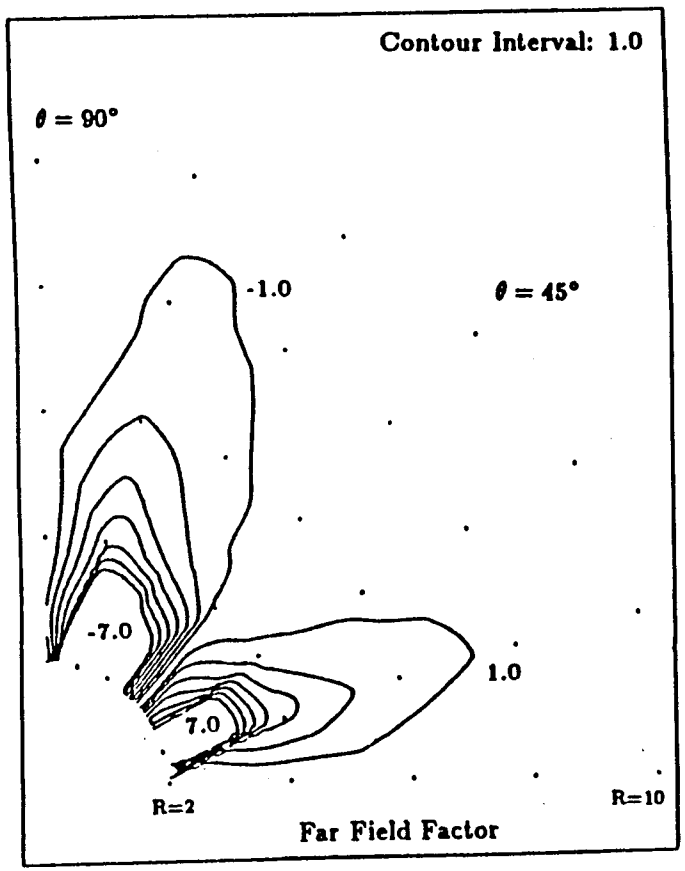

Figure 27a Percent Error in $\vec{V}_{\mu r \kappa}$
L Component, Plane 1, $AR = 1$

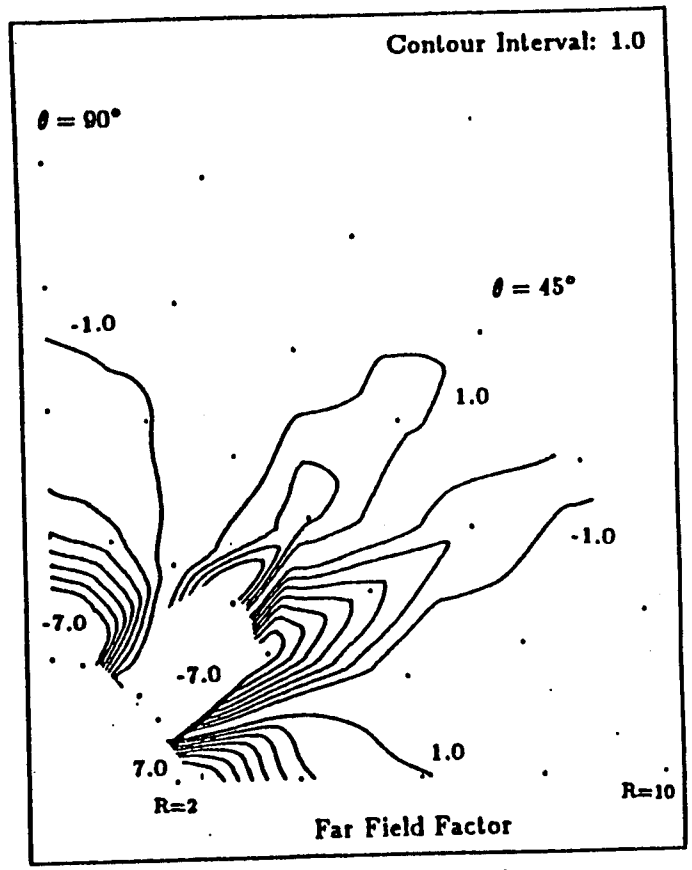

Figure 27b Percent Error in $\vec{V}_{\mu r \kappa}$
N Component, Plane 1, $AR = 1$

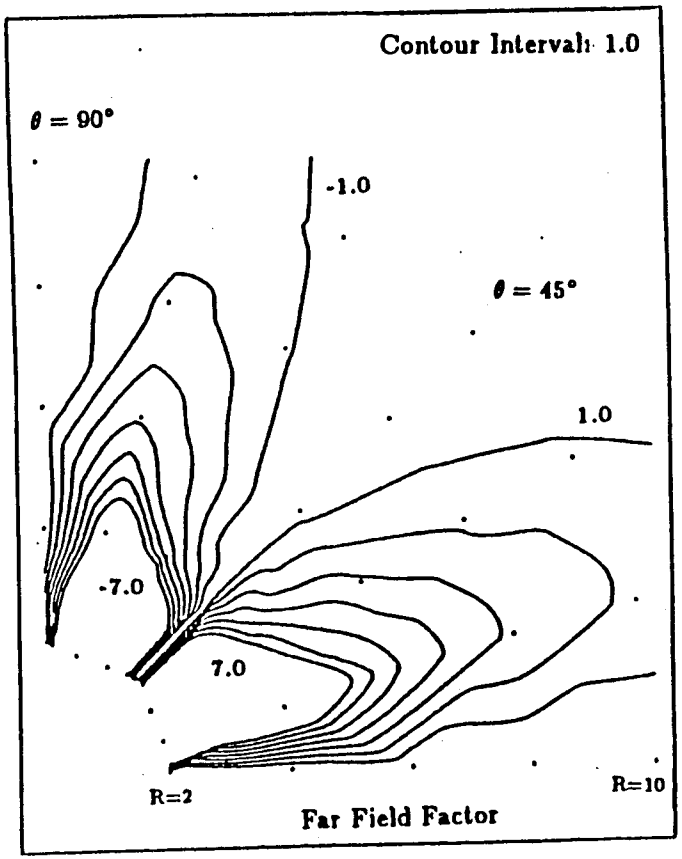

Figure 28a Percent Error in $\vec{V}_{\mu r \kappa}$
L Component, Plane 1, $AR = 4$

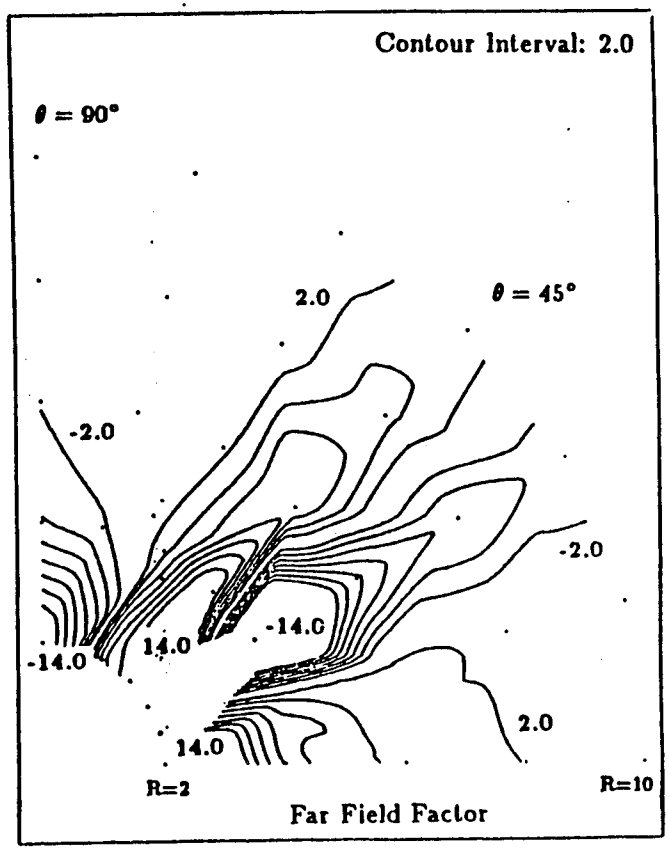

Figure 28b Percent Error in $\vec{V}_{\mu r \kappa}$
N Component, Plane 1, $AR = 4$

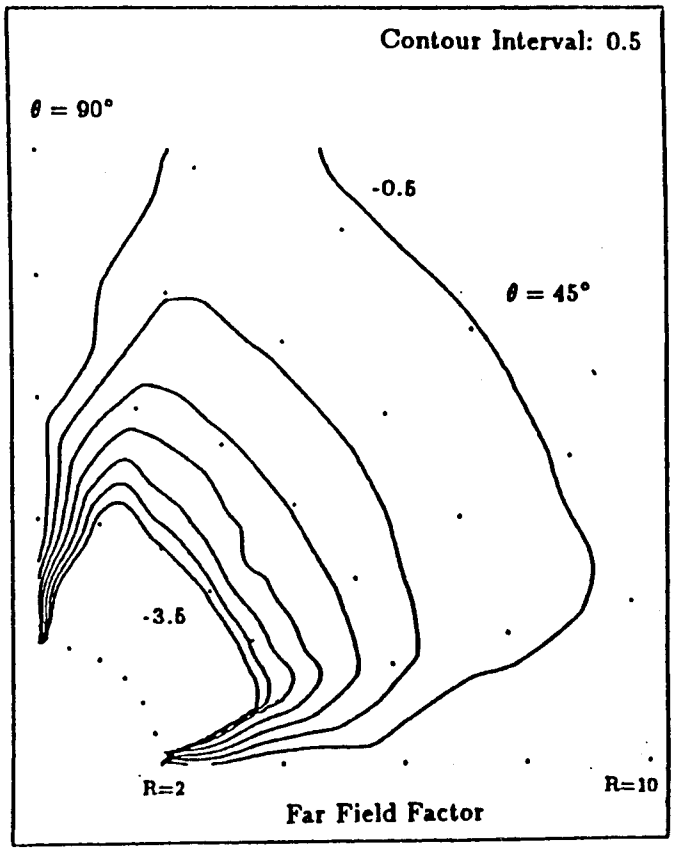

Figure 29a Percent Error in $\vec{V}_{\mu r K}$
M Component, Plane 2, $AR = 4$

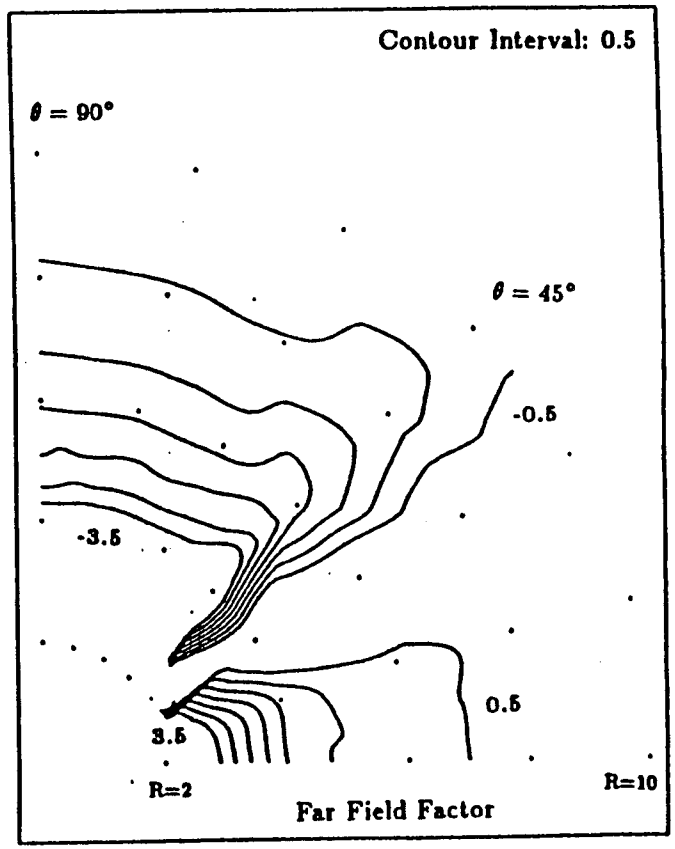

Figure 29b Percent Error in $\vec{V}_{\mu r K}$
N Component, Plane 2, $AR = 4$

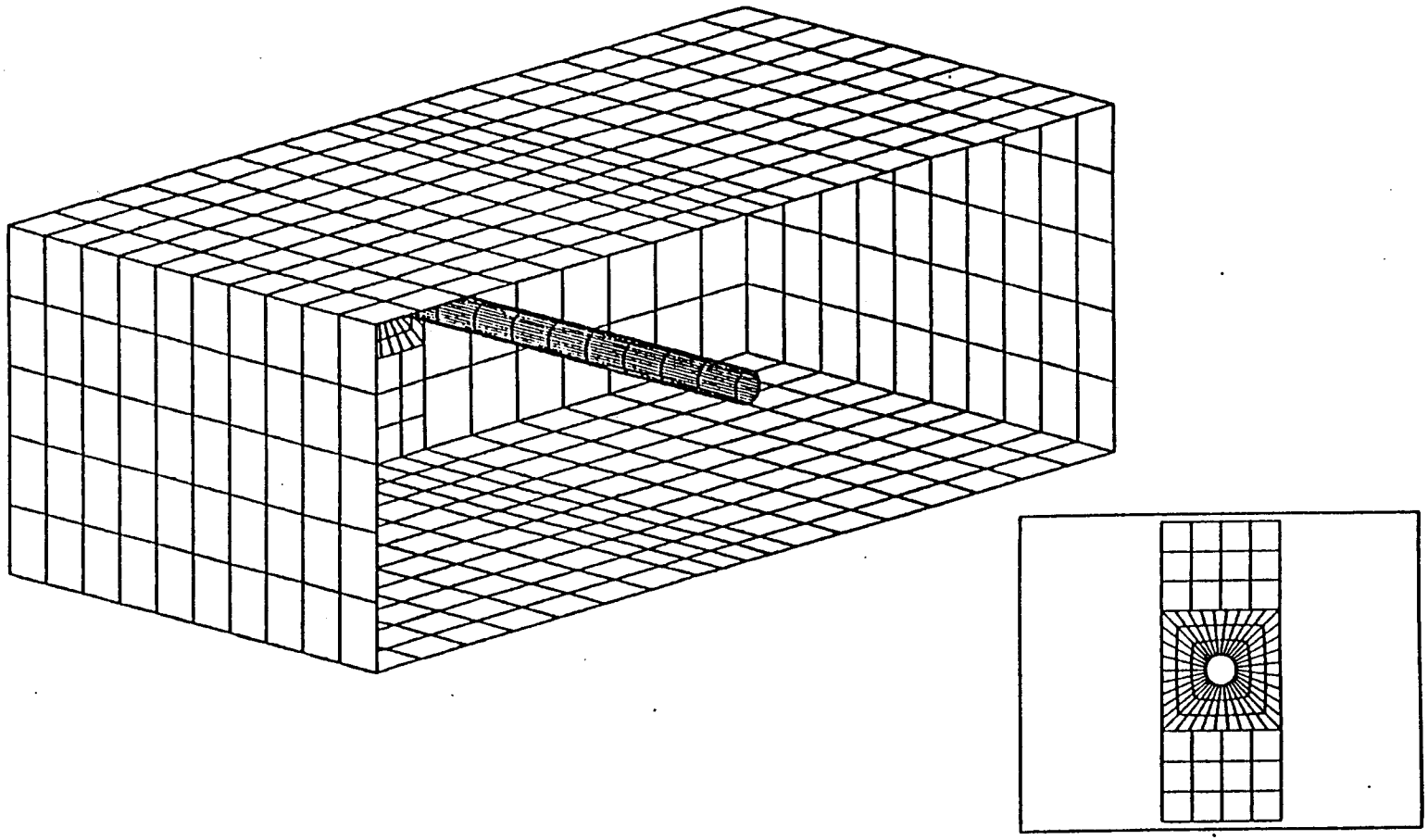

Figure 30 Paneled Geometry of Cylinder in Duct with Inset Showing Details of Cylinder/Wall Junction

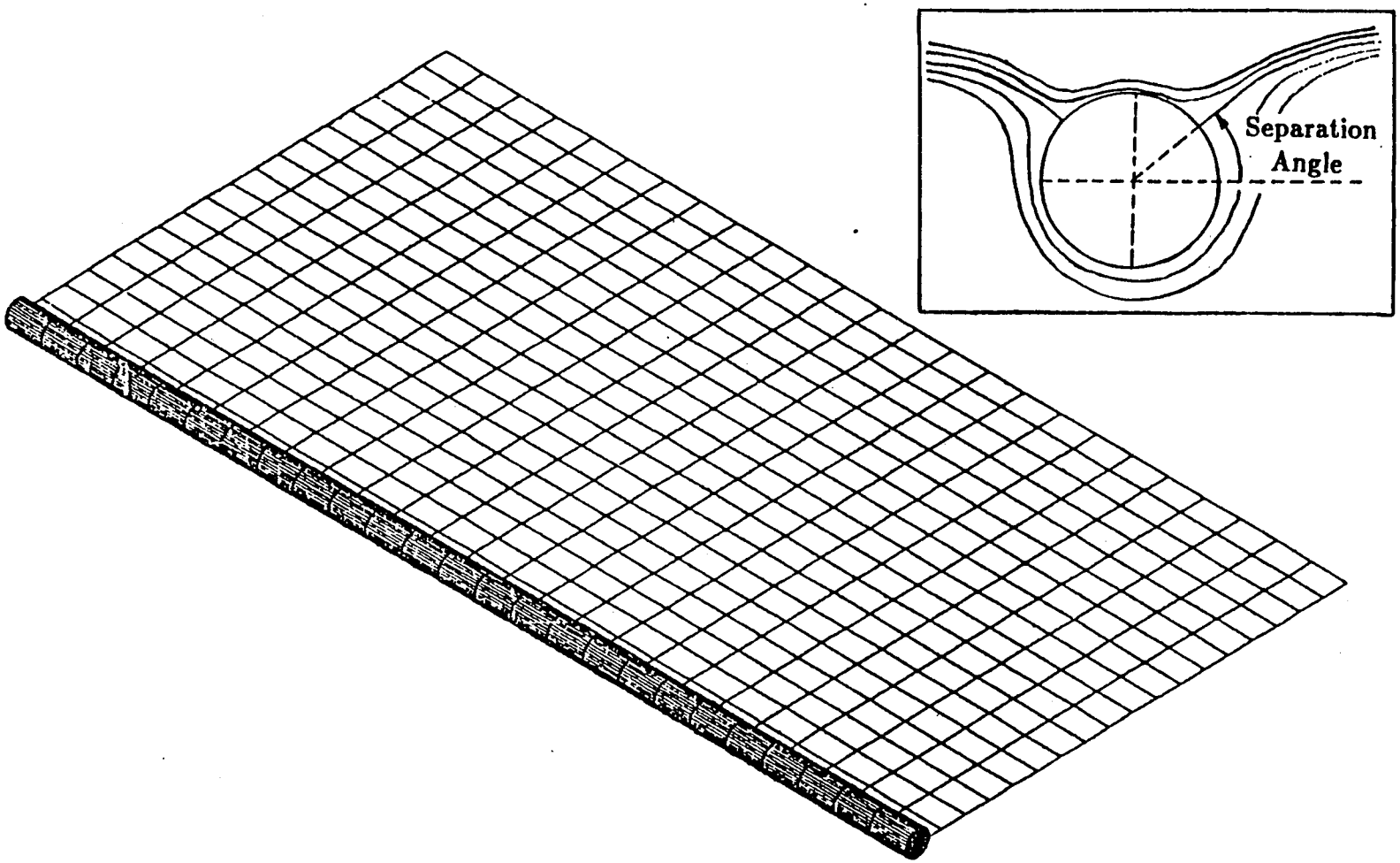

Figure 31 Model Used to Approximate a Two-Dimensional Cylinder with Inset Showing Wake Separation Angle

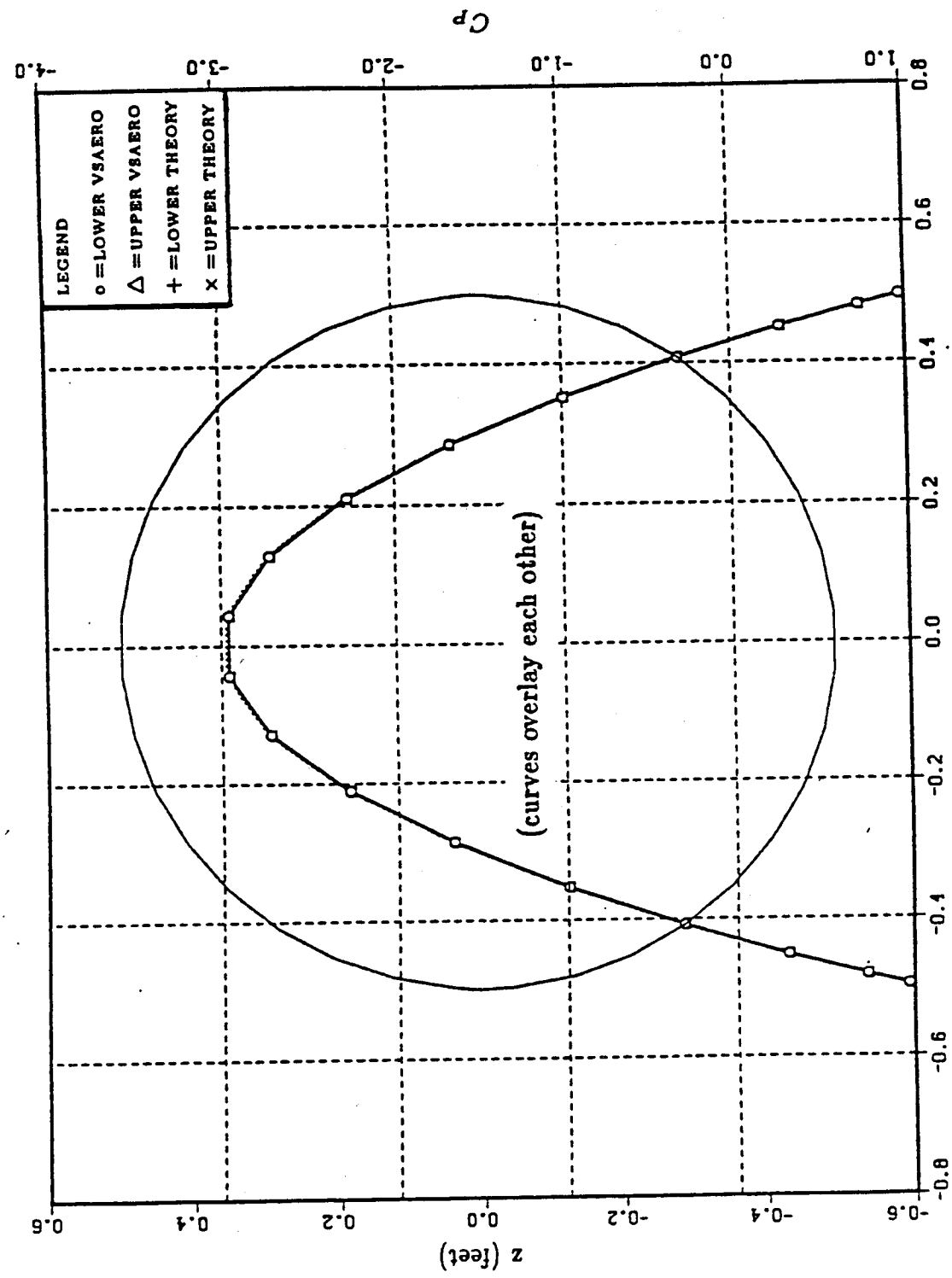

Figure 32 Comparison of the VSAERO and Theoretical Pressure Distributions on a Two-Dimensional Cylinder Outside the Tunnel, Carrying no Lift

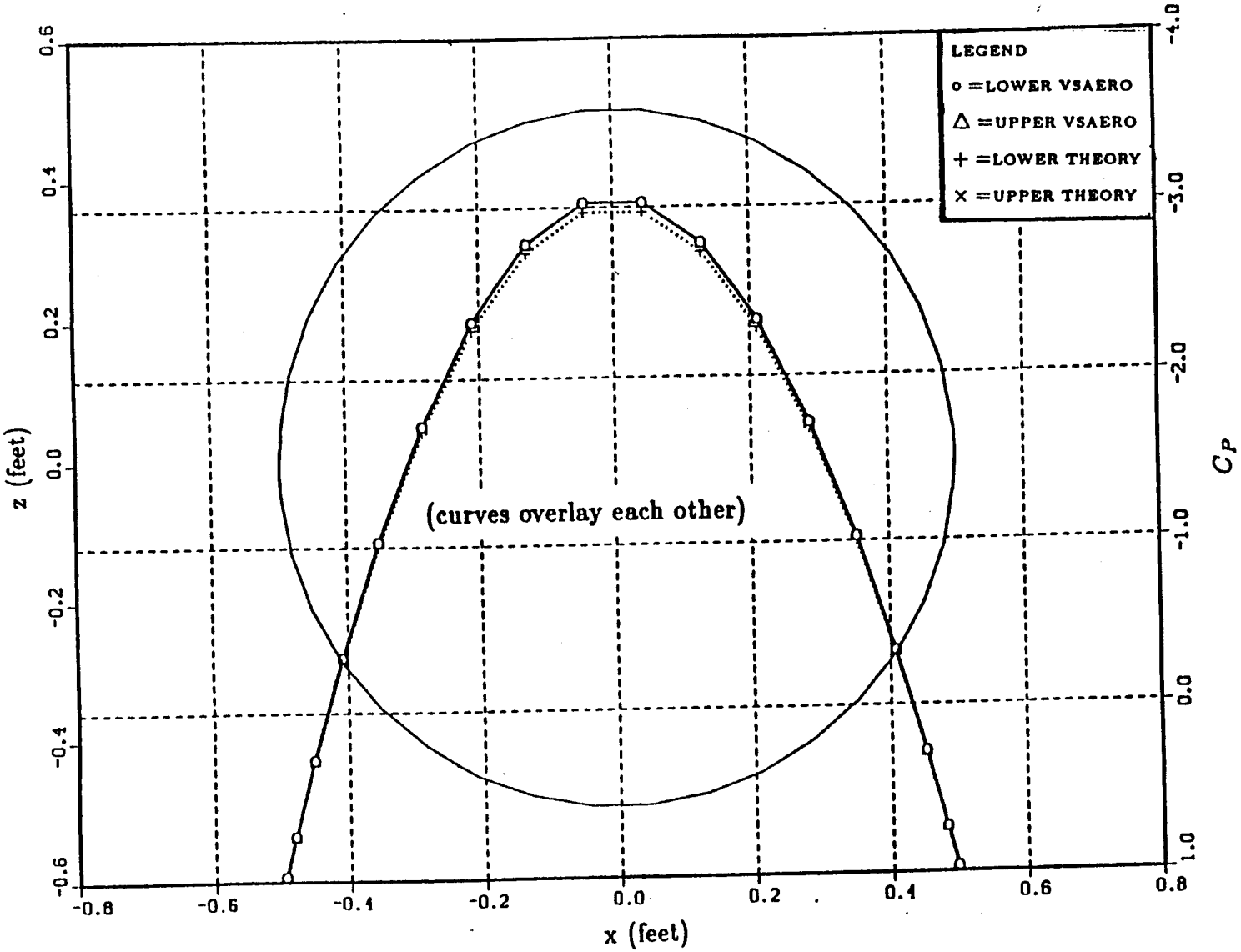

Figure 33 Comparison of the VSAERO and Theoretical Pressure Distributions on a Two-Dimensional Cylinder Inside the Tunnel, Carrying no Lift. Theoretical Results are not Corrected for Tunnel Wall Effects.

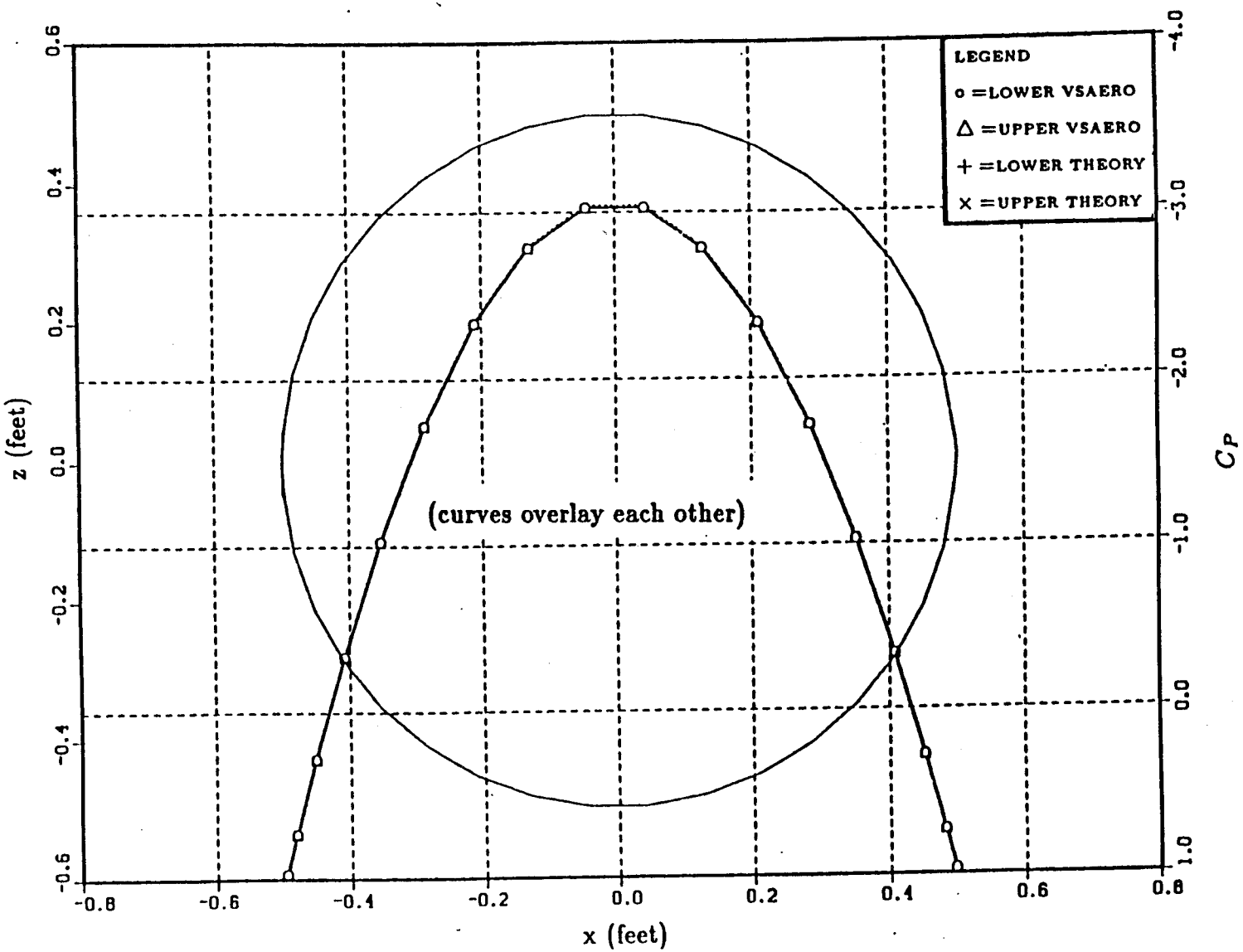

Figure 34 Comparison of the VSAERO and Theoretical Pressure Distributions on a Two-Dimensional Cylinder Inside the Tunnel, Carrying no Lift. Theoretical Results are Corrected for Tunnel Wall Effects.

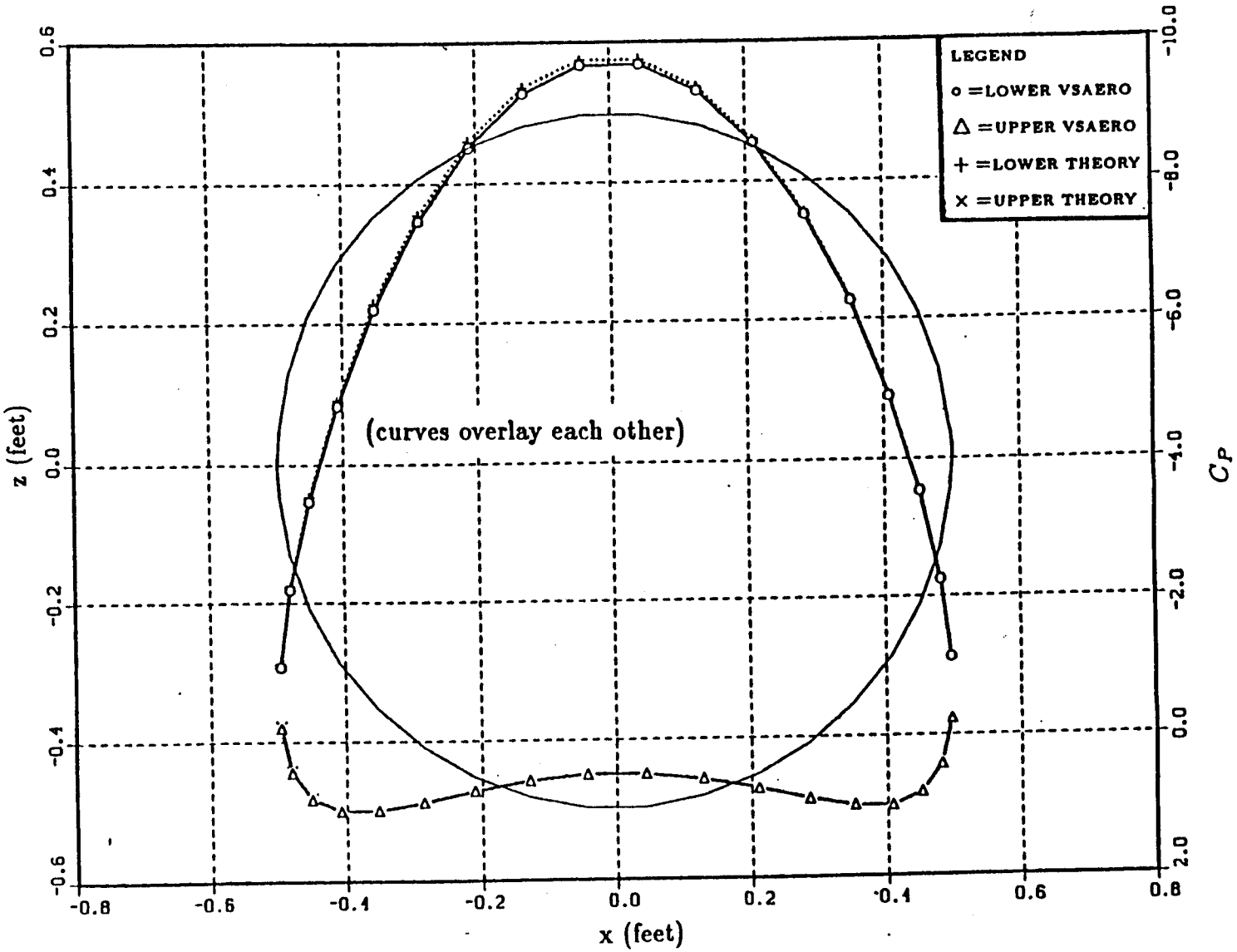

Figure 35 Comparison of the VSAERO and Theoretical Pressure Distributions on a Two-Dimensional Cylinder Outside the Tunnel, Carrying Lift.

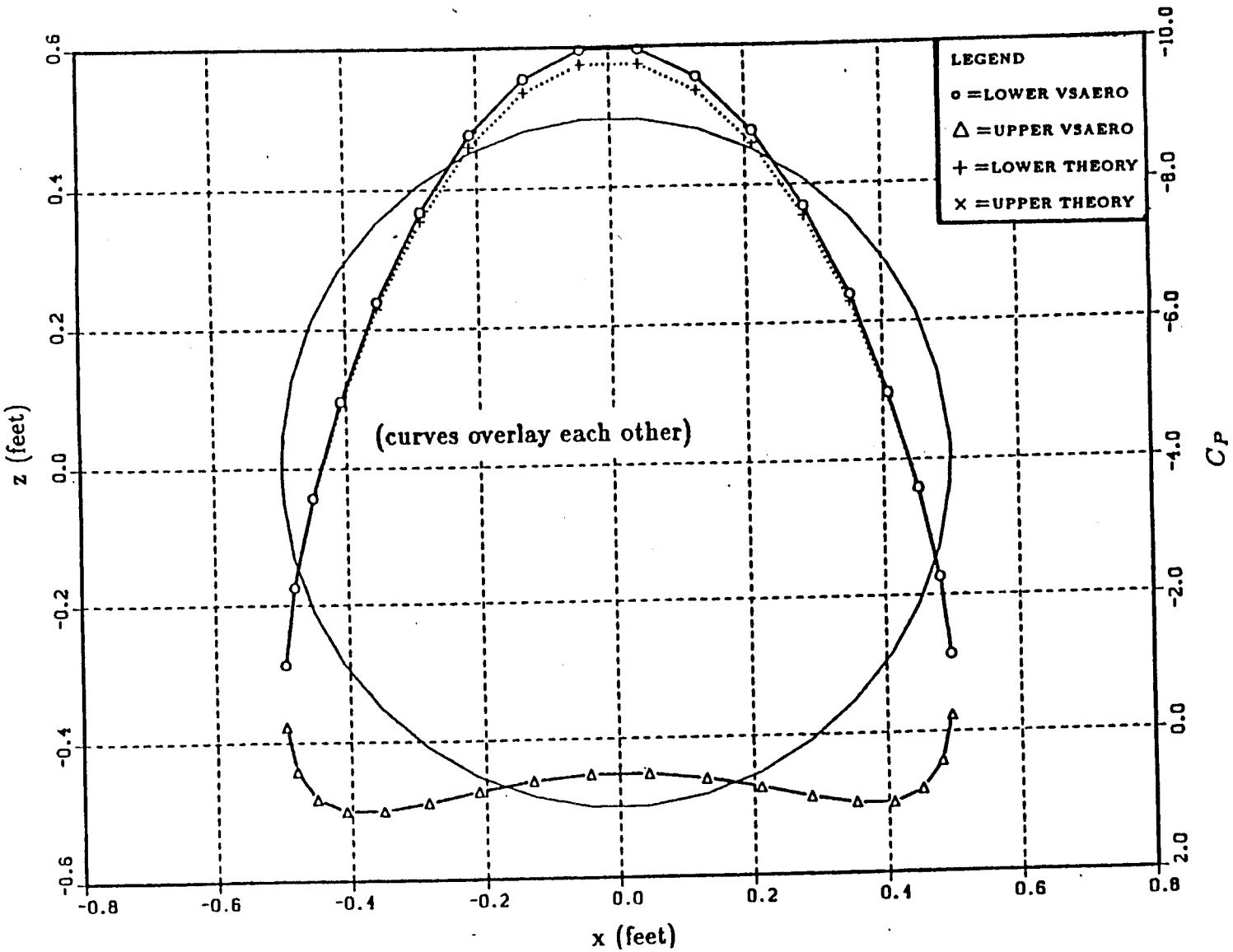

Figure 36 Comparison of the VSAERO and Theoretical Pressure Distributions on a Two-Dimensional Cylinder Inside the Tunnel, Carrying Lift. Theoretical Results are not Corrected for Tunnel Wall Effects.

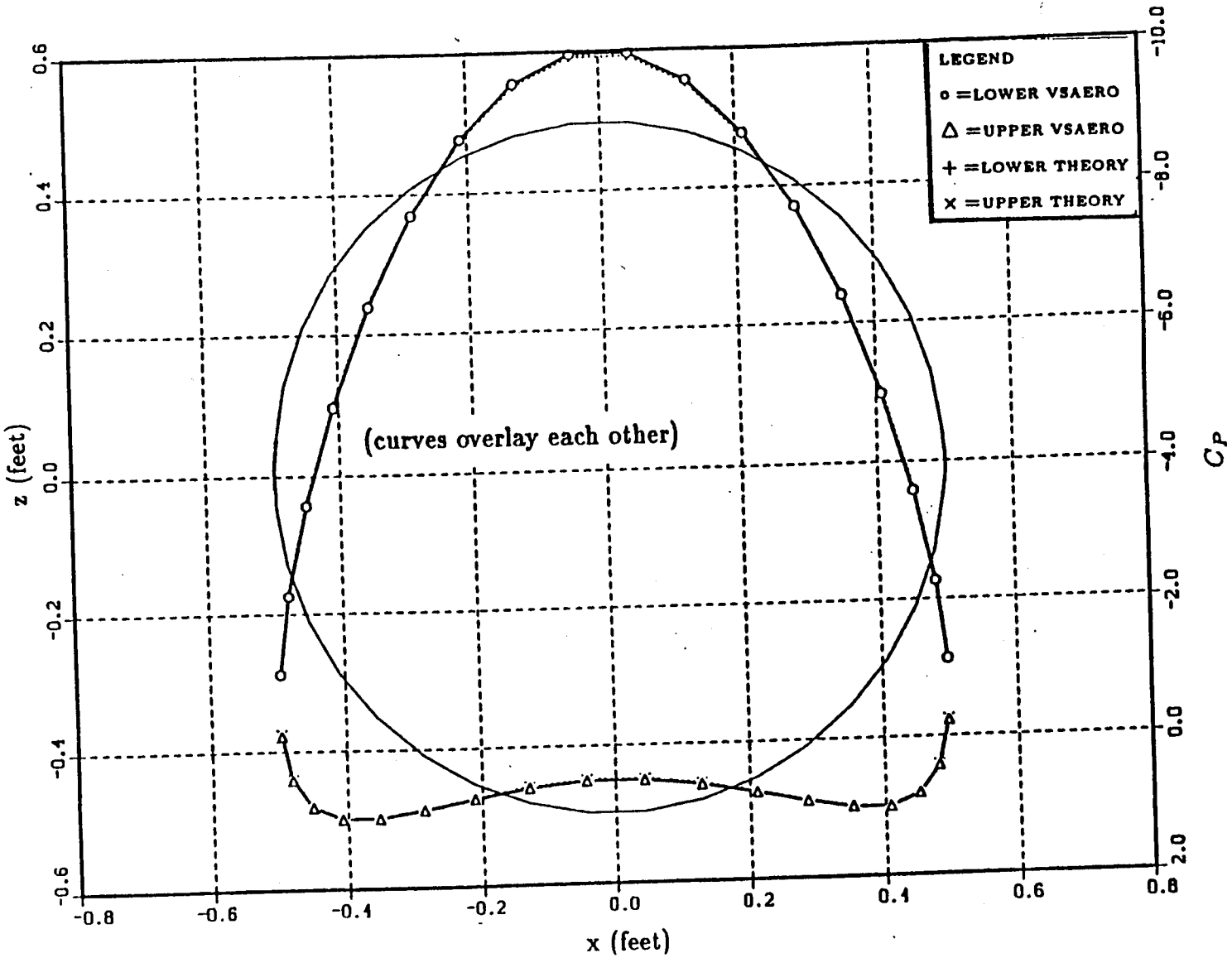

Figure 37 Comparison of the VSAERO and Theoretical Pressure Distributions on a Two-Dimensional Cylinder Inside the Tunnel, Carrying Lift. Theoretical Results are Corrected for Tunnel Wall Effects.

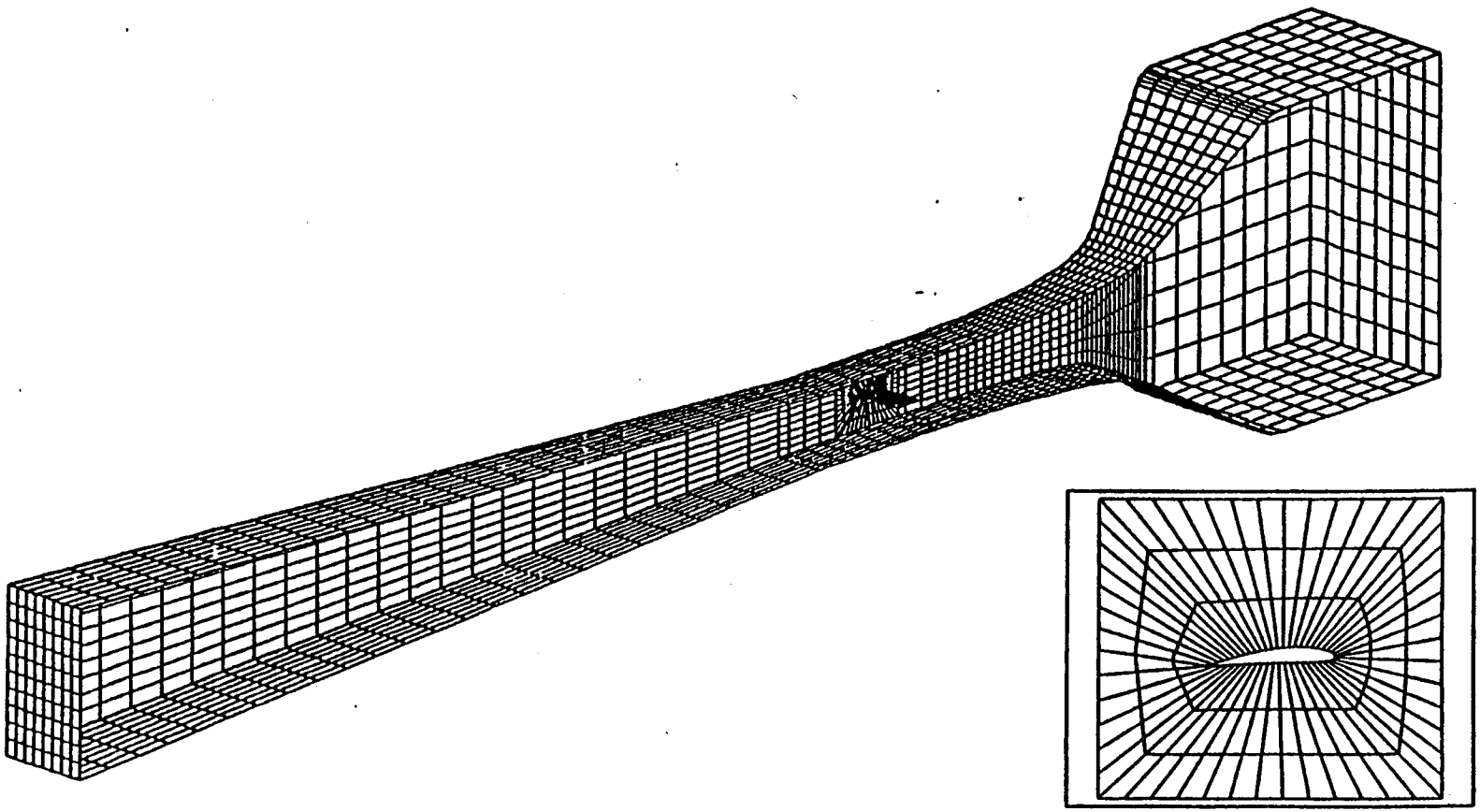

Figure 38 Paneled Geometry of a NACA 4412 Wing in the Army 7 × 10 Wind Tunnel at NASA Ames Research Center with Inset Showing the Details of the Wing/Wall Junction.

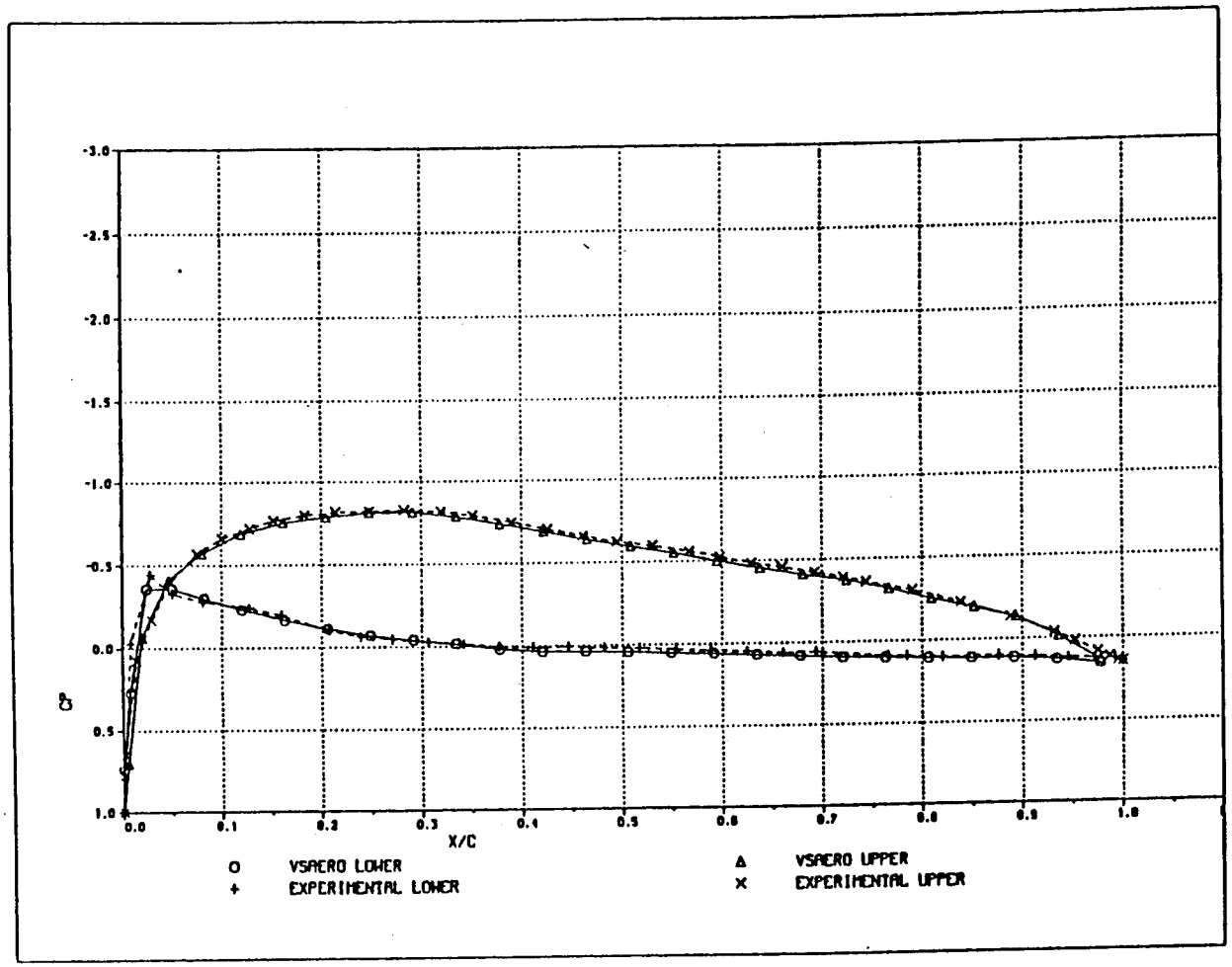

Figure 39 Comparison of the VSAERO and Experimental Pressure Distributions on the NACA 4412 Wing at $\alpha = 0°$

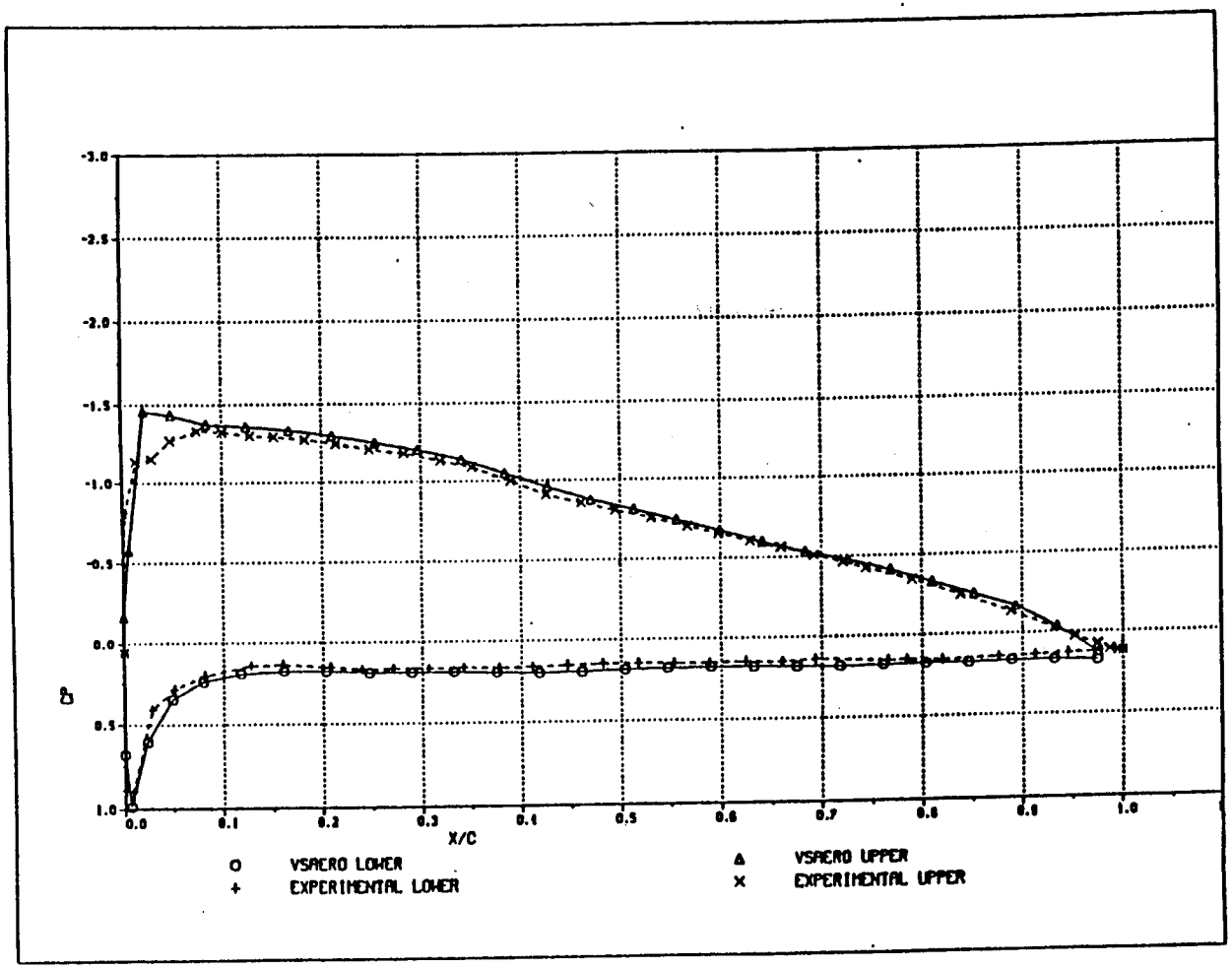

Figure 40 Comparison of the VSAERO and Experimental Pressure Distributions on the NACA 4412 Wing at $\alpha = 4°$

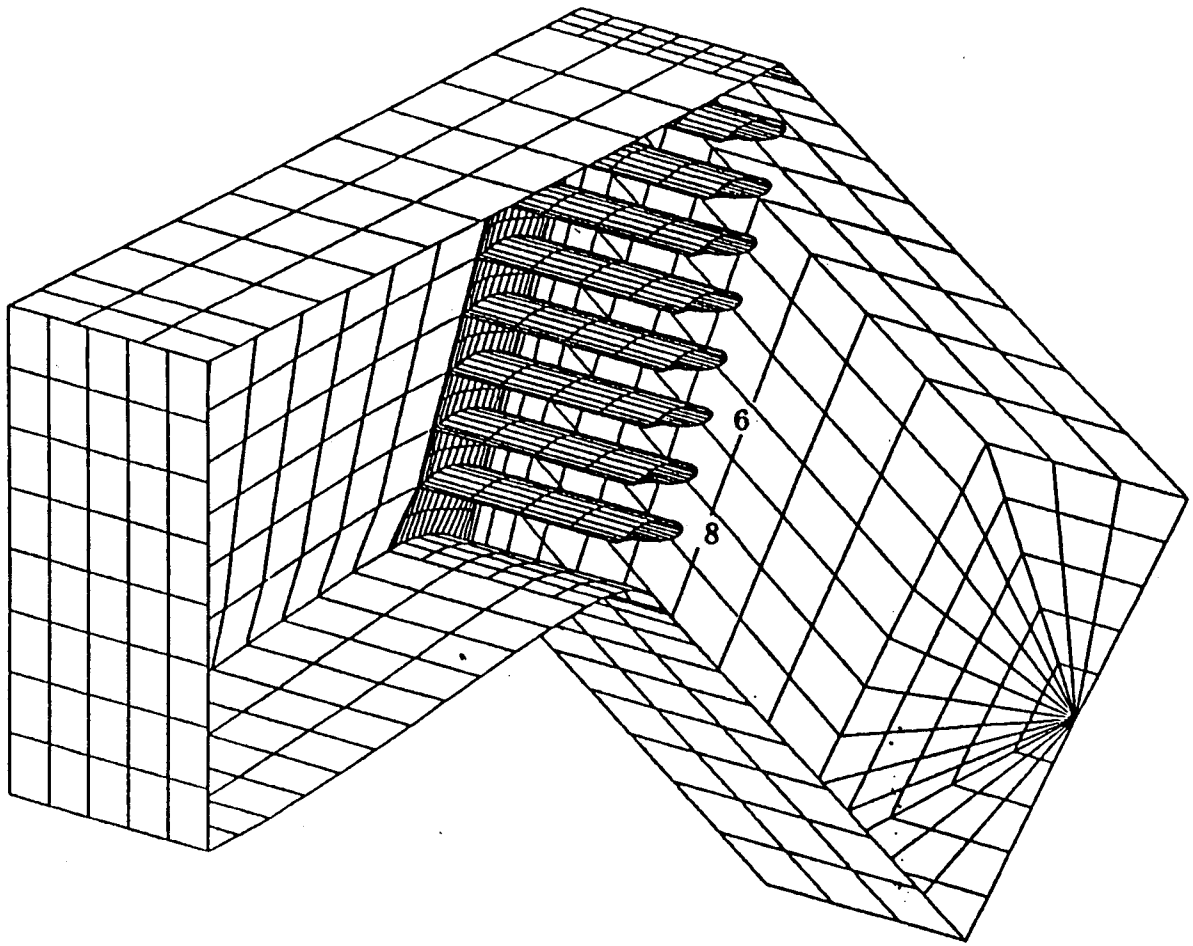

Figure 41 Paneled Geometry of a Set of Turning Vanes in a Tunnel with a 45° Bend in it

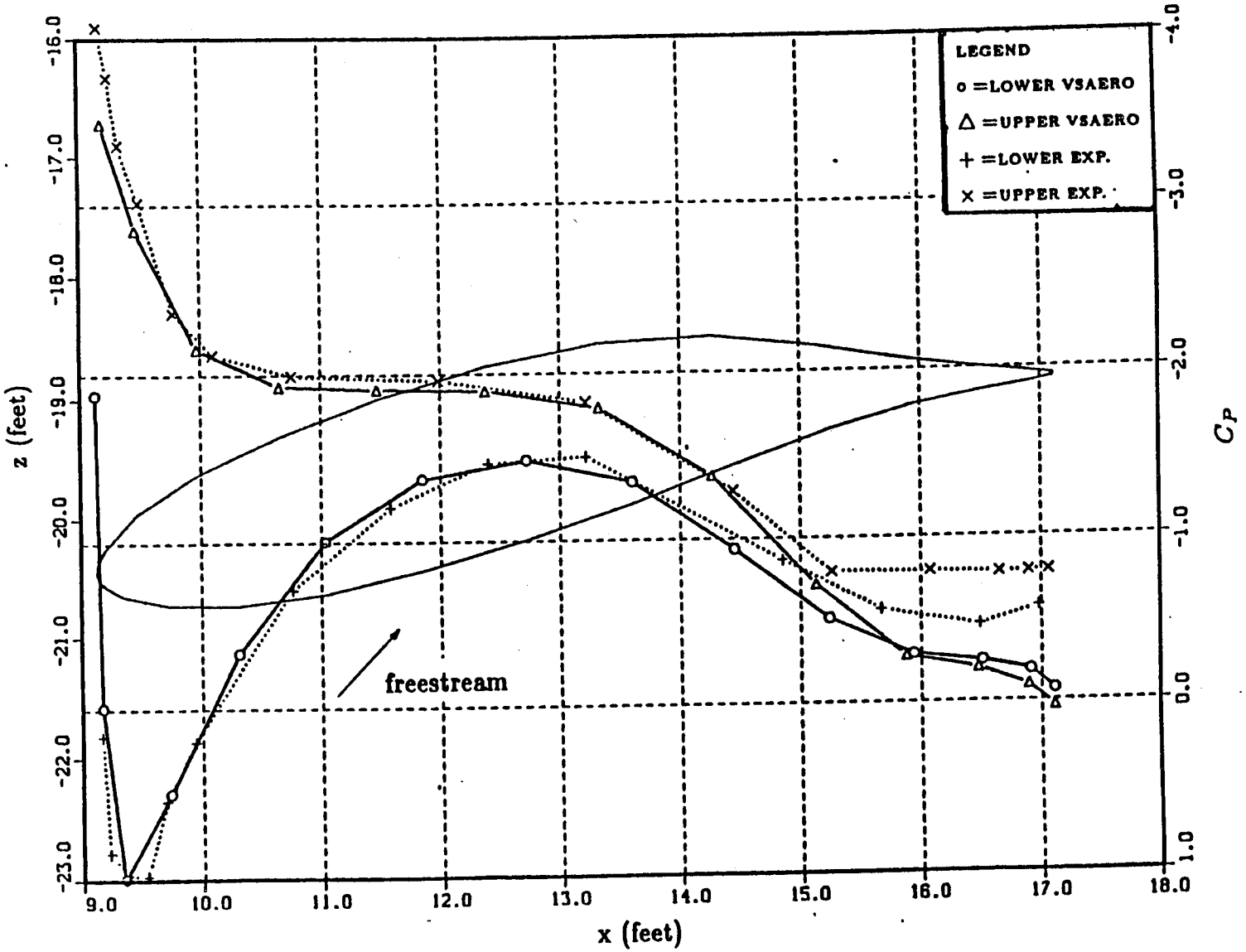

Figure 42 Comparison of the VSAERO and Experimental Pressure Distributions on Vane 6

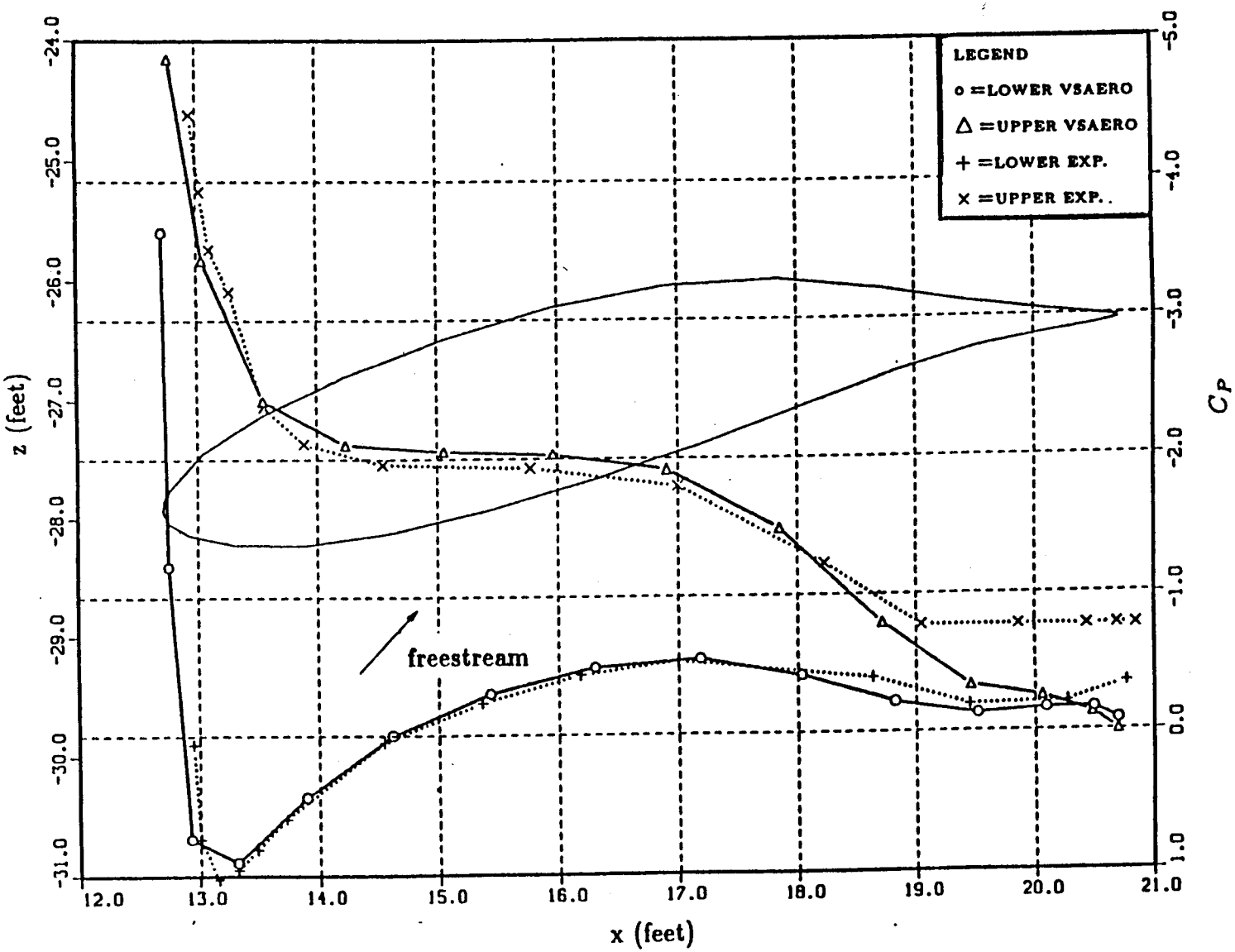

Figure 43 Comparison of the VSAERO and Experimental Pressure Distributions on Vane 8

1. Report No.	2. Government Accession No.	3. Recipient's Catalog No.
NASA CR- 177424		

4. Title and Subtitle	5. Report Date
APPLICATION OF A LOW ORDER PANEL METHOD TO COMPLEX THREE-DIMENSIONAL INTERNAL FLOW PROBLEMS	September 1986
	6. Performing Organization Code
7. Author(s)	8. Performing Organization Report No.
Dale L. Ashby, Doral R. Sandlin	
	10. Work Unit No.
	T 7523
9. Performing Organization Name and Address	11. Contract or Grant No.
California Polytechnic State University Aeronautical Engineering Department San Luis Obispo, California 93407	NCC2-226
	13. Type of Report and Period Covered
12. Sponsoring Agency Name and Address	Contractor Report
National Aeronautics and Space Administration Washington, DC 20546	14. Sponsoring Agency Code
	505-60-21

15. Supplementary Notes

Point of Contact: Technical Monitor, Victor Corsiglia, MS 247-2
Ames Research Center, Moffett Field, CA 94035

16. Abstract

An evaluation of the ability of a low order panel method to predict complex three-dimensional internal flow fields has been made. The computer code VSAERO was used as a basis for the evaluation. Guidelines for modeling internal flow geometries were determined and the effects of varying the boundary conditions and the use of numerical approximations on the solution accuracy were studied. Several test cases were run and the results were compared with theoretical or experimental results.

Modeling an internal flow geometry as a closed box with normal velocities specified on an inlet and exit face provided accurate results and gave the user control over the boundary conditions. The values of the boundary conditions greatly influenced the amount of leakage an internal flow geometry suffered and could be adjusted to eliminate leakage. The use of the far-field approximation to reduce computation time influenced the accuracy of a solution and was coupled with the values of the boundary conditions needed to eliminate leakage. The error induced in the influence coefficients by using the far-field approximation was found to be dependent on the type of influence coeffient, the far-field radius, and the aspect ratio of the panels. In all three test cases run, the VSAERO results agreed very well with experimental or theoretical results, provided the boundary conditions and far-field radius were set according to the guidelines developed in this paper.

17. Key Words (Suggested by Author(s))	18. Distribution Statement
Panel methods, Internal flows, VSAERO, Potential flow	Unclassified - Unlimited Subject Category 02

19. Security Classif. (of this report)	20. Security Classif. (of this page)	21. No. of Pages	22. Price*
Unclassified	Unclassified	91	

*For sale by the National Technical Information Service, Springfield, Virginia 22161